Numerical Studies of Wave Turbulence in Finite Domains

by

Alexander A. Hrabski

A dissertation submitted in partial fulfillment
of the requirements for the degree of
Doctor of Philosophy
(Naval Architecture and Marine Engineering and Scientific Computing)
in the University of Michigan
2023

Doctoral Committee:

Assistant Professor Yulin Pan, Chair
Professor Zaher Hani
Professor Kevin Maki
Professor Peter Miller

Alexander A. Hrabski
ahrabski@umich.edu
ORCID iD: 0000-0001-9620-5833

DEDICATION

To my family and friends,
and
To Charles Doering (1956-2021)

ACKNOWLEDGEMENTS

There are a great deal of people who in some way contributed to this dissertation. I'd like to thank:

My family for supporting me throughout my undergraduate and graduate education, and for always encouraging me to develop my own ideas about the world. Without that encouragement, I'd be a very different person. I'd also like to thank my friends and partner Zena, for endlessly entertaining those ideas I was encouraged to have, among many other things. You all have made the last 5 years very enjoyable.

My mentors of the past for the lessons they taught me, and the time and care it took to do so. In particular Charles Nelson, for teaching me a great deal of discipline, and for challenging me to lead with confidence, especially on the days I least wanted to. Bjorn Malekin and Anke Pinkert, for fostering in me a love of the humanities, and for challenging me to articulate what I truly believe. Namsoo Hyong, for showing me clearly that an individual can develop and surround them self with a wonderful community, and that it is worthwhile to do so. He also taught me that motivation comes from the outside as much as comes from within. Without these lessons, I wouldn't be where I stand today.

The faculty and staff of the Department of Naval Architecture and Marine Engineering, for providing an engaging and well-thought education. I've had many opportunities due to their hard work.

Kevin Maki, Zaher Hani, and Peter Miller for serving on my committee. Your time has been appreciated and your thoughtful comments have greatly enhanced my work. I'd like to thank Gigliola Staffilani, Bobby Wilson, Benno Rumpf, Filippo Giuliani, Ricardo Grande, and Sergey Nazarenko for their time and input over the past few years. I'd also like to thank the late Charles Doering, for his advice and comments. I believe he would have enjoyed seeing the conclusions to which we eventually came, and I dedicate this dissertation in his honor.

My advisor, Yulin Pan, who has shown me endless patience, and who taught me to think carefully and thoroughly. Your hard work has helped me grow tremendously, and you have my deepest gratitude.

My colleagues in Yulin's Flow Physics and Engineering Lab. In particular, I'd like to thank Xianliang Gong, Zhou Zhang, Jeongbin Park, and Ashleigh Simonis. It's been a pleasure to work with you all, and it's a great joy to call you friends.

Those who have funded my education: my family, Yulin Pan, the Department of Naval Architecture and Marine Engineering, the Anthony Lutkus Scholarship, and the National Science Foundation Graduate Research Fellowship Program. Any opinions, findings, and conclusions or recommendations expressed in this material are mine and do not necessarily reflect the views of the National Science Foundation.

And, last but not least, I'd like to thank those who created and made available this dissertation template in LaTeX, including John Meluso, Derek Dalle, and others. Many graduate students indeed owe you greatly!

TABLE OF CONTENTS

LIST OF FIGURES

FIGURE

LIST OF APPENDICES

ABSTRACT

Nonlinear wave systems are ubiquitous in nature, and when many incoherent dispersive waves interact, there is the potential for wave turbulence (WT). Just as in flow turbulence, systems in WT exhibit inter-scale energy cascades, power-law inertial-range spectra, and even intermittency. Unlike in flow turbulence, however, a natural analytical closure for field statistics has been developed. By closing the hierarchy of moment equations that determine field statistics, spectral evolution can be expressed as a Boltzmann-like Wave Kinetic Equation (WKE). The WKE and its supporting closure make formal predictions for the steady power-law inertial-range spectra (known as the Kolmogorov-Zakharov (KZ) spectra), the energy cascade strength and direction, and much more. In addition to being of great theoretical interest, the WKE has been widely employed as a reduced-order model for spectral evolution in practical applications such as global ocean wave forecasting models.

The WT closure and the WKE are derived in the large-domain and infinitesimal wave amplitude limit (together, the kinetic limit), and they describe the average effect of the wave-wave interactions that drive spectral evolution. When a wave system is realized on a finite domain with finite wave amplitude, this assumption of the kinetic limit does not hold. As a result, WKE predictions such as the KZ spectrum become questionable. Numerical and physical experiments in bounded domains often describe steeper spectra and weaker energy cascades than theory predicts. In extreme cases, coherent structures can form that even lead to the breakdown of the kinetic wave description. While recent theory for predicting finite-size effects is in fairly good agreement with observations, it is a largely qualitative model built on kinematic relationships, considering finite-size effects by comparing Fourier domain discreteness to nonlinear broadening of the dispersion relation. For a given domain size, this theory predicts that finite-size effects will dominate when nonlinear broadening becomes much smaller than characteristic Fourier-space frequency spacing.

In this dissertation, we work towards a more quantitative, dynamics-based understanding of finite-size effects through numerical studies of the Majda-McLaughlin-Tabak (MMT) model. First, we explore a limitation of the aforementioned kinematic model: we show that weakly nonlinear wave dynamics in a finite-domain are shaped by the structure of the Discrete Resonant Manifold of wave-wave interactions, which in some cases can support WKE-like dynamics even when nonlinear broadening goes to zero. Next, we explore the properties of the energy cascade in a bounded domain as nonlinear broadening goes to zero. In addition to showing the importance

of quasi-resonant interactions to kinetic behavior, we develop an interaction-based energy flux decomposition that allows for a direct, dynamical measurement of nonlinear broadening and a novel and effective study of the WT closure. This tool is then used to study WT in the kinetic limit for a one-dimensional model, where we show numerically that, as the domain is made larger and nonlinearity is made weaker, the error of the WT closure is reduced for a statistically steady WT field. A final study explores a novel, almost-periodic coherent structure in the two-dimensional MMT model that emerges when nonlinearity is weak, where we draw a possible connection to Kolmogorov-Arnold-Moser Theory. We conclude with discussion.

CHAPTER 1

Introduction

1.1 Wave Turbulence and its Applications

Nonlinear wave systems are ubiquitous in nature, describing phenomena ranging from millimeter-scale ripples on the ocean's surface [78] to kilometer-scale motions of the solar wind [38]. Despite the diverse physical mechanisms that drive these waves, their dynamical descriptions share much in common. Realistic wave systems are often multi-scale processes, in which their evolution is determined by motions at a broad range of length- and time-scales. The agitated sea depicted in Figure 1.1 is an example of a multi-scale system, where waves of many length scales oscillate at disparate frequencies. Due to the nonlinearity of these systems, these multi-scale dynamics support an inter-scale energy cascade driven by wave-wave interactions. This energy cascade is frequently accompanied by power-law energy spectra and self-similar field statistics. Because these behaviors are highly analogous to those of flow turbulence, such a process in wave systems is referred as wave turbulence.

Due to the breadth of physical processes that exhibit wave turbulence, Wave Turbulence Theory (WTT) has seen a great deal of development since its first descriptions in the early-to-mid 20th century [79, 43, 99]. For a wave field exhibiting WT, the goal of WTT is to describe the statistical evolution of the field [101, 69]. These statistical descriptions have greatly enhanced our understanding of nonlinear wave processes, which in turn have enabled predictive modeling in a variety of contexts. In ocean surface waves, ideas from WTT play a key role in spectral forecasting models like WaveWatch III [95], which are used to guide safe and efficient maritime operations, among many other things. Internal ocean gravity waves exhibit wave turbulence and are a critical mechanism for ocean mixing [81, 75, 97], which drives a litany of important oceanic and atmospheric processes. Other applications include, but are not limited to, Magnetohydrodynamics [38], Bose Einstein Condensates [71], Acoustics [59, 41], vibrations of metal sheets [29], and even Gravitational waves in the early universe [39].

Figure 1.1: The rough sea, captured by a NOAA research vessel. Note the range of feature sizes, from small ripples to swells that are meters in length.

1.2 Statistical Closure and the Wave Kinetic Equation

The challenge in quantitative descriptions of wave turbulence is similar to that of flow turbulence [72]. Multi-scale nonlinear wave systems evolve according to wave-wave interactions, and for the large systems typical in nature, the number of interactions is huge. While computational tools exist for the simulation of these systems, a robust theoretical description of the fully deterministic field is intractable. For this reason, we turn to a statistical description of the dynamics. To keep our discussion general, we note here that all subsequent quantities will be unitless, assuming the wave system of interest has been suitably nondimensionalized. The primary statistic of interest is wave action spectrum $n(\boldsymbol{k}, t)$, where $\boldsymbol{k}$ is a d-dimensional wavenumber vector corresponding to a d-dimensional physical space, and t is time. Wave action spectrum is a second order statistic that describes (roughly) the mean-square amplitude of each Fourier component of the field. When one writes the governing equation for wave action evolution, it is quickly discovered to depend on multi-mode statistics of a higher order than wave action itself (e.g., fourth order statistics for surface gravity waves). Thus, to solve for the evolution of wave action spectrum, one must know the evolution of some set of higher-order statistics. A governing equation can be written for these statistics also, however they themselves evolve according to even higher-order statistics! In this way, a hierarchy of statistical dependency is formed.

This problem exists also in flow turbulence, where it is addressed by Kraichnan's Direct Interaction Approximation (DIA) [51] and subsequent developments [e.g., 52]. Under a set of more-or-less

heuristic assumptions, Kraichnan *closed* the statistical hierarchy to obtain an evolution equation for the velocity covariance tensor, which is the analogous quantity to the action spectrum of wave turbulence. A statistical closure expresses high-order statistics as functions of lower-order statistics, thus *closing* the hierarchy and allowing for explicit computation of statistical evolution. A statistical closure for wave turbulence also exists. Due to the structure of nonlinear dispersive wave equations (compared to the Navier-Stokes equations), the closure arises in a far more natural way than the DIA, and, recently, has even been rigorously justified for the Nonlinear Schroedinger Equation (NLS) [22]. While there are many technical aspects to the closure, some of which will be discussed in detail, the general picture is as follows: under the assumptions of random initial wave phase and amplitude among Fourier modes, and, in the limits of a large domain and weak nonlinearity, one can close the governing equation for wave action spectrum up to the so-called kinetic timescale. For a four wave process (generally, a system with a cubic nonlinearity) the resulting Wave Kinetic Equation can be written as

$$\begin{aligned}\frac{\partial n_{\boldsymbol{k}}}{\partial t} = \int_{-\infty}^{\infty}\int_{-\infty}^{\infty}\int_{-\infty}^{\infty} 4\pi T^2_{\mathbf{123}\boldsymbol{k}} \left(n_{\mathbf{1}} n_{\mathbf{2}} n_{\mathbf{3}} + n_{\mathbf{1}} n_{\mathbf{2}} n_{\boldsymbol{k}} - n_{\mathbf{1}} n_{\mathbf{3}} n_{\boldsymbol{k}} - n_{\mathbf{2}} n_{\mathbf{3}} n_{\boldsymbol{k}}\right) \\ \times\delta\left(\boldsymbol{k}_1 + \boldsymbol{k}_2 - \boldsymbol{k}_3 - \boldsymbol{k}\right)\delta\left(\tilde{\omega}_{\mathbf{1}} + \tilde{\omega}_{\mathbf{2}} - \tilde{\omega}_{\mathbf{3}} - \tilde{\omega}_{\boldsymbol{k}}\right) d\boldsymbol{k}_1 d\boldsymbol{k}_2 d\boldsymbol{k}_3,\end{aligned} \tag{1.1}$$

where $T_{\mathbf{123}\boldsymbol{k}} = T(\boldsymbol{k}_1, \boldsymbol{k}_2, \boldsymbol{k}_3, \boldsymbol{k})$ is the interaction kernel of the wave equation, $n_{\boldsymbol{i}} \equiv n(\boldsymbol{k}_i, t)$, $\tilde{\omega}_{\boldsymbol{i}} \equiv \tilde{\omega}(\boldsymbol{k}_i)$ is the renormalized power-law dispersion relation, and δ denotes the Dirac delta function. Immediately, one can see that the WKE expresses wave action evolution as an integral over all combinations of 4 wave modes in the domain. Hence, the RHS of (1.1) is said to be an integral over wave-wave interactions. This turns out, in fact, to be critical in understanding the WT closure and the WKE.

While (1.1) is useful in modeling transient spectra, this dissertation will take special interest in its predictions for stationary spectra, i.e., those spectra with $\frac{\partial n_{\boldsymbol{k}}}{\partial t} = 0$ for all $\boldsymbol{k}$. As we will discuss next, there exist exact, stationary power-law solutions to the WKE, known as Kolmogorov-Zakharov spectra, whose scaling exponents sometimes agree with experimental observation. These spectra often require a long integration to develop: typically many times the kinetic timescale over which the WT is derived. Thus, they are a difficult object for rigorous mathematical analysis, motivating their numerical study.

1.2.1 Theoretical Predictions for Stationary Spectra and their Realizability

Stationary solutions to (1.1) can be found by substituting a general power-law Ansatz of $n_{\boldsymbol{k}} = A|\boldsymbol{k}|^{\gamma}$, and then, after a series of transformations, known as the Zakharov Transformations, finding zeros

of the integrand [101, 69]. There exist, in general, four stationary power-law solutions to (1.1). The first two, representing equipartition of wave action $n_{\boldsymbol{k}} = C$ and equipartition of energy $n_{\boldsymbol{k}} = C/\omega_{\boldsymbol{k}}$, produce no inter-scale flux. The latter of these is known as the Rayleigh-Jeans (RJ) spectrum, and represents the thermodynamic equilibrium of the system. These solutions are typically not considered to be wave turbulence. On the other hand, two finite-flux solutions exist, corresponding to a forward cascade of energy (i.e., from large scales to small scales) and an inverse cascade of wave action. These spectra take the forms of $n_{\boldsymbol{k}} = C_0 P^{\theta_0} k^{\gamma_0}$ and $n_{\boldsymbol{k}} = C_1 Q^{\theta_1} k^{\gamma_1}$, respectively, and are together known as the Kolmogorov-Zakharov (KZ) spectra. Here, P represents the average non-dimensional flux of energy from large scales to small scales, Q represents the average non-dimensional flux of wave action from small scales to large scales, and C_0 and C_1 are known as Kolmogorov constants. While solutions of these forms usually exist to (1.1), whether or not they are *realizable* is an important and non-trivial question [101, 69]. For the remainder of this thesis, we will consider primarily the so-called "forward" cascade KZ solution, corresponding to a spectrum of $n_{\boldsymbol{k}} = C_0 P^{\theta_0} k^{\gamma_0}$ with a flux of energy "forward" from the large scale to the small scale. However, much of the underlying theory for the "inverse" KZ solution (i.e., corresponding to the wave action flux Q from the small scale to the large scale) is similar, and the realizability of these two different spectra are closely related. Also, many of the conclusions of this dissertation developed for the forward cascade are expected to hold for the inverse cascade.

Experimental and numerical experiments of the forward cascade of wave turbulence and its associated spectra are an important topic. To provide even a thorough review of the literature on this topic is a difficult task, as it has a long history with many facets. For a representative review for the surface water wave systems, we refer the reader to [31]. Here, we will only take a moment to note that, for systems such as surface capillary waves, the KZ spectrum has been widely observed in a variety of numerical and experimental contexts [78, 21, 77, 31].This not generally the case, however, and often times in numerical studies and physical experiments of other wave systems, the KZ spectra are not observed. For example, in the internal wave system in a rotating fluid, the KZ spectrum is only created with the use of a sophisticated experimental setup that eliminates competing physical mechanisms [67, 70]. Similar mechanisms will be discussed in Section 1.4. The inevitable conclusion of the broad literature on this topic is that there is no single general reason why KZ spectra are not observed, but rather a variety of factors that contribute the breakdown of one or more of the many assumptions required for the KZ spectrum. The remainder of this chapter will largely be dedicated to describing these mechanisms.

In order for the forward KZ spectrum to be realized in real systems, a few conditions must be met. Let us assume for now that the assumptions that underlie the WKE are sufficiently satisfied, so that the WKE is a good model for wave action spectrum. First, the KZ spectrum must be shown to be *local* (more precisely, the spectrum must have *stationary locality*), meaning that the RHS of

(1.1), known as the collision integral, must not diverge for spectra with γ in the neighborhood of γ_0. Even if the spectrum is in this sense local, it is possible that solution is unstable, or even that the forward cascade solution corresponds to a non-physical inverse cascade of energy. If the KZ solution is non-local, unstable, or predicts the wrong sign of energy flux (i.e., is non-physical), the solution cannot be realized [101, 69]. Additionally, a stationary forward cascade process in a real system must be accompanied by forcing at some scale and dissipation at disparate, higher scales. These scales are separated inevitably by a finite distance in $\boldsymbol{k}$-space, whereas the KZ spectra are derived assuming a power-law form for infinite $\boldsymbol{k}$. The underlying assumption in realizing the KZ spectrum is that the forcing and dissipation scales are sufficiently separated to support an "inertial" range of self-similar dynamics supported only by the nonlinearity of the wave equation. The general stability of finite-width (in wave number) KZ spectra is an open question [101, 30], with plenty of evidence that dissipation effects on inertial range dynamics are non-negligible for certain systems [34, 65]. We note also that there are further considerations not discussed here, such as stability of the KZ spectra under anisotropic perturbation and *evolution locality* [101, 69].

Even with these difficulties, there are additional considerations that affect the realizability of KZ spectra. This class of issues is not to do with technicalities of the WKE, but rather the assumptions that underlie the WKE as a model for wave action spectrum. The WKE is derived in the so-called "kinetic limit", which formally requires that the limits of a large domain and infinitesimal nonlinearity are taken in a rather delicate way [69, 30, 22]. Real wave systems, however, seldom take place in a truly infinite domain with infinitesimal wave amplitude, and thus, without careful analysis, it is unclear to what extent the WKE should apply. Additionally, the statistical assumptions that produce the WKE are imposed at some initial time $t = 0$, and it must be shown *a posteriori* that these assumptions remain valid up to the kinetic timescale (over which the WKE describes evolution). Whether these assumptions remain valid for the timescales of interest in the study of realistic stationary spectra must be further considered [30, 73]. Lastly, nonlinearity in the governing wave equation can produce correlations in wave phases and amplitudes between modes that lead to the breakdown of the statistical closure [69]. These types of behavior often depend on the specifics of the wave equation itself and, as will be seen later in this thesis, can radically change the dynamics of the field. In the following two sections, we explore in greater detail these issues surrounding the validity of the WKE as a model for wave action evolution and the corresponding effects on stationary solutions to the WKE.

1.3 The Kinetic Limit and Finite-size Effects

There are a great many relevant problems in wave turbulence, and nonlinear wave physics more broadly, that fall outside of the kinetic limit. Numerical evaluations of nonlinear wave systems

frequently occur on periodic domains of some finite size, and physical experiments are typically constrained to a container or basin of fixed size. Thus, the extent to which WKE predictions like the KZ spectra can be realized on a bounded domain is of great interest.

Because the wave turbulence closure is derived in the kinetic limit, the WKE can only formally be expected to hold on an infinite domain under infinitesimal nonlinearity. These limits, in fact, must be taken in a specific order - the "large-box" limit, referring to (infinite) domain size, must be taken before the limit of weak nonlinearity [22]. The definition of "weak nonlinearity" can differ depending on context. For surface gravity waves, it is typically meant that the wave amplitude of each Fourier mode for surface elevation is small compared to its wavelength. In more general contexts, a ratio of nonlinear and linear contributions to the evolution of Fourier coefficients can be used. There is much more to say on the topic of the kinetic limit, as will be discussed extensively in later chapters. For now, it will suffice to say that the kinetic limit determines two important features of the dynamics. A large domain ensures that there are many wave-wave interactions that are *quasi-resonant*, the definition of which will be provided shortly. On the other hand, weak nonlinearity restricts only those interactions that are very (asymptotically) close to resonance to contributing to wave action evolution. Thus, the required order of these two limits ensures there are a massive number of quasi-resonant interactions available to drive spectral evolution no matter how small the nonlinearity. On small domains, too few quasi-resonant interactions exist for the WKE to be a good model of the dynamics. When finite-domain dynamics are compared to WKE predictions, limited spectral evolution, reductions in the strength of the inter-scale energy cascade, and steepening of the power-law wave action spectra are observed (see Section 1.3.2 for a brief review). These anomalies in finite-domain kinetic wave physics are referred to collectively as "Finite-size effects". To better understand this picture, we present a popular kinematic explanation put forward by L'vov and Nazarenko [60].

1.3.1 A Kinematic Understanding

The kinematic description that follows is most clear if we constrain ourselves to a specific class of system. Thus, we will consider a wave equation evaluated on a two-dimensional (2D), periodic, square domain of side length L. The wave equation of interest describes the evolution of a complex scalar $\psi(\boldsymbol{x}, t) \in \mathbb{C}$ according to a linear dispersion term and a simple cubic nonlinearity, and the dispersion relation will be given explicitly by $\omega(k) = |\boldsymbol{k}|^2$. The NLS is an example of a system in this category, and a closely related system will be studied throughout the majority of this dissertation. We also will assume that the size of the solution $|\psi(\boldsymbol{x}, t)| \sim O(\varepsilon)$, where ε is a small positive number, so that the nonlinearity is weak. Formalities to do with ε, L, and the wave equation itself will be precisely defined in Chapter 2.

For our periodic domain, we say that $\boldsymbol{x} \in \mathbb{T}_L^2$, or written out, $\boldsymbol{x}$ belongs to the 2D torus $\mathbb{T}_L^2$. For a domain of this type, we can express $\psi(\boldsymbol{x}, t)$ as a Fourier series, summing over all the wave number vectors $\boldsymbol{k}$ that exist in the corresponding Fourier-domain Λ_L^2. The Fourier series representation of $\psi(\boldsymbol{x}, t)$ is given by

$$\psi(\boldsymbol{x}, t) = \sum_{\boldsymbol{k} \in \Lambda_L^2} \hat{\psi}_{\boldsymbol{k}}(t) e^{i\boldsymbol{k}\cdot\boldsymbol{x}} \tag{1.2}$$

where $\Lambda_L^2 \equiv \{(m, \ell) \mid m, \ell \in 2\pi\mathbb{Z}/L\}$. Both the physical domain and the corresponding wave number domain are depicted in the first row of Figure 1.2. Crucially, for a finite physical domain, Fourier domain is a lattice. As L is made large, the lattice spacing $\Delta k = 2\pi/L$ becomes small.

On the other hand, *after* the kinetic limit is taken, physical domain is given by $\boldsymbol{x} \in \mathbb{R}^2$, so the corresponding Fourier domain must also be given by $\boldsymbol{k} \in \mathbb{R}^2$ (as the Fourier series (1.2) becomes a Fourier transformation). Thus, in the kinetic limit, Fourier domain becomes continuous. The origin of finite-size effects rests with these differences in Fourier domain. To see how, we now consider the delta functions of the wave kinetic equation, which provide the kinematic conditions that determine which types of wave-wave interactions contribute to wave action evolution in the kinetic limit. The collision integral is nonzero only if the following conditions are satisfied for any 4 wave modes,

$$\boldsymbol{k}_1 + \boldsymbol{k}_2 - \boldsymbol{k}_3 - \boldsymbol{k} = \boldsymbol{0} \tag{1.3}$$

$$\omega_{\boldsymbol{1}} + \omega_{\boldsymbol{2}} - \omega_{\boldsymbol{3}} - \omega_{\boldsymbol{k}} = 0 \quad , \tag{1.4}$$

where we have neglected to renormalize the dispersion relation for clarity (see Chapter 2 for details). Equation (1.3) is often referred to as the wave number condition, and wave-wave interactions that satisfy this condition are referred to as quartets. This condition results from the cubic nonlinearity of the wave equation, and must always be satisfied, no matter which assumptions on wave statistics or nonlinearity we employ. The condition (1.4), on the other hand, emerges only in the kinetic limit, and is known as the resonance condition. Wave-wave interactions that satisfy the resonance condition are referred to as resonant interactions or resonant quartets. *Quasi-resonant* interactions refer to interactions that *approximately* satisfy (1.4). Indeed, when ε is small but not zero, interactions that satisfy

$$|\omega_{\boldsymbol{1}} + \omega_{\boldsymbol{2}} - \omega_{\boldsymbol{3}} - \omega_{\boldsymbol{k}}| \leq \Gamma(\varepsilon) \tag{1.5}$$

may contribute to spectral evolution, where Γ decreases as ε is made small. This fact is intimately related to the realization of the WT closure on finite domains, as we will later show.

For our chosen domain and dispersion relation, there is a geometric interpretation of these conditions. When added tip-to-tail, the wave number condition requires that the wave number vectors form a quadrilateral. If one additionally imposes the resonance condition, it can be shown

(in Appendix B) that the wave number vectors must be configured in a rectangular fashion, albeit in a somewhat unintuitive way. In the case of the quasi-resonance condition (1.5), the wavenumber vectors may only approximate a rectangle. This geometric interpretation of (1.3), (1.4) and (1.5) is also depicted in Figure 1.2. When $\boldsymbol{k}$ is continuous, there are an infinite set of wave-wave interactions that satisfy these conditions. Recall however, that the WT closure requires sufficiently many quasi-resonant interactions to exist as the broadening Γ becomes small. Thus, the realization of the WT closure in finite domain, finite nonlinearity wave systems (and subsequently the observation of WKE predictions) hinges critically on the *number* of wave-wave interactions that satisfy conditions (1.3) and (1.5) when interpreted on the lattice Λ_L^2. As can be deduced from Figure 1.2, as the lattice becomes coarse, there are fewer ways to draw resonant and quasi-resonant quartets (rectangles). However, for sufficiently large Γ, we restore many of the interactions that are eliminated as we admit increasingly skew rectangles. Thus, the magnitude of finite-size effects is said to depend on the interplay of two competing quantities: the magnitude of nonlinear broadening Γ and the characteristic frequency spacing $\Delta\omega = \frac{d\omega}{dk}\Delta k$, which measures the effect of the discreteness of Fourier domain.

Using these parameters, we can define two distinct regimes of dynamics. In the case of $\Delta\omega \ll \Gamma$, the domain size L is sufficiently large for a given (small) ε to ensure there are many quasi-resonant interactions to support the WT closure, and as a result, we expect the WKE and subsequent predictions such as the KZ spectrum to hold. This regime is known as *Kinetic Wave Turbulence* (KWT). On the other hand, when $\Delta\omega \gg \Gamma$, there are insufficient quasi-resonant interactions to support the WT closure, resulting in finite-size effects. This regime of dynamics is known as *Discrete Wave Turbulence* (DWT). In addition to these two regimes, there exists also a *Mesoscopic Wave Turbulence* regime, for which $\Delta\omega \sim \Gamma$, characterized by combinations of kinetic and finite-size behaviors. This kinematic picture is widely adopted in the WT literature, and is frequently used to describe finite-size effects as observed in physical and numerical experiments, as will now be discussed.

1.3.2 Numerical and Physical Experiments

We now briefly revisit the topic of experimental studies, but with a special focus on those studies to do with finite-size effects. Both experiments and numerical simulations of DWT have shown, in many cases, steepened spectra compared to the KWT regime [84, 78], as well as restricted energy transfer [58, 16, 10, 68] or even "frozen turbulence" [84, 65, 103]. Frozen Turbulence refers to a state where there is insufficient resonance to support any spectral evolution. Because the relationship between Γ and the discreteness $\Delta\omega$ is critical to predicting DWT, there are a number of existing techniques to compare these quantities given data, for example, the coherence function

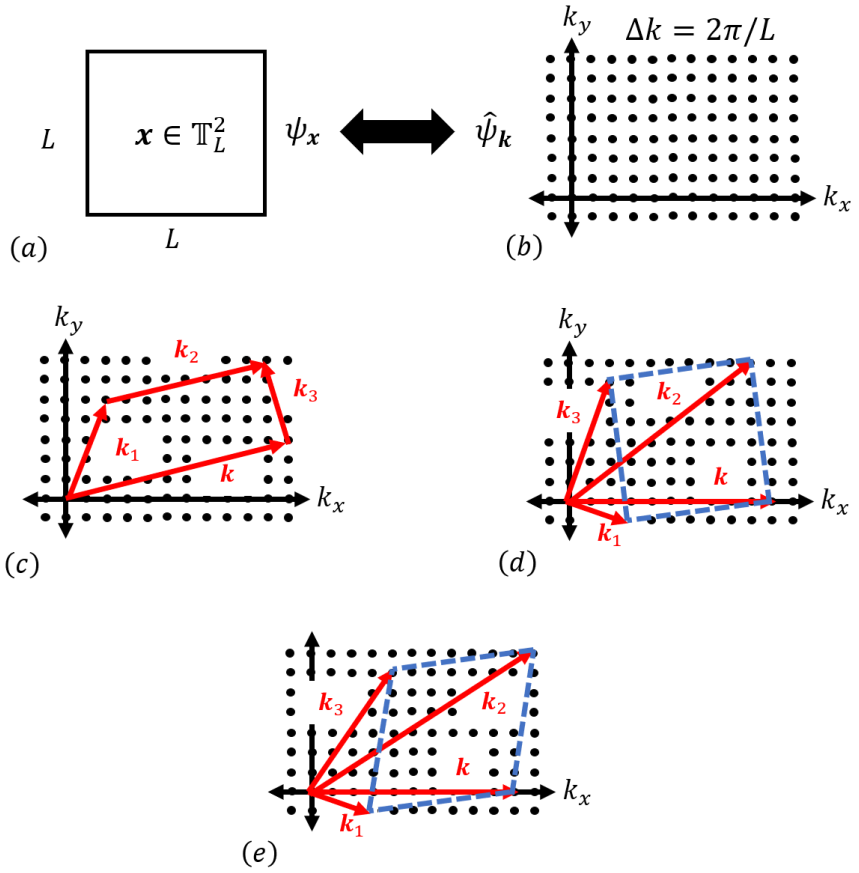

Figure 1.2: (a) the L-periodic physical domain $\mathbb{T}_L^2$ and (b) the corresponding wave number domain Λ_L^2, with lattice spacing $\Delta k = 2\pi/L$. (c) a quartet satisfying (1.3) on Λ_L^2, (d) a quartet additionally satisfying the resonance condition (1.4) for $\omega_{\boldsymbol{k}} = |\boldsymbol{k}|^2$, and (e) a quartet satisfying the relaxed quasi-resonant condition (1.5). For a given Δk, there are many more quartets satisfying (1.5) than (1.4), as there are many more slightly skewed rectangles (e) than true rectangles (d) in Λ_L^2.

[e.g. 2, 77, 102] and the broadened dispersion relation ($k - \omega$ spectrum) [e.g. 68, 21]. While these techniques are often an effective way to compare $\Delta\omega$ and Γ, they do not directly address dynamical questions regarding the WT closure in the DWT regime. Also, there is work [49, 48, 60] to show that, in the DWT regime, the remaining resonant interactions may form disjoint sets of modes, and even drive the formation of integrable or nearly-integrable coherent structures, which brings us to our next topic.

1.4 Coherent Structures

In addition to finite-size effects, there exists another class of behaviors in nonlinear wave systems that can lead to the breakdown of the WT closure. The term "coherent structure" serves as a catch-all category of nonlinear behavior that leads to strong correlations in space and across time. In the case of nonlinear wave systems, examples of coherent structures include solitons [14, 100, 13], breathers [14, 13, 26], wave collapses [87], rogue waves [74, 26], and radiative pulses [88], to name a few. Some of these coherent structures share similar underlying physics. They can form/exist at high or low nonlinearity, and often depend critically on the specific form of a given wave equation. Because of this, studies of coherent structures are often constrained to specific phenomena exhibited in various systems of interest. For example, waves on elastic sheets have been shown to exhibit "sharpening" of their wave crests, leading to spectra that differ from the KZ spectra [64]. On the other hand, some coherent structures, such as rogue waves, are observed in a wide variety of media that are subject to different evolution equations, allowing for more general descriptions and theories [74, 26]. In both cases, the correlations built by these nonlinear processes lead to the breakdown of the statistical assumptions that underlie the WT closure. In particular, phenomena like intermittency are often attributed to the existence/emergence of coherent structures at higher nonlinearities, and, as will be shown in this dissertation, even coherent structures that form at low nonlinearities can strongly dominate an otherwise stochastic process. Now we turn our focus to a particularly relevant class of coherent structure known as breathers.

1.4.1 Breathers in lattices and continuous media

Breathers are a broadly-defined class of features that arise in nonlinear dynamical systems, generally describing a family of solutions with strong spatial localization and oscillations in time. Together with solitons, breathers are considered as prototypes for rogue waves that can occur across many fields, such as water waves [28, 74], optics [26], and plasma physics [25]. In mathematics, breathers are defined to be fundamental solutions to both continuous field equations and discrete lattice problems. Breather solutions to continuous systems have been found primarily in one-dimensional

(1D) nonlinear partial differential equations (PDEs), including the Sine-Gordon equation [18], the nonlinear Schrödinger equation (NLS) [94, 28, 74, 26, 25], the modified Korteweg–De Vries (KdV) equation [14], and certain generalized KdV equations [13]. Discrete breathers [37] have been constructed as solutions to a wide variety of discrete systems, including Josephson Junctions [96, 66] and the Fermi-Pasta-Ulam-Tsingou (FPUT) problem [57].

Another important category of studies regards the spontaneous emergence of breathers (and other coherent structures) under the free evolution of a system. These coherent structures include discrete breathers in the FPUT problem [17] and the discrete nonlinear Schrödinger equation [86, 85], as well as quasi-solitons [100, 88], quasi-breathers [83], and wave collapses [100, 87, 89] identified in the 1D Majda-McLaughlin-Tabak model. As in the case of constructing exact breather solutions to PDEs, these studies are predominantly performed in 1D situations. The only exception, to our knowledge, is [90], which identifies a breather solution to the NLS with a potential on a two-dimensional (2D) domain, but the mechanism associated with the breather remains unexplained. In general, very little is known about 2D breathers in continuous systems.

1.5 Dissertation Overview and Outline

In this dissertation, we explore the dynamics of wave turbulence when realized in finite domains. There are two major components to this work. The majority is aimed at building upon the picture of finite-size effects put forward by L'vov and Nazarenko by developing a complimentary dynamical understanding of finite-domain wave turbulence. In the second component, we explore a novel breather solution to a system that otherwise is shown to follow a stochastic description.

In the study of finite-size effects, our focus will primarily be on the stationary spectra associated with forward cascade process, and will (in particular) focus on the energy cascade itself as a way to understand the changes of wave turbulence in finite domains. This differs from the more typical approach of studying the wave action spectral slope and spatiotemporal/coherence spectra to quantify finite-size effects. To do this, we have developed a novel method for the instantaneous evaluation of inter-scale energy flux that reveals the quasi-resonant contributions to the energy cascade process. All of these studies will be conducted on the Majda-McLaughlin-Tabak (MMT) model, a family nonlinear dispersive wave equations that have been widely used to study various aspects of kinetic wave theory. The basic strategy of each of these studies will be to vary the strength of the nonlinearity by several orders of magnitude. By changing the nonlinearity, we produce a transition from Discrete to Kinetic wave turbulence. In the final study on finite-size effects, we also vary the domain size to numerically approximate the kinetic limit. Given data that captures the finite-size effects of interest, we then perform an extensive study of the energy cascade process and spectral form throughout these ranges of dynamics.

In the second component of this work, we numerically demonstrate the existence of breather solutions to the MMT model, realized on a 2D domain with periodic boundary conditions. In this dissertation, we use a physical definition of breather as spatial localization of energy occurring in a periodic or quasi-periodic pattern in time. In addition to being a novel 2D breather in a continuous field, other remarkable and distinguishing features of the breather include: (1) the breather spontaneously emerges from a stochastic wave field after long-time evolution, not relying on specific initial conditions; (2) the breather appears equivalently for both the focusing and defocusing cases, but exists only in the weak nonlinearity regime. As the nonlinearity of the system increases, we find a breakdown of the breather state with the field relaxing to the Rayleigh-Jeans spectrum. Further analysis suggests that the state trajectory of the breathers is associated with a Kolmogorov-Arnold-Moser (KAM) torus.

The outline of this dissertation is as follows. In Chapter 2, we review the Majda-McLaughlin-Tabak model, and provide detailed derivations for our numerical method, the wave kinetic equation, the Kolmogorov-Zakharov spectra, evaluations of energy flux, and other required formulae for the subsequent studies. In Chapter 3, we perform a study of decaying wave turbulence on rational and irrational tori, demonstrating a sensitivity of wave turbulence in the DWT regime to the structure of the Discrete Resonant Manifold, the set of all interactions on a torus as nonlinear broadening $\Gamma(\varepsilon) \to 0$. In Chapter 4, we provide an extensive study of the forward energy cascade in forced-dissipated wave turbulence in both the DWT and KWT regimes, where we show definitively the necessity of quasi-resonant interactions in forming kinetic wave behavior. We extend these ideas to a study of a 1D MMT model in Chapter 5, where we add a more precise study of the WT closure by varying not only nonlinear strength ε, but also domain size L to numerically approximate the kinetic limit. In Chapter 6, we pivot our focus to a study of the breather solution, after which provide a discussion and concluding remarks in Chapter 7.

CHAPTER 2

The Majda-McLaughlin-Tabak Model and Related Derivations

2.1 The Majda-McLaughlin-Tabak Model

Developed by Majda, McLaughlin, and Tabak (MMT) in their 1997 paper [61], the MMT model was first used to assess the claims of WT via a relatively simple, tuneable nonlinear wave system. The motivation for developing such a system is as follows: real wave systems often require a series of simplifications before a nonlinear wave equation is found that is suitable for kinetic description. Because of this, one cannot be sure if discrepancies from WTT predictions are due to a failure in assumptions that lead to the nonlinear wave equation, or a problem with kinetic description, or even a complicated combination of the two. Additionally, WT depends critically on dispersion relation, dimension, and precise properties of the nonlinearity. A single, tuneable model offers the potential to perform a robust study of theoretical predictions without radically changing the governing equation. Hence, the MMT model has since been widely employed to study WT and related problems.

The model describes the evolution of a complex scalar field $\psi_{\boldsymbol{x}} \equiv \psi(\boldsymbol{x}, t) \in \mathbb{C}$ according to

$$i\frac{\partial \psi_{\boldsymbol{x}}}{\partial t} = |\partial_{\boldsymbol{x}}|^{\alpha}\psi_{\boldsymbol{x}} + \lambda|\partial_{\boldsymbol{x}}|^{\beta/4}\left(\left||\partial_{\boldsymbol{x}}|^{\beta/4}\psi_{\boldsymbol{x}}\right|^2 |\partial_{\boldsymbol{x}}|^{\beta/4}\psi_{\boldsymbol{x}}\right), \tag{2.1}$$

where $\boldsymbol{x}$ is the d-dimensional spatial coordinate, t is time, and $\lambda = \pm 1$ controls the sign of the nonlinearity, with a positive (negative) sign corresponding to a defocusing (focusing) equation. We use the term defocusing out of convention, however, with effect of λ on the formation of coherent structures in the MMT model being more complicated than that of the NLS, which is the equation in which this terminology first arose. The derivative operator $|\partial_{\boldsymbol{x}}|^{\alpha}$ is defined in spectral domain. If we assume a periodic domain of size L, then the $\psi(\boldsymbol{x}, t)$ can be related to the coefficients of a

Fourier series by the Fourier transformation

$$\hat{\psi}_{\boldsymbol{k}} = \frac{1}{L}\int_0^L \psi_{\boldsymbol{x}} e^{-i\boldsymbol{k}\cdot\boldsymbol{x}} d\boldsymbol{x}, \tag{2.2}$$

where the integral is over a d-dimensional periodic domain, and the corresponding Fourier series is given by

$$\psi_{\boldsymbol{x}} = \sum_{\boldsymbol{k}\in\Lambda_L^2} \hat{\psi}_{\boldsymbol{k}} e^{i\boldsymbol{k}\cdot\boldsymbol{x}}, \tag{2.3}$$

where $\Lambda_L^d \equiv 2\pi\mathbb{Z}^d/L$. The operator $|\partial_{\boldsymbol{x}}|^\alpha$ is then defined as

$$|\partial_{\boldsymbol{x}}|^\alpha \psi(\boldsymbol{x},t) \equiv \sum_{\boldsymbol{k}\in\Lambda_L^2} |\boldsymbol{k}|^\alpha \hat{\psi}_{\boldsymbol{k}}(t) e^{i\boldsymbol{k}\cdot\boldsymbol{x}}. \tag{2.4}$$

Here, α explicitly controls the derivative order. We note also that, in general, $|\partial_{\boldsymbol{x}}|^\alpha$ is a non-local operator, and is equivalent to the fractional Laplacian operator for a range of α [56].

Using this model in $d = 1$ dimension, the (short) water wave dispersion relation of $\alpha = 1/2$, MMT demonstrated that, for certain values of β, the WKE fails to predict the spectrum associated with the forward cascade process [61]. Instead, non-KZ spectra, later referred to as MMT spectra, were observed. After validating various aspects of the theory, they eventually found that the WT closure did not represent the true dynamics of their system. Later studies by their group identified system configurations that would produce KZ spectra, and they even observed the coexistence of KZ spectra and the anomalous MMT spectra [8]. Subsequent studies by Zakharov et al. attribute the MMT spectra to coherent structures [100, 88]. As discussed in the introduction, there are nevertheless many open questions as to how and when the KZ spectra (or MMT spectra) may be observed in numerical experiments of the MMT model.

Before we proceed, we note that the MMT model conserves the total number of particles of the solution $\int |\psi_{\boldsymbol{x}}|^2 d\boldsymbol{x}$ (a term derived from statistical thermodynamics), as well as linear momentum $\int \left(\psi_{\boldsymbol{x}} \frac{\partial \psi^*_{\boldsymbol{x}}}{\partial x} - \psi^*_{\boldsymbol{x}} \frac{\partial \psi_{\boldsymbol{x}}}{\partial x}\right) d\boldsymbol{x}$. Here, $\frac{\partial \psi_{\boldsymbol{x}}}{\partial x}$ refers to all d components of the gradient in systems with $d > 1$. Most importantly, the system is Hamiltonian, with H given by

$$H = H_2 + H_4 = \int \left||\partial_{\boldsymbol{x}}|^{\alpha/2}\psi_{\boldsymbol{x}}\right|^2 d\boldsymbol{x} + \frac{1}{2}\lambda \int \left||\partial_{\boldsymbol{x}}|^{\beta/4}\psi_{\boldsymbol{x}}\right|^4 d\boldsymbol{x}. \tag{2.5}$$

The H_2 term corresponds to the linear term on the RHS of (2.1) and H_4 corresponds to the nonlinear term. We also note here that, for $\alpha = 2$ and $\beta = 0$, the MMT model reduces to the cubic NLS without a potential. For the general case of $\alpha = 2$, the MMT model corresponds to a non-local derivative NLS. This can be seen using the field transformation $\phi_{\boldsymbol{x}} = |\partial_{\boldsymbol{x}}|^{\beta/4}\psi_{\boldsymbol{x}}$ for which (2.1)

becomes

$$i\frac{\partial \phi}{\partial t} = |\partial_{\boldsymbol{x}}|^2 \phi + \lambda |\partial_{\boldsymbol{x}}|^{\beta/2} \left(|\phi|^2 \phi \right). \tag{2.6}$$

For $\beta = 2$, this system is a non-local form of the derivative NLS of Kaup and Newell [50], and for $\beta = 4$, (2.6) is local.

We continue our exposition of the MMT model by rewriting (2.1) as an evolution equation for the Fourier coefficients $\hat{\psi}_{\boldsymbol{k}}(t)$. This step is (a) useful in the understanding of the numerical evaluation of (2.1) and (b) necessary to the derivation of the WKE. After substituting (2.3) into (2.1), only the nonlinear term requires special attention. This term can be written as

$$\begin{aligned} &\lambda |\partial_{\boldsymbol{x}}|^{\beta/4} \left(\left| |\partial_{\boldsymbol{x}}|^{\beta/4} \psi_{\boldsymbol{x}} \right|^2 |\partial_{\boldsymbol{x}}|^{\beta/4} \psi_{\boldsymbol{x}} \right) = \\ &\lambda |\partial_{\boldsymbol{x}}|^{\beta/4} \left(\sum_{\boldsymbol{k}_1 \in \Lambda_L^2} |\boldsymbol{k}_1|^{\beta/4} \hat{\psi}_{\boldsymbol{1}}(t) e^{i\boldsymbol{k}_1 \cdot \boldsymbol{x}} \sum_{\boldsymbol{k}_2 \in \Lambda_L^2} |\boldsymbol{k}_2|^{\beta/4} \hat{\psi}_{\boldsymbol{2}}(t) e^{i\boldsymbol{k}_2 \cdot \boldsymbol{x}} \sum_{\boldsymbol{k}_3 \in \Lambda_L^2} |\boldsymbol{k}_3|^{\beta/4} \hat{\psi}^*_{\boldsymbol{3}}(t) e^{-i\boldsymbol{k}_3 \cdot \boldsymbol{x}} \right), \end{aligned} \tag{2.7}$$

where $\hat{\psi}_{\boldsymbol{2}}(t) \equiv \hat{\psi}(\boldsymbol{k}_2, t)$ and $\hat{\psi}^*_{\boldsymbol{k}}(t)$ is the complex conjugate ($c.c.$) of $\hat{\psi}_{\boldsymbol{k}}(t)$. Recognizing (2.7) contains sums over strictly independent wave numbers, the terms can be reordered as

$$\begin{aligned} &\lambda |\partial_{\boldsymbol{x}}|^{\beta/4} \left(\left| |\partial_{\boldsymbol{x}}|^{\beta/4} \psi_{\boldsymbol{x}} \right|^2 |\partial_{\boldsymbol{x}}|^{\beta/4} \psi_{\boldsymbol{x}} \right) = \\ &\lambda |\partial_{\boldsymbol{x}}|^{\beta/4} \left(\sum_{\boldsymbol{k}_1 \in \Lambda_L^2} \sum_{\boldsymbol{k}_2 \in \Lambda_L^2} \sum_{\boldsymbol{k}_3 \in \Lambda_L^2} (k_1 k_2 k_3)^{\beta/4} \hat{\psi}_{\boldsymbol{1}} \hat{\psi}_{\boldsymbol{2}} \hat{\psi}^*_{\boldsymbol{3}} e^{i(\boldsymbol{k}_1 + \boldsymbol{k}_2 - \boldsymbol{k}_3) \cdot \boldsymbol{x}} \right), \end{aligned} \tag{2.8}$$

where we have simplified our notation by defining $k_i \equiv |\boldsymbol{k}_i|$ for $i = 1, 2, 3$. Writing out the full MMT equation, we now have

$$\sum_{\boldsymbol{k} \in \Lambda_L^2} i\frac{\partial \hat{\psi}_{\boldsymbol{k}}}{\partial t} e^{i\boldsymbol{k} \cdot \boldsymbol{x}} = \sum_{\boldsymbol{k} \in \Lambda_L^2} k^{\alpha} \hat{\psi}_{\boldsymbol{k}} e^{i\boldsymbol{k} \cdot \boldsymbol{x}} + \lambda |\partial_{\boldsymbol{x}}|^{\beta/4} \left(\sum_{\boldsymbol{k}_1 \in \Lambda_L^2} \sum_{\boldsymbol{k}_2 \in \Lambda_L^2} \sum_{\boldsymbol{k}_3 \in \Lambda_L^2} (k_1 k_2 k_3)^{\beta/4} \hat{\psi}_{\boldsymbol{1}} \hat{\psi}_{\boldsymbol{2}} \hat{\psi}^*_{\boldsymbol{3}} e^{i(\boldsymbol{k}_1 + \boldsymbol{k}_2 - \boldsymbol{k}_3) \cdot \boldsymbol{x}} \right). \tag{2.9}$$

To simplify this equation further, the nonlinear term must be written as a sum over $\boldsymbol{k}$. The intuition behind this is that we would like to exploit the orthogonality of each term in the Fourier series, which requires us to know each Fourier coefficient of the nonlinear term corresponding to mode $\boldsymbol{k}$.

We achieve this with the Kroeneker delta function δ_K, such that

$$\begin{aligned}\sum_{\boldsymbol{k}\in\Lambda_L^2} i\frac{\partial\hat{\psi}_{\boldsymbol{k}}}{\partial t}e^{i\boldsymbol{k}\cdot\boldsymbol{x}} &= \sum_{\boldsymbol{k}\in\Lambda_L^2} k^\alpha\hat{\psi}_{\boldsymbol{k}}e^{i\boldsymbol{k}\cdot\boldsymbol{x}} \\ +\lambda\sum_{\boldsymbol{k}\in\Lambda_L^2}\sum_{\boldsymbol{k}_1\in\Lambda_L^2}\sum_{\boldsymbol{k}_2\in\Lambda_L^2}\sum_{\boldsymbol{k}_3\in\Lambda_L^2}&(k_1k_2k_3k)^{\beta/4}\hat{\psi}_{\boldsymbol{1}}\hat{\psi}_{\boldsymbol{2}}\hat{\psi}^*_{\boldsymbol{3}}\delta_K(\boldsymbol{k}_1+\boldsymbol{k}_2-\boldsymbol{k}_3-\boldsymbol{k})e^{i\boldsymbol{k}\cdot\boldsymbol{x}},\end{aligned} \tag{2.10}$$

where we have further made use of the identity (2.4), and we have set $k_i = |\boldsymbol{k}_i|$. Now, by orthogonality of the Fourier series, we arrive at the evolution equation for the Fourier coefficients,

$$i\frac{\partial\hat{\psi}_{\boldsymbol{k}}}{\partial t} = k^\alpha\hat{\psi}_{\boldsymbol{k}} + \lambda\sum_{\boldsymbol{k}_1\in\Lambda_L^2}\sum_{\boldsymbol{k}_2\in\Lambda_L^2}\sum_{\boldsymbol{k}_3\in\Lambda_L^2}(k_1k_2k_3k)^{\beta/4}\hat{\psi}_{\boldsymbol{1}}\hat{\psi}_{\boldsymbol{2}}\hat{\psi}^*_{\boldsymbol{3}}\delta_K(\boldsymbol{k}_1+\boldsymbol{k}_2-\boldsymbol{k}_3-\boldsymbol{k}). \tag{2.11}$$

A few comments are in order. First, if $\lambda = 0$ as in the linear case, we can see that each Fourier mode evolves independently according to $\hat{\psi}_{\boldsymbol{k}}(t) = \hat{\psi}_{\boldsymbol{k}}(0)e^{-i\omega_k t}$, where the dispersion relation is $\omega_k = k^\alpha$. The linear case is fully integrable. When $\lambda \neq 0$, the cubic nonlinearity produces *mode coupling*. This mode coupling takes the form of 4 wave interactions, as a sum over permutations of 3 Fourier modes determines the evolution of a 4th mode (mode $\boldsymbol{k}$). As promised in Section 1.3, the wave number condition, present in the Kronecker delta function, exists long before the kinetic limit is taken in the WKE derivation. When there are many modes involved in the field, as is typical in wave turbulence, analytical treatment of the dynamics becomes very difficult. This will be touched upon in a Section 2.3 when we derive the WKE, however at present we will move on to methods for the numerical evaluation of (2.11).

2.2 Numerical Evaluation of the MMT model

First, we remind the reader that, for (2.1) evaluated on a domain with periodic boundary conditions, we can equivalently solve (2.11), and then use the Fourier series (2.3) to obtain a solution to the original PDE. Because so much of WTT describes spectral behavior, directly simulating (2.11) is often preferable! The equivalence between solutions to (2.1) and (2.11) is the key step behind the pseudospectral method that has been widely employed to study nonlinear dispersive wave equations on simple, periodic domains [e.g., 61, 100, 88, 87].

The basic idea of the pseudospectral method is as follows: (2.1) is first discretized via the Fourier transform, where our solution is represented as a trunacted lattice of Fourier modes. By truncated, we mean that the Fourier series contains terms only up to some maximum wave number in each direction. Suppose this lattice contains M total modes. The resulting large system of M ODEs (2.11) is coupled only through the nonlinear term, and a naive (direct) evaluation requires

$O(M^4)$ total operations. To avoid this extreme computational expense, one evaluates the nonlinear term in (2.11) in physical domain (i.e., one evaluates the nonlinear term in (2.1)). In practice, this requires first applying a inverse Discrete Fourier Transform (inverse DFT), requiring $O(M \log M)$ operations. Once the values of this nonlinear term are computed, one can take the DFT of the term in physical domain to obtain the desired term in Fourier domain. The resulting total computational complexity of each RHS evaluation of (2.11) is a reasonable $O(M \log M)$.

For $\alpha > 1$, however, the above scheme is stiff due to the linear dynamics occurring at widely separated timescales for even a modest number of Fourier modes. This is treated by the use of an integration factor. Rather than solving (2.11), one first makes the transformation $\hat{\phi}_{\boldsymbol{k}} = \hat{\psi}_{\boldsymbol{k}} e^{i\omega_k t}$, where $\phi_{\boldsymbol{k}}$ evolves according to

$$i\frac{\partial \hat{\phi}_{\boldsymbol{k}}}{\partial t} = \lambda e^{i\omega_k t} \sum_{\boldsymbol{k}_1 \in \Lambda_L^2} \sum_{\boldsymbol{k}_2 \in \Lambda_L^2} \sum_{\boldsymbol{k}_3 \in \Lambda_L^2} (k_1 k_2 k_3 k)^{\beta/4} \hat{\phi}_{\boldsymbol{1}} \hat{\phi}_{\boldsymbol{2}} \hat{\phi}^*_{\boldsymbol{3}} e^{-i(\omega_1+\omega_2-\omega_3)t} \delta_K(\boldsymbol{k}_1 + \boldsymbol{k}_2 - \boldsymbol{k}_3 - \boldsymbol{k}). \quad (2.12)$$

If we denote the operator $\mathcal{F}$ as the DFT, one can easily rewrite the above equation as

$$i\frac{\partial \hat{\phi}_{\boldsymbol{k}}}{\partial t} = \lambda k^{\beta/4} e^{i\omega_k t} \mathcal{F}\left\{ \left| \mathcal{F}^{-1}\left\{ k^{\beta/4} \hat{\phi}_{\boldsymbol{k}} e^{-i\omega_k t} \right\} \right|^2 \mathcal{F}^{-1}\left\{ k^{\beta/4} \hat{\phi}_{\boldsymbol{k}} e^{-i\omega_k t} \right\} \right\}, \quad (2.13)$$

the RHS of which can be explicitly evaluated over a truncated Fourier space (i.e., the wave number lattice Λ_L truncated to M modes). To propagate (2.13) forward in time, we use a 4-th order Runge-Kutta scheme.

To create a (quasi-) steady forward energy cascade and an accompanying power-law spectrum it is necessary to first add dissipation at the small scales of the simulation (large k) of the MMT model. For the studies in Chapters 4 and 5, we will additionally force the MMT equation at the large scale, to produce a statistically stationary spectrum. This forcing will also be accompanied by dissipation at the largest scales (lowest k), such that the inverse cascade does not accumulate energy near the 0 mode. Thus, rather than solving (2.11), we instead solve

$$i\frac{\partial \hat{\psi}_{\boldsymbol{k}}}{\partial t} = k^\alpha \hat{\psi}_{\boldsymbol{k}} + \lambda \sum_{\boldsymbol{k}_1 \in \Lambda_L^2} \sum_{\boldsymbol{k}_2 \in \Lambda_L^2} \sum_{\boldsymbol{k}_3 \in \Lambda_L^2} (k_1 k_2 k_3 k)^{\beta/4} \hat{\psi}_{\boldsymbol{1}} \hat{\psi}_{\boldsymbol{2}} \hat{\psi}^*_{\boldsymbol{3}} \delta_K(\boldsymbol{k}_1 + \boldsymbol{k}_2 - \boldsymbol{k}_3 - \boldsymbol{k}) + iF_{\boldsymbol{k}} - i\nu_{\boldsymbol{k}} \hat{\psi}_{\boldsymbol{k}}, \quad (2.14)$$

where $F_{\boldsymbol{k}}$ is white-noise type forcing, and $\nu_{\boldsymbol{k}}$ is the wave number dependent dissipation parameter. The form of $\nu_{\boldsymbol{k}}$ will change slightly in subsequent chapters, and will be discussed at that time. It is important, however, that ν_k be chosen to be effectively (or exactly) zero in the inertial range. The white noise forcing is applied from some $k_{f1} \leq k \leq k_{f2}$ at the large scale, where $F_{\boldsymbol{k}}$ at each mode and each time step is taken from a Gaussian distribution of 0 mean and standard deviation σ_F that

determines the forcing strength. Following the work in [61], we can modify our scheme (2.13) to solve (2.14) via

$$i\frac{\partial\hat{\phi}_{\boldsymbol{k}}}{\partial t} = e^{(-\nu_k+i\omega_k)t}\left(\lambda k^{\beta/4}\mathcal{F}\left\{\left|\mathcal{F}^{-1}\left\{k^{\beta/4}\hat{\phi}_{\boldsymbol{k}}e^{-i\omega_k t}\right\}\right|^2\mathcal{F}^{-1}\left\{k^{\beta/4}\hat{\phi}_{\boldsymbol{k}}e^{-i\omega_k t}\right\}\right\} + iF_{\boldsymbol{k}}\right). \tag{2.15}$$

Finally, we note that a suitable dealiasing scheme is needed for the evaluation of (2.13) and (2.15). See Appendix C for a detailed discussion. Next, we discuss the derivation of the WKE.

2.3 Derivation of the Wave Kinetic Equation

This derivation will follow [73], which, in our opinion, provides a relatively straightforward derivation without sacrificing much in the way of rigor within the WT formalism. While more precise and more general derivations are available [69, 30], the advantages of these methods do not justify their added complexity *for the purposes of this dissertation*. In more general theoretical contexts, these more sophisticated derivations have much to offer. Also, neither this derivation nor the more sophisticated derivations just mentioned are truly mathematically rigorous. The mathematically rigorous derivation in [22] is formulated in context of a Cauchy initial value problem, and includes number-theoretic considerations, among many other nuances that will not be discussed here.

This section will make use of a truncated notation for practical reasons. We note that a small amount of this notation will be redefined later in this chapter and dissertation, including θ, which here denotes *angle* (to be defined in a moment) for this section only. The derivation of the WKE begins with the wave number formulation of the MMT model (2.11). We will take this opportunity to write the Hamiltonian density in its wave number form, which is given by

$$H = \sum_{\boldsymbol{k}\in\Lambda_L^2}\hat{H}_2(\boldsymbol{k}) + \sum_{\boldsymbol{k}\in\Lambda_L^2}\hat{H}_4(\boldsymbol{k}) =$$
$$\sum_{\boldsymbol{k}\in\Lambda_L^2}k^{\alpha/2}|\hat{\psi}_{\boldsymbol{k}}|^2 + \varepsilon\frac{\lambda}{2}\sum_{\boldsymbol{k}\in\Lambda_L^2}\sum_{\boldsymbol{k}_1\in\Lambda_L^2}\sum_{\boldsymbol{k}_2\in\Lambda_L^2}\sum_{\boldsymbol{k}_3\in\Lambda_L^2}(k_1k_2k_3k)^{\beta/4}\hat{\psi}_{\boldsymbol{1}}\hat{\psi}_{\boldsymbol{2}}\hat{\psi}^*_{\boldsymbol{3}}\hat{\psi}^*_{\boldsymbol{k}}\delta_K(\boldsymbol{k}_1+\boldsymbol{k}_2-\boldsymbol{k}_3-\boldsymbol{k}), \tag{2.16}$$

where we assume that the nonlinear term is $O(\varepsilon)$ the size of the linear term, where ε is a small quantity. This generally corresponds to a low amplitude solution.

For simplicity of notation, we will rewrite the sums and delta function in (2.16) as

$$H = \sum_{\boldsymbol{k}}k^{\alpha/2}|\hat{\psi}_{\boldsymbol{k}}|^2 + \varepsilon\frac{\lambda}{2}\sum_{\boldsymbol{123k}}(k_1k_2k_3k)^{\beta/4}\hat{\psi}_{\boldsymbol{1}}\hat{\psi}_{\boldsymbol{2}}\hat{\psi}^*_{\boldsymbol{3}}\hat{\psi}^*_{\boldsymbol{k}}\delta^{\boldsymbol{12}}_{\boldsymbol{3k}}.$$

The corresponding wave equation can be written as

$$i\frac{\partial\hat{\psi}_{\boldsymbol{k}}}{\partial t} = k^{\alpha}\hat{\psi}_{\boldsymbol{k}} + \varepsilon\lambda\sum_{\mathbf{123}}(k_1k_2k_3k)^{\beta/4}\hat{\psi}_{\mathbf{1}}\hat{\psi}_{\mathbf{2}}\hat{\psi}^{*}_{\mathbf{3}}\delta^{\mathbf{12}}_{\mathbf{3}\boldsymbol{k}}.$$

We now introduce a canonical transformation to action-angle coordinates, where $\hat{\psi}_{\boldsymbol{k}} = \sqrt{I_{\boldsymbol{k}}}e^{-i\theta_{\boldsymbol{k}}}$, $I_{\boldsymbol{k}}$ is known as the action of degree-of-freedom $\boldsymbol{k}$ (here, each degree-of-freedom is associated with a Fourier mode), and $\theta_{\boldsymbol{k}}$ is known as the *angle* of each degree-of-freedom. Note that action-angle coordinates are quite explicitly an interpretation of the complex Fourier mode $\hat{\psi}_{\boldsymbol{k}}$ in polar form. This is useful because the key statistical assumptions that follow are in easily understood in terms of actions and angles, rather than through a Cartesian interpretation. Under this transformation, the evolution equations for $I_{\boldsymbol{k}}$ and $\theta_{\boldsymbol{k}}$ are now

$$\begin{aligned}\frac{dI_{\boldsymbol{k}}}{dt} &= 2\varepsilon\lambda\sum_{\mathbf{123}}(k_1k_2k_3k)^{\beta/4}\sqrt{I_{\mathbf{1}}I_{\mathbf{2}}I_{\mathbf{3}}I_{\boldsymbol{k}}}\sin\left(\Delta\theta^{\mathbf{3}\boldsymbol{k}}_{\mathbf{12}}\right)\delta^{\mathbf{12}}_{\mathbf{3}\boldsymbol{k}},\\ \frac{d\theta_{\boldsymbol{k}}}{dt} &= \omega_{\boldsymbol{k}} + \varepsilon\lambda\sum_{\mathbf{123}}(k_1k_2k_3k)^{\beta/4}\sqrt{\frac{I_{\mathbf{1}}I_{\mathbf{2}}I_{\mathbf{3}}}{I_{\boldsymbol{k}}}}\cos\left(\Delta\theta^{\mathbf{3}\boldsymbol{k}}_{\mathbf{12}}\right)\delta^{\mathbf{12}}_{\mathbf{3}\boldsymbol{k}},\end{aligned} \tag{2.17}$$

where $\Delta\theta^{\mathbf{3}\boldsymbol{k}}_{\mathbf{12}} = \theta_{\mathbf{3}} + \theta_{\boldsymbol{k}} - \theta_{\mathbf{1}} - \theta_{\mathbf{2}}$. In this new form, one can show that a certain subset of interactions never contribute to action evolution, and contribute to angle evolution independently of the angles themselves. This occurs when $\Delta\theta^{\mathbf{3}\boldsymbol{k}}_{\mathbf{12}} = 0$ identically, i.e., when wave numbers $\boldsymbol{k}_1 = \boldsymbol{k}_3$ and $\boldsymbol{k}_2 = \boldsymbol{k}$, $\boldsymbol{k}_1 = \boldsymbol{k}$ and $\boldsymbol{k}_2 = \boldsymbol{k}_3$, or when all 4 wave numbers are the same. As discussed in [73] and [69], these terms must be properly handled in order to avoid secular growth of the perturbation series at a later stage in the derivation. One avoids this issue by *renormalizing* the dispersion relation by including the effect of these interactions in the definition of ω. As [73] notes, this can be thought of as an application of the widely-employed Poincaré-Linstedt method. Due to the symmetry of indices 1 and 2, we need only consider the first of these cases and define

$$\tilde{\omega}_{\boldsymbol{k}} \equiv k^{\alpha} + \varepsilon\lambda\left(2\sum_{\mathbf{3}}(k_3k)^{\beta/2}I_{\mathbf{3}} - k^{\beta}I_{\boldsymbol{k}}\right). \tag{2.18}$$

We must also remove those corresponding interactions from the sums in (2.17). A summation over the remaining interactions will be denoted with a prime, so that

$$\begin{aligned}\frac{dI_{\boldsymbol{k}}}{dt} &= 2\varepsilon\lambda\sum_{\mathbf{123}}{}'(k_1k_2k_3k)^{\beta/4}\sqrt{I_{\mathbf{1}}I_{\mathbf{2}}I_{\mathbf{3}}I_{\boldsymbol{k}}}\sin\left(\Delta\theta^{\mathbf{3}\boldsymbol{k}}_{\mathbf{12}}\right)\delta^{\mathbf{12}}_{\mathbf{3}\boldsymbol{k}},\\ \frac{d\theta_{\boldsymbol{k}}}{dt} &= \tilde{\omega}_{\boldsymbol{k}} + \varepsilon\lambda\sum_{\mathbf{123}}{}'(k_1k_2k_3k)^{\beta/4}\sqrt{\frac{I_{\mathbf{1}}I_{\mathbf{2}}I_{\mathbf{3}}}{I_{\boldsymbol{k}}}}\cos\left(\Delta\theta^{\mathbf{3}\boldsymbol{k}}_{\mathbf{12}}\right)\delta^{\mathbf{12}}_{\mathbf{3}\boldsymbol{k}},\end{aligned} \tag{2.19}$$

are the action-angle evolution equations written in our new notation.

We now seek the solution to (2.19) at some time t given some initial conditions $\overline{I}_{\boldsymbol{k}} \equiv I_{\boldsymbol{k}}(t=0)$ and $\overline{\theta}_{\boldsymbol{k}} \equiv \theta_{\boldsymbol{k}}(t=0)$. Given that ε is small, we will write an approximate solution as a perturbation (power) series in ε,

$$\begin{aligned} I_{\boldsymbol{k}}(t) &= I_{\boldsymbol{k}}^{(0)}(t) + \varepsilon I_{\boldsymbol{k}}^{(1)}(t) + \varepsilon^2 I_{\boldsymbol{k}}^{(2)}(t) \\ \theta_{\boldsymbol{k}}(t) &= \theta_{\boldsymbol{k}}^{(0)}(t) + \varepsilon \theta_{\boldsymbol{k}}^{(1)}(t) + \varepsilon^2 \theta_{\boldsymbol{k}}^{(2)}(t). \end{aligned} \tag{2.20}$$

By substituting these expressions into (2.19), we can successively obtain expressions for the i-th order coefficients $I_{\boldsymbol{k}}^{(i)}$ and $\theta_{\boldsymbol{k}}^{(i)}$. At 0-th order, we have the linear dynamics given by

$$\begin{aligned} \frac{dI_{\boldsymbol{k}}^{(0)}}{dt} &= 0 \\ \frac{d\theta_{\boldsymbol{k}}^{(0)}}{dt} &= \tilde{\omega}_{\boldsymbol{k}}. \end{aligned} \tag{2.21}$$

This system is easily integrated from the initial conditions to give

$$\begin{aligned} I_{\boldsymbol{k}}^{(0)}(t) &= \overline{I}_{\boldsymbol{k}} \\ \theta_{\boldsymbol{k}}^{(0)}(t) &= \overline{\theta}_{\boldsymbol{k}} + \overline{\tilde{\omega}}_{\boldsymbol{k}} t. \end{aligned} \tag{2.22}$$

With this substituted into (2.19), we now can write the first order evolution equations as

$$\begin{aligned} \frac{dI_{\boldsymbol{k}}^{(1)}}{dt} &= 2\lambda \sum_{\mathbf{123}}{}' (k_1 k_2 k_3 k)^{\beta/4} \sqrt{\overline{I}_{\mathbf{1}} \overline{I}_{\mathbf{2}} \overline{I}_{\mathbf{3}} \overline{I}_{\boldsymbol{k}}} \sin\left(\Delta\overline{\theta}_{\mathbf{12}}^{\mathbf{3}\boldsymbol{k}} + \Delta\overline{\tilde{\omega}}_{\boldsymbol{k}} t\right) \delta_{\mathbf{3}\boldsymbol{k}}^{\mathbf{12}}, \\ \frac{d\theta_{\boldsymbol{k}}^{(1)}}{dt} &= \lambda \sum_{\mathbf{123}}{}' (k_1 k_2 k_3 k)^{\beta/4} \sqrt{\frac{\overline{I}_{\mathbf{1}} \overline{I}_{\mathbf{2}} \overline{I}_{\mathbf{3}}}{\overline{I}_{\boldsymbol{k}}}} \cos\left(\Delta\overline{\theta}_{\mathbf{12}}^{\mathbf{3}\boldsymbol{k}} + \Delta\overline{\tilde{\omega}}_{\boldsymbol{k}} t\right) \delta_{\mathbf{3}\boldsymbol{k}}^{\mathbf{12}}, \end{aligned} \tag{2.23}$$

where $\Delta\overline{\tilde{\omega}}_{\mathbf{12}}^{\mathbf{3}\boldsymbol{k}} = \overline{\tilde{\omega}}_{\mathbf{3}} + \overline{\tilde{\omega}}_{\boldsymbol{k}} - \overline{\tilde{\omega}}_{\mathbf{1}} - \overline{\tilde{\omega}}_{\mathbf{2}}$. Integrating these expression in time, one obtains

$$\begin{aligned} I_{\boldsymbol{k}}^{(1)}(t) &= 2\lambda \sum_{\mathbf{123}}{}' (k_1 k_2 k_3 k)^{\beta/4} \sqrt{\overline{I}_{\mathbf{1}} \overline{I}_{\mathbf{2}} \overline{I}_{\mathbf{3}} \overline{I}_{\boldsymbol{k}}} \frac{\cos\left(\Delta\overline{\theta}_{\mathbf{12}}^{\mathbf{3}\boldsymbol{k}}\right) - \cos\left(\Delta\overline{\theta}_{\mathbf{12}}^{\mathbf{3}\boldsymbol{k}} + \Delta\overline{\tilde{\omega}}_{\boldsymbol{k}} t\right)}{\Delta\overline{\tilde{\omega}}_{\mathbf{12}}^{\mathbf{3}\boldsymbol{k}}} \delta_{\mathbf{3}\boldsymbol{k}}^{\mathbf{12}}, \\ \theta_{\boldsymbol{k}}^{(1)}(t) &= \lambda \sum_{\mathbf{123}}{}' (k_1 k_2 k_3 k)^{\beta/4} \sqrt{\frac{\overline{I}_{\mathbf{1}} \overline{I}_{\mathbf{2}} \overline{I}_{\mathbf{3}}}{\overline{I}_{\boldsymbol{k}}}} \frac{\sin\left(\Delta\overline{\theta}_{\mathbf{12}}^{\mathbf{3}\boldsymbol{k}} + \Delta\overline{\tilde{\omega}}_{\mathbf{12}}^{\mathbf{3}\boldsymbol{k}} t\right) - \sin\left(\Delta\overline{\theta}_{\mathbf{12}}^{\mathbf{3}\boldsymbol{k}}\right)}{\Delta\overline{\tilde{\omega}}_{\mathbf{12}}^{\mathbf{3}\boldsymbol{k}}} \delta_{\mathbf{3}\boldsymbol{k}}^{\mathbf{12}}. \end{aligned} \tag{2.24}$$

Finally, the evolution of $I_{\boldsymbol{k}}^{(2)}(t)$, after a great deal of reduction, is given by

$$\begin{aligned}\frac{dI_{\boldsymbol{k}}^{(2)}}{dt} = 2\lambda^2 \sum_{\mathbf{123}}{}' \sum_{\mathbf{456}}{}' \sum_{m=1}^{4} (k_1k_2k_3k)^{\beta/4}(k_4k_5k_6k_m)^{\beta/4}\sqrt{\frac{\bar{I}_{\mathbf{1}}\bar{I}_{\mathbf{2}}\bar{I}_{\mathbf{3}}\bar{I}_{\boldsymbol{k}}\bar{I}_{\mathbf{4}}\bar{I}_{\mathbf{5}}\bar{I}_{\mathbf{6}}}{\bar{I}_{\boldsymbol{m}}}} \\ \times \frac{\sin\left(\sigma_m\Delta\bar{\theta}_{\mathbf{45}}^{\mathbf{6}\boldsymbol{m}} - \Delta\bar{\theta}_{\mathbf{12}}^{\mathbf{3}\boldsymbol{k}} + (\sigma_m\Delta\bar{\tilde{\omega}}_{\mathbf{45}}^{\mathbf{6}\boldsymbol{m}} - \Delta\bar{\tilde{\omega}}_{\mathbf{12}}^{\mathbf{3}\boldsymbol{k}})t\right)}{\Delta\bar{\tilde{\omega}}_{\mathbf{45}}^{\mathbf{6}\boldsymbol{m}}}\delta_{\mathbf{45}}^{\mathbf{6}\boldsymbol{m}}\delta_{\mathbf{3}\boldsymbol{k}}^{\mathbf{12}},\end{aligned} \tag{2.25}$$

where the pre-factor $\sigma_m = +1, +1, -1, -1$ for $m = 1, 2, 3, 4$. At this point, we may stop, as the evolution of $\theta_{\boldsymbol{k}}^{(2)}$ would not be used. We also need not explicitly integrate this equation, as we only require a second-order accurate evolution equation for $I_{\boldsymbol{k}}$,

$$\frac{dI_{\boldsymbol{k}}}{dt} = \varepsilon\frac{dI_{\boldsymbol{k}}^{(1)}}{dt} + \varepsilon^2\frac{dI_{\boldsymbol{k}}^{(2)}}{dt} + O(\varepsilon^3), \tag{2.26}$$

and we have already achieved this goal.

We proceed by assuming, at $t = 0$, that the angles of each mode are independent and uniformly distributed. We are interested in the quantity

$$\langle\frac{dI_{\boldsymbol{k}}}{dt}\rangle_{\bar{\theta}} = \varepsilon\langle\frac{dI_{\boldsymbol{k}}^{(1)}}{dt}\rangle_{\bar{\theta}} + \varepsilon^2\langle\frac{dI_{\boldsymbol{k}}^{(2)}}{dt}\rangle_{\bar{\theta}} + O(\varepsilon^3), \tag{2.27}$$

where $\langle\cdot\rangle_{\bar{\theta}}$ denotes an ensemble average of some observable (e.g., $I_{\boldsymbol{k}}$) over the uniformly distributed, independent initial angles. Beginning with the first order term, we can see using the linearity of expectation that $\langle\frac{dI_{\boldsymbol{k}}^{(1)}}{dt}\rangle_{\bar{\theta}}$ is determined by $\langle\sin\left(\Delta\bar{\theta}_{\mathbf{12}}^{\mathbf{3}\boldsymbol{k}}\right)\rangle_{\bar{\theta}} = \mathrm{Im}\langle e^{i\Delta\bar{\theta}_{\mathbf{12}}^{\mathbf{3}\boldsymbol{k}}}\rangle_{\bar{\theta}} = 0$, as $e^{i\Delta\bar{\theta}_{\mathbf{12}}^{\mathbf{3}\boldsymbol{k}}}$ is uniformly distributed on the unit circle. Thus, $\langle\frac{dI_{\boldsymbol{k}}^{(1)}}{dt}\rangle_{\bar{\theta}} = 0$ and the leading order contribution to $\langle\frac{dI_{\boldsymbol{k}}}{dt}\rangle_{\bar{\theta}}$ is $O(\varepsilon^2)$. The angle average of the second order term can be written in complex notation as

$$\langle\frac{dI_{\boldsymbol{k}}^{(2)}}{dt}\rangle_{\bar{\theta}} = 2\lambda^2\mathrm{Im}\left[\sum_{\mathbf{123}}{}' \sum_{\mathbf{456}}{}' \sum_{m=1}^{4} (k_1k_2k_3k)^{\beta/4}(k_4k_5k_6k_m)^{\beta/4}\sqrt{\frac{\bar{I}_{\mathbf{1}}\bar{I}_{\mathbf{2}}\bar{I}_{\mathbf{3}}\bar{I}_{\boldsymbol{k}}\bar{I}_{\mathbf{4}}\bar{I}_{\mathbf{5}}\bar{I}_{\mathbf{6}}}{\bar{I}_{\boldsymbol{m}}}}\right. \tag{2.28}$$

$$\left. \times \frac{(e^{i\sigma_m\Delta\bar{\tilde{\omega}}_{\mathbf{45}}^{\mathbf{6}\boldsymbol{m}}} - 1)e^{-i\Delta\bar{\tilde{\omega}}_{\mathbf{12}}^{\mathbf{3}\boldsymbol{k}}t}}{\Delta\bar{\tilde{\omega}}_{\mathbf{45}}^{\mathbf{6}\boldsymbol{m}}}\langle e^{i(\sigma_m\Delta\bar{\theta}_{\mathbf{45}}^{\mathbf{6}\boldsymbol{m}} - \Delta\bar{\theta}_{\mathbf{12}}^{\mathbf{3}\boldsymbol{k}})}\rangle_{\bar{\theta}}\delta_{\mathbf{45}}^{\mathbf{6}\boldsymbol{m}}\delta_{\mathbf{3}\boldsymbol{k}}^{\mathbf{12}}\right], \tag{2.29}$$

Each term in m must be averaged separately. For $m = 1$, the term to be averaged is

$$\langle e^{i(\sigma_m\Delta\bar{\theta}_{\mathbf{45}}^{\mathbf{6}\boldsymbol{m}} - \Delta\bar{\theta}_{\mathbf{12}}^{\mathbf{3}\boldsymbol{k}})}\rangle_{\bar{\theta}} = \langle e^{i\Delta\bar{\theta}_{\mathbf{452}}^{\mathbf{63}\boldsymbol{k}}}\rangle_{\bar{\theta}}. \tag{2.30}$$

This term will evaluate to zero unless the wave number indices match such that $\bar{\theta}_{\mathbf{452}}^{\mathbf{63}\boldsymbol{k}} = 0$ identically,

in which case the average is 1. If one considers all 4 values of m and sums the result, one can directly write the expression for $\langle \frac{dI_{\boldsymbol{k}}}{dt} \rangle_{\overline{\theta}}$,

$$\langle \frac{dI_{\boldsymbol{k}}}{d\tau} \rangle_{\overline{\theta}} = 4\lambda^2 \sum_{\mathbf{123}} (k_1 k_2 k_3 k)^{\beta/2} \overline{I}_{\mathbf{1}} \overline{I}_{\mathbf{2}} \overline{I}_{\mathbf{3}} \overline{I}_{\boldsymbol{k}} \left(\frac{1}{\overline{I}_{\boldsymbol{k}}} + \frac{1}{\overline{I}_{\mathbf{3}}} - \frac{1}{\overline{I}_{\mathbf{1}}} - \frac{1}{\overline{I}_{\mathbf{2}}} \right) \frac{\sin\left(\Delta\overline{\tilde{\omega}}^{\mathbf{3k}}_{\mathbf{12}} \tau / \varepsilon^2 \right)}{\Delta\overline{\tilde{\omega}}^{\mathbf{3k}}_{\mathbf{12}}} \delta^{\mathbf{12}}_{\mathbf{3k}}, \tag{2.31}$$

where we have made the substitution $\tau = \varepsilon^2 t$, which is known as the kinetic time. We also note that the primed sum, which excludes certain diagonal interactions, is no longer necessary because those interaction cancel.

This is a very important stage in the derivation, as we have not made any assumptions about the size of the domain - only its statistics, and that the nonlinearity is sufficiently small that the perturbation series (2.20) remains well-ordered. As we will see later in this chapter, a formula similar to (2.31) can be used to study the closure function $\sin\left(\Delta\overline{\tilde{\omega}}^{\mathbf{3k}}_{\mathbf{12}} \tau / \varepsilon^2 \right) / \Delta\overline{\tilde{\omega}}^{\mathbf{3k}}_{\mathbf{12}}$ to assess validity of the WT closure when realized in the MMT model on a periodic domain. The derivation continues with the taking of the large box limit, followed by the weak nonlinearity limit.

The large box limit, where $L \to \infty$, can equivalently be formulated as $\Delta k^d \to 0$, where Δk^d is the volume of Fourier domain occupied by mode $\boldsymbol{k}$. This latter formulation is particularly useful, because we will define (with a slight abuse of notation) action *density* to be

$$I'_{\boldsymbol{k}} \equiv \frac{I_{\boldsymbol{k}}}{\Delta k^d}. \tag{2.32}$$

In the large box limit, $I'_{\boldsymbol{k}}$ is a function of continuous $k \in \mathbb{R}^d$. As $\Delta k^d \to 0$ sums become integrals and Kronecker delta functions become Dirac delta functions according to the rules specified in [73, 69, 30]. Making these substitutions and dropping the primes from our notation, we obtain

$$\langle \frac{\partial I_{\boldsymbol{k}}}{\partial \tau} \rangle_{\overline{\theta}} = 4\lambda^2 \int_{\mathbf{123}} (k_1 k_2 k_3 k)^{\beta/2} \overline{I}_{\mathbf{1}} \overline{I}_{\mathbf{2}} \overline{I}_{\mathbf{3}} \overline{I}_{\boldsymbol{k}} \left(\frac{1}{\overline{I}_{\boldsymbol{k}}} + \frac{1}{\overline{I}_{\mathbf{3}}} - \frac{1}{\overline{I}_{\mathbf{1}}} - \frac{1}{\overline{I}_{\mathbf{2}}} \right) \frac{\sin\left(\Delta\overline{\omega}^{\mathbf{3k}}_{\mathbf{12}} \tau / \varepsilon^2 \right)}{\Delta\overline{\omega}^{\mathbf{3k}}_{\mathbf{12}}} \delta^{\mathbf{12}}_{\mathbf{3k}} d\boldsymbol{k}_1 d\boldsymbol{k}_2 d\boldsymbol{k}_3. \tag{2.33}$$

We also note here that [73] demonstrates convincingly that use of the renormalized frequency is not necessary after the large box limit is taken provided that $\lim_{\substack{\Delta k^d \to 0 \\ \varepsilon \to 0}} \Delta k^d / \varepsilon = 0$, e.g., the large-box limit is taken before the weak nonlinearity limit. Thus, we use the linear dispersion relation in the resonance condition for the remainder of this dissertation. This same conclusion is not reached via other, equally compelling derivations [69, 12], however (see section 3.3.3 in [12] for a detailed discussion). This discrepancy appears to be related to the manner in which the $L \to \infty$ and $\varepsilon \to 0$ limits are taken. It is typical of "physicists" derivations such as this one to take the large-box limit first, followed by the $\varepsilon \to 0$ limit, citing the intuition developed in Chapter 1 regarding the

importance of quasi-resonance. On the other hand, the rigorous derivation in [22] takes the kinetic limit more carefully, according to a scaling law between L and ε. While we leave the open questions regarding the rigorous and justified use of frequency renormalization to future study, we have been careful throughout the work of this dissertation to verify that our results do not meaningfully change when the renormalized dispersion relation is used. For a system with $\beta = 0$, as used in Chapter 5, the normalized frequency contributions to the resonance condition cancel, and renormalization is not strictly needed in the WKE.

This discrepancy regarding frequency renormalization is complicated in part because the form of the generalized delta function is one of the primary differences between the various WKE derivations [101, 47, 69, 73]. Here, it takes the form $\sin\left(\Delta\overline{\omega}^{\boldsymbol{3k}}_{\boldsymbol{12}}\tau/\varepsilon^2\right)/\Delta\overline{\omega}^{\boldsymbol{3k}}_{\boldsymbol{12}}$. We refer to this function as a generalized delta function because, in the weak nonlinearity limit, we have that

$$\lim_{\varepsilon\to 0}\frac{\sin\left(\Delta\overline{\omega}^{\boldsymbol{3k}}_{\boldsymbol{12}}\tau/\varepsilon^2\right)}{\Delta\overline{\omega}^{\boldsymbol{3k}}_{\boldsymbol{12}}} = \pi\delta(\Delta\overline{\omega}^{\boldsymbol{3k}}_{\boldsymbol{12}}). \tag{2.34}$$

We now take the limit $\varepsilon \to 0$, and obtain

$$\langle\frac{\partial I_{\boldsymbol{k}}}{\partial\tau}\rangle_{\overline{\theta}} = 4\pi\lambda^2\int_{\boldsymbol{123}}(k_1k_2k_3k)^{\beta/2}\overline{I}_{\boldsymbol{1}}\overline{I}_{\boldsymbol{2}}\overline{I}_{\boldsymbol{3}}\overline{I}_{\boldsymbol{k}}\left(\frac{1}{\overline{I}_{\boldsymbol{k}}}+\frac{1}{\overline{I}_{\boldsymbol{3}}}-\frac{1}{\overline{I}_{\boldsymbol{1}}}-\frac{1}{\overline{I}_{\boldsymbol{2}}}\right)\delta(\Delta\overline{\omega}^{\boldsymbol{3k}}_{\boldsymbol{12}})\delta^{\boldsymbol{12}}_{\boldsymbol{3k}}d\boldsymbol{k}_1d\boldsymbol{k}_2d\boldsymbol{k}_3. \tag{2.35}$$

The final step of this derivation is to interpret the action density $\langle I_{\boldsymbol{k}}\rangle_{\overline{\theta}}$ as a stochastic random variable of some distribution whose expected value (ensemble average) we are now interested in. Thus, we take the ensemble average $\langle\cdot\rangle_{\overline{I},\overline{\theta}}$ of (2.35), under the assumption that the amplitudes of each Fourier component are independent. This leads to an equation for wave action spectrum evolution, where $n_{\boldsymbol{k}} \equiv \langle I_{\boldsymbol{k}}\rangle_{\overline{I},\overline{\theta}}$, which is given by

$$\frac{\partial n_{\boldsymbol{k}}}{\partial\tau} = 4\pi\lambda^2\int_{\boldsymbol{123}}(k_1k_2k_3k)^{\beta/2}\overline{n}_{\boldsymbol{1}}\overline{n}_{\boldsymbol{2}}\overline{n}_{\boldsymbol{3}}\overline{n}_{\boldsymbol{k}}\left(\frac{1}{\overline{n}_{\boldsymbol{k}}}+\frac{1}{\overline{n}_{\boldsymbol{3}}}-\frac{1}{\overline{n}_{\boldsymbol{1}}}-\frac{1}{\overline{n}_{\boldsymbol{2}}}\right)\delta(\Delta\overline{\omega}^{\boldsymbol{3k}}_{\boldsymbol{12}})\delta^{\boldsymbol{12}}_{\boldsymbol{3k}}d\boldsymbol{k}_1d\boldsymbol{k}_2d\boldsymbol{k}_3. \tag{2.36}$$

An interesting feature of the system is that the WKE is agnostic to the sign of the nonlinearity, as $\lambda^2 = 1$. While the sign of the nonlinearity affects the emergence of coherent structures in the MMT model [87], it does not change the limiting kinetic description of the field. Thus, it will be omitted from the WKE from the remainder of this work. As a last step, we assume that the our previous assumption of initially random phases and amplitudes (RPA) persists over kinetic timescale τ, allowing us to substitute the initial wave action spectrum $\overline{n}_{\boldsymbol{k}}$ for its values at later times $n_{\boldsymbol{k}}$. See [30] for additional commentary on the validity of this assumption. This last step leads us

to the WKE for the MMT system, now written with more explicit conventions,

$$\frac{\partial n_{\boldsymbol{k}}}{\partial t} = 4\pi \int_{-\infty}^{\infty}\int_{-\infty}^{\infty}\int_{-\infty}^{\infty} (k_1 k_2 k_3 k)^{\beta/2} n_{\boldsymbol{1}} n_{\boldsymbol{2}} n_{\boldsymbol{3}} n_{\boldsymbol{k}} \left(\frac{1}{n_{\boldsymbol{k}}} + \frac{1}{n_{\boldsymbol{3}}} - \frac{1}{n_{\boldsymbol{1}}} - \frac{1}{n_{\boldsymbol{2}}}\right) \times \delta(\omega_1 + \omega_2 - \omega_3 - \omega_k)\delta(\boldsymbol{k}_1 + \boldsymbol{k}_2 - \boldsymbol{k}_3 - \boldsymbol{k}) d\boldsymbol{k}_1 d\boldsymbol{k}_2 d\boldsymbol{k}_3, \tag{2.37}$$

where we replace τ with t, as is conventional, with an understanding that the evolution is with respect to the kinetic time.

2.4 The Kolmogorov-Zakharov Spectra

While the forward KZ spectrum $n_k = C_0 P^{\theta_0} k^{\gamma_0}$ can be found in the general case given (α, β) and dimension d, we will focus our attention on the case of $d = 1$, $\alpha = 1/2$, and $\beta = 0$. This is the system we will study in Chapter 5, and this is the only system we study for which we choose to derive the Kolmogorov Constant C_0, which first requires us to derive γ_0 and θ_0. We will present a more general formula for γ_0 at the end of this section. Much of the following derivation reflects that of [100], however with substantially more detail provided and a correction included.

The derivation of the KZ spectrum typically begins by assuming an isotropic spectrum $n_k = n_{-k}$, though it is in general possible to derive an anisotropic WKEs for anisotropic systems [69]. For $d = 1$, this is done by considering all the possible positive and negative combinations of the wave number condition over which the WKE integrates. Each of $\boldsymbol{k}_1$, $\boldsymbol{k}_2$, and $\boldsymbol{k}_3$ can take a positive or negative sign in the delta function of (2.37), producing 8 possibilities. However, not every combination of these signs produces a non-trivial resonance. A trivial resonance is one that satisfies the resonance conditions (1.3) and (1.4) by having $\boldsymbol{k}_1 = \boldsymbol{k}_3$ and $\boldsymbol{k}_2 = \boldsymbol{k}$, or $\boldsymbol{k}_2 = \boldsymbol{k}_3$ and $\boldsymbol{k}_1 = \boldsymbol{k}$. Although the delta functions in the WKE are non-zero in these cases, the integrand of (2.37) take a zero value, and thus these case can be ignored. After these trivial cases are removed, we are left with

$$\begin{aligned}\frac{\partial n_k}{\partial t} = 4\pi \int_0^{\infty}\int_0^{\infty}\int_0^{\infty} n_1 n_2 n_3 n_k \left(\frac{1}{n_k} + \frac{1}{n_3} - \frac{1}{n_1} - \frac{1}{n_2}\right) \delta(\omega_1 + \omega_2 - \omega_3 - \omega_k) \\ \times \left(\delta(k_1 + k_2 + k_3 - k) + \delta(k_1 - k_2 - k_3 - k) + \delta(-k_1 + k_2 - k_3 - k) \right. \\ \left. + \delta(-k_1 - k_2 + k_3 - k)\right) dk_1 dk_2 dk_3.\end{aligned} \tag{2.38}$$

it will later become important to integrate over the resonant manifold, which is much easier to interpret as quadratic functions in ω. Therefore, we next rewrite the above equation as an integral over ω, and replace (on the LHS) n_k, the spectral density in k, with $\mathcal{N}_\omega$, the spectral density in ω.

This leads to

$$\frac{\partial \mathcal{N}_\omega}{\partial t} = 128\pi \int_0^\infty \int_0^\infty \int_0^\infty (\omega_1\omega_2\omega_3\omega) n_1 n_2 n_3 n_\omega \left(\frac{1}{n_\omega} + \frac{1}{n_3} - \frac{1}{n_1} - \frac{1}{n_2}\right) \delta(\omega_1 + \omega_2 - \omega_3 - \omega) \times \Big(\delta(\omega_1^2 + \omega_2^2 + \omega_3^2 - \omega^2) + \delta(\omega_1^2 - \omega_2^2 - \omega_3^2 - \omega^2) + \delta(-\omega_1^2 + \omega_2^2 - \omega_3^2 - \omega^2) + \delta(-\omega_1^2 - \omega_2^2 + \omega_3^2 - \omega^2)\Big) d\omega_1 d\omega_2 d\omega_3, \tag{2.39}$$

where $n_\omega = n(k(\omega))$, and we have used the facts that $dk = 2\omega d\omega$ and $\mathcal{N}(\omega)d\omega = n(k)dk + n(-k)dk = 2n(k)dk$. We note that the factor of 2 on the spectral element relation is necessary for a consistent and correct flux definition. We also note that, by our spectral element definition, n_k and n_ω are angle-averaged while $\mathcal{N}(\omega)$ is angle-integrated.

With a slight abuse of notation, we assume that $n_\omega = A\omega^\gamma$, where γ refers to an arbitrary exponent that later will become the KZ exponents γ_0 and γ_1. Substituting this into (2.39), we are left with

$$\frac{\partial \mathcal{N}_\omega}{\partial t} = 128\pi A^3 \int_0^\infty \int_0^\infty \int_0^\infty \omega_1^{\gamma+1}\omega_2^{\gamma+1}\omega_3^{\gamma+1}\omega^{\gamma+1} \left(\omega^{-\gamma} + \omega_3^{-\gamma} - \omega_1^{-\gamma} - \omega_2^{-\gamma}\right) \delta(\omega_1 + \omega_2 - \omega_3 - \omega) \times \Big(\delta(\omega_1^2 + \omega_2^2 + \omega_3^2 - \omega^2) + \delta(\omega_1^2 - \omega_2^2 - \omega_3^2 - \omega^2) + \delta(-\omega_1^2 + \omega_2^2 - \omega_3^2 - \omega^2) + \delta(-\omega_1^2 - \omega_2^2 + \omega_3^2 - \omega^2)\Big) d\omega_1 d\omega_2 d\omega_3, \tag{2.40}$$

Next we employ the Zakharov transformations [101, 69], which are a set of conformal transformations one applies to the integrand that result in the reduction of the sum of delta functions to a single delta function. This new structure of the integrand will allow us to (a) explicitly see the zeros of the equation and (b) allow us to explicitly compute the Kolmogorov constant C. See [61] for an intuitive, geometric description of how these transformations achieve this effect assuming only a self-similar spectrum. We distribute the last sum of delta functions, and handle each term separately. The first term,

$$\frac{\partial \mathcal{N}_\omega}{\partial t}^{(1)} = 128\pi A^3 \int_0^\infty \int_0^\infty \int_0^\infty \omega_1^{\gamma+1}\omega_2^{\gamma+1}\omega_3^{\gamma+1}\omega^{\gamma+1} \left(\omega^{-\gamma} + \omega_3^{-\gamma} - \omega_1^{-\gamma} - \omega_2^{-\gamma}\right) \times \delta(\omega_1 + \omega_2 - \omega_3 - \omega)\delta(\omega_1^2 + \omega_2^2 + \omega_3^2 - \omega^2) d\omega_1 d\omega_2 d\omega_3, \tag{2.41}$$

is already of the form onto which we will map the other terms. Here, we have used a superscript

(1) to denote we are referring to the first term. Now, as an example, we manipulate the second term in full,

$$\frac{\partial \mathcal{N}_\omega}{\partial t}^{(2)} = 128\pi A^3 \int_0^\infty \int_0^\infty \int_0^\infty \omega_1^{\gamma+1}\omega_2^{\gamma+1}\omega_3^{\gamma+1}\omega^{\gamma+1}\left(\omega^{-\gamma}+\omega_3^{-\gamma}-\omega_1^{-\gamma}-\omega_2^{-\gamma}\right) \times\delta(\omega_1+\omega_2-\omega_3-\omega)\delta(\omega_1^2-\omega_2^2-\omega_3^2-\omega^2)d\omega_1 d\omega_2 d\omega_3, \tag{2.42}$$

to which we apply the following transformations: $\omega_1 = \omega^2/\omega_1'$, $\omega_2 = \omega\omega_2'/\omega_1'$, and $\omega_3 = \omega\omega_2'/\omega_1'$. Under these transformations, $d\omega_1 d\omega_2 d\omega_3 = \left(\frac{\omega}{\omega_1'}\right)^4 d\omega_1' d\omega_2' d\omega_3'$, and (2.42) becomes, after some reduction,

$$\frac{\partial \mathcal{N}_\omega}{\partial t}^{(2)} = 128\pi A^3 \int_0^\infty \int_0^\infty \int_0^\infty \left(\frac{\omega}{\omega_1'}\right)^{3\gamma+5} \omega_1'^{\gamma+1}\omega_2'^{\gamma+1}\omega_3'^{\gamma+1}\omega'^{\gamma+1}\left(\omega_1'^{-\gamma}+\omega_3'^{-\gamma}-\omega'^{-\gamma}-\omega_2'^{-\gamma}\right) \times\delta(\omega'+\omega_2'-\omega_3'-\omega_1')\delta(\omega_1'^2+\omega_2'^2+\omega_3'^2-\omega'^2)d\omega_1' d\omega_2' d\omega_3'. \tag{2.43}$$

We note that the identity $\int \delta(ax)dx = \int \delta(x)/|a|dx$ is used to simply the above expression. The integrand of (2.43) *almost* reflects (2.41) with an additional factor of $(\omega/\omega_1')^{3\gamma+5}$. If one carefully looks at the signed terms in the equation, however, it is apparent that certain indices have become switched as a result of our transformation. Thankfully, the choice of indices is arbitrary, so we renumber them according to $123 \rightarrow 132$. This leaves us with

$$\frac{\partial \mathcal{N}_\omega}{\partial t}^{(2)} = -128\pi A^3 \int_0^\infty \int_0^\infty \int_0^\infty \left(\frac{\omega}{\omega_1'}\right)^{3\gamma+5} \omega_1'^{\gamma+1}\omega_2'^{\gamma+1}\omega_3'^{\gamma+1}\omega'^{\gamma+1}\left(\omega'^{-\gamma}+\omega_3'^{-\gamma}-\omega_1'^{-\gamma}-\omega_2'^{-\gamma}\right) \times\delta(\omega_1'+\omega_2'-\omega_3'-\omega)\delta(\omega_1'^2+\omega_2'^2+\omega_3'^2-\omega'^2)d\omega_1' d\omega_2' d\omega_3'. \tag{2.44}$$

In this form, the symmetry with (2.41) is obvious. We perform the remaining Zakharov transformations (see [101] for the forms of the other transformations), sum the four terms, and drop the primes from our notation. This results in

$$\frac{\partial \mathcal{N}_\omega}{\partial t} = 128\pi A^3 \int_0^\infty \int_0^\infty \int_0^\infty \omega_1^{\gamma+1}\omega_2^{\gamma+1}\omega_3^{\gamma+1}\omega^{\gamma+1}\left(\omega^{-\gamma}+\omega_3^{-\gamma}-\omega_1^{-\gamma}-\omega_2^{-\gamma}\right) \times\left(1+\left(\frac{\omega_3}{\omega}\right)^y-\left(\frac{\omega_1}{\omega}\right)^y-\left(\frac{\omega_2}{\omega}\right)^y\right)\delta(\omega_1+\omega_2-\omega_3-\omega)\delta(\omega_1^2+\omega_2^2+\omega_3^2-\omega^2)d\omega_1 d\omega_2 d\omega_3, \tag{2.45}$$

with $y \equiv -3\gamma - 5$. Careful consideration of the quartet and resonance conditions that remain in the delta functions reveals that (2.45) is an integral over the intersection of the plane $\omega_1+\omega_2-\omega_3-\omega = 0$ and the sphere $\omega_1^2 + \omega_2^2 + \omega_3^2 = \omega^2$ for any given ω. Thus, we do not need to consider integrating over any $\omega_i > \omega$. This enables a reparameterization in terms of some $\xi_i = \omega_i/\omega \in [0, 1]$, so that (2.45) becomes

$$\frac{\partial \mathcal{N}_\omega}{\partial t} = 128\pi A^3 \omega^{-y-1} I(y) = 128\pi A^3 \omega^{-y-1} \int_0^1 \int_0^1 \int_0^1 (\xi_1\xi_2\xi_3)^{\gamma+1} \left(1 + \xi_3^{-\gamma} - \xi_1^{-\gamma} - \xi_2^{-\gamma}\right) \times(1 + \xi_3^y - \xi_1^y - \xi_2^y)\delta(\xi_1 + \xi_2 - \xi_3 - 1)\delta(\xi_1^2 + \xi_2^2 + \xi_3^2 - 1)d\xi_1 d\xi_2 d\xi_3. \tag{2.46}$$

This is the form of the WKE that yields the possible γ corresponding to stationary solutions. First, however, one must show that the collision integral converges in the neighborhood of all γ for which the collision integral is stationary (obtaining these γ will be discussed next). We refer the reader to [100] for details and proof of stationary locality for this system.

One can see by the second product in the integrand that if $\gamma = 0$, the RHS of (2.46) is identically 0. This corresponds to equipartition of wave action, i.e., n_ω is constant. Also, if $\gamma = -1$, then the second product is identically 0 whenever the resonance condition is satisfied, also leading to a 0 of the collision integral. This solution $n_\omega = A/\omega$ corresponds to the Rayleigh-Jeans spectrum. As discussed in the introduction, neither of these solutions correspond to wave turbulence, but rather are equilibrium solutions. The KZ solutions are given by $y = 0$ and $y = 1$, which produce 0's of the collision integral by the same arguments as the equilibrium solutions. Setting $y = 0$, one obtains $n_\omega = A\omega^{-5/3}$, and for $y = 1$, one obtains $n_\omega = A\omega^{-2}$. To determine which of these out-of-equilibrium spectra correspond to the forward cascade of energy (with exponent γ_0) and which corresponds to the inverse cascade of wave action (γ_1), one may use Fjørtoft's argument [69] or Zakharov's method via evaluating (2.46) [100], while in both cases being careful to ensure the flux directions are not non-physical via comparison to the equilibrium spectra [101, 69, 100]. In [100], it is shown that the forward and inverse cascade for our system has stationary locality and physical cascade directions, and that $y = 1$ corresponds to the forward cascade.

Next, we derive the Kolmogorov constant C_0 and flux scaling parameter θ_0 associated with the forward cascade. The energy flux through frequency ω is defined by a control volume argument in spectral space (see Section 2.5) as

$$P(\omega) \equiv -\int_0^\infty \omega' \frac{\partial \mathcal{N}}{\partial t}(\omega')d\omega' = -128\pi A^3 \frac{\omega^{1-y}}{1-y} I(y), \tag{2.47}$$

where an negative sign is introduced to ensure that a positive flux corresponds to a cascade of energy

from large to small scales (long to short time scales via the dispersion relation). For the forward cascade with $y = 1$, the computation of $P(\omega)$ involves the limit of an indeterminate quantity, which can be obtained via L'Hospital's rule to be

$$P(\omega) = 128\pi A^3 \lim_{y\to 1} \frac{dI(y)}{dy}. \tag{2.48}$$

The limit of the desired derivative, S, is given by

$$\begin{aligned} S = \lim_{y\to 1} \frac{dI(y)}{dy} = \int_0^1 \int_0^1 \int_0^1 (\xi_1\xi_2\xi_3)^{-1} \left(1 + \xi_3^2 - \xi_1^2 - \xi_2^2\right) \\ \times(\xi_3 \ln \xi_3 - \xi_1 \ln \xi_1 - \xi_2 \ln \xi_2)\delta(\xi_1 + \xi_2 - \xi_3 - 1)\delta(\xi_1^2 + \xi_2^2 + \xi_3^2 - 1)d\xi_1 d\xi_2 d\xi_3, \end{aligned} \tag{2.49}$$

where we have used the fact that $\lim_{y\to 1} \frac{dx^y}{dy} = x \ln x$. In Appendix A, we develop a precise method to numerically evaluate (2.49) to find $S = 0.09353$. We now compute the relationship between A and $P(\omega)$, revealing both the KZ flux scaling θ_0 and Kolmogorov constant C_0 via

$$A = C_0 P^{\theta_0} = (128\pi S)^{-1/3} P^{1/3}, \tag{2.50}$$

resulting in $C_0 = 0.2984$ and $\theta_0 = 1/3$. Given that C_0 is positive, we can now be sure that the cascade direction is correct. Thus, the KZ spectrum associated with the forward cascade process in the $(\alpha = 1/2, \beta = 0)$ MMT model is given by $n_\omega = 0.2984 P^{1/3}\omega^{-2}$, or, via the linear dispersion relation, $n_k = 0.2984 P^{1/3} k^{-1}$. We note that this value of C_0 is different from the result of Zakharov et al. [100], due to their missing factor of 2 in the spectral element relation $\mathcal{N}(\omega)d\omega = 2n(k)dk$.

We conclude this section by providing the forward cascade KZ spectra $n_k = C_0 P^{\theta_0} k^{\gamma_0}$ for the other MMT systems studied in this work. A general derivation of γ_0 and θ_0 is possible, which resembles the analysis provided here (see [69]). The result is that, for a 4-wave system, $\theta_0 = 1/3$, and γ_0 is determined by the system parameters. For the MMT model, this reduces to $\gamma_0 = -d - 2\beta/3$. We will not require the Kolmogorov constant for these other MMT systems.

2.5 Numerically Exact Evaluations of KZ Quantities

Next, we will shift our focus to discuss how quantities such as γ, C, P, and the flux scaling θ can be computed for numerical data. In this work, C, θ, and γ (without subscripts) will often refer to quantities that are measured, where as the C_0, γ_0, and θ_0 will always refer to the KZ spectrum for a given system. Given these numerical considerations, we return our focus to (2.1) evaluated with periodic boundary conditions. The first of these quantities, γ, can be computed directly from

a numerically obtained spectrum via a least-squares approach. In order to compute θ, one must compare the numerically obtained wave action spectra to numerically computed P for a range of these values. The calculation of P, however, is a rich topic, with several possible approaches. Before detailed discussion on how these quantities are computed, however, we must define how we obtain averaged quantities.

The numerical method described by (2.15) returns $\hat{\psi}_{\boldsymbol{k}}(t)$ on some interval $t \in [t_1, t_2]$. Because this dissertation is interested in almost exclusively steady (or quasi-steady) field statistics, such as wave action and mean energy flux, it is sufficient to replace the ensemble averages in section 2.3 with *time* averages, assuming ergodic dynamics. For statistically stationary processes (i.e., fully developed forced-dissipated turbulence), one can choose the time window $T_w \equiv t_2 - t_1$ to be orders of magnitude greater than the kinetic time scale. For decaying turbulence, one must carefully choose T_w to average out the $O(\varepsilon)$ dynamics, while preserving information on the $O(\varepsilon^2)$ dynamics. In both cases, we will for the rest of this dissertation denote time averaging with an overbar, and define wave action for numerical data to be

$$n_{\boldsymbol{k}} \equiv \frac{1}{T_w} \int_{t1}^{t2} |\hat{\psi}_{\boldsymbol{k}}|^2 dt = \overline{|\hat{\psi}_{\boldsymbol{k}}|^2}. \tag{2.51}$$

The numerically-obtained wave action spectrum can be angle-averaged easily, and will be denoted as n_k. In one dimension, angle-averaging numerical data is equivalent to summing over the positive and negative wave number components, then dividing by 2. Then, we identify the power-law inertial range interval $k \in IR$, and then fit a model $n_k = Ak^\gamma$ over this interval of k in a least squares sense, directly obtaining γ. If we assume $\theta = \theta_0 = 1/3$, then, after computing the mean flux $\overline{P}$, one can obtain $C = A/\overline{P}^{1/3}$. If several wave action spectra are obtained corresponding to different $\overline{P}$, is also possible to obtain a numerical θ. In this dissertation, this is done simply by evaluating the total inertial-range wave action $N = \sum_{k \in IR} n_{\boldsymbol{k}}$, and fitting a model $N = B\overline{P}^\theta$ to this data over the measured range of $\overline{P}$.

We are left now only with the issue of computing $\overline{P}$ from numerical data. First, we will point out that the WKE, taken in the $\varepsilon \to 0$ limit, describes the flux of H_2, as $H_4 \to 0$ in this limit. Thus, the first term in (2.16) provides an expression for the linear energy spectrum. A common way to compute mean inter-scale energy flux is to look at the total energy budget of the system. If a spectrum is decaying under small-scale dissipation, the mean inter-scale flux can be estimated the time rate of change of energy of the system, or by $\overline{P}_d$, the dissipation rate associated with the high-wave number dissipation term in (2.14). This latter approach also works for a stationary system with large-scale forcing and large-scale dissipation. The average high wave number dissipation rate can be computed by considering the mean time rate of change of $H_2(t)$ due to the dissipation

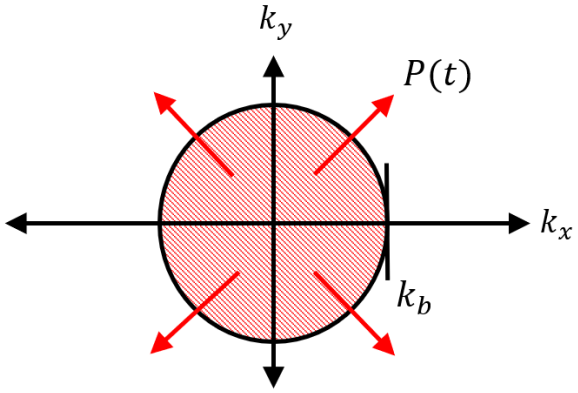

Figure 2.1: The control volume of radius k_b that defines the instantaneous outward (i.e., from large to small scale) energy flux $P(t)$ on a 2D domain.

$\frac{dn_{\boldsymbol{k}}}{dt} = 2\nu_{\boldsymbol{k}} n_{\boldsymbol{k}}$,

$$\overline{P} = \overline{P}_d = \sum_{k>k_d} -2\nu_{\boldsymbol{k}}\omega_{\boldsymbol{k}} n_{\boldsymbol{k}}, \tag{2.52}$$

where a negative sign is introduced so that a positive $\overline{P}_d$ corresponds to flux of energy from large to small scales, in accordance with WTT. For (2.52) to capture only the high wave number contributions to dissipation rate, one must ensure that k_d is chosen to be high enough to exclude the low wave number dissipation, which also is captured by the $\nu_{\boldsymbol{k}}$ term, assuming either broad scale dissipation, or that low wave number dissipation is included.

While (2.52) is an effective way to compute the mean energy flux, there exists a more direct and dynamically insightful method for computing $\overline{P}$. Rather than looking to dissipation rate, we instead draw a (circular) control volume in spectral domain, as depicted for a 2D wave number domain in Figure 2.1. This circle is of radius k_b, and the instantaneous energy flux through k_b is given by the time rate of change of H_2 in this control volume computed directly from the nonlinear term of (2.11). This formulation has the advantage of allowing the full (time) distribution of $P(t)$ to be resolved, in addition to the mean flux $\overline{P}$. A formula for $P(t)$ is given by

$$P(k_b,t) = -\sum_{k<k_b} \omega_{\boldsymbol{k}} \frac{d|\hat{\psi}_{\boldsymbol{k}}|^2}{dt}(t) = -\sum_{k<k_b} \omega_{\boldsymbol{k}} \left(\frac{d\hat{\psi}_{\boldsymbol{k}}}{dt}\hat{\psi}^*_{\boldsymbol{k}} + \hat{\psi}_{\boldsymbol{k}} \frac{d\hat{\psi}^*_{\boldsymbol{k}}}{dt} \right)(t), \tag{2.53}$$

where the derivatives in the rightmost expression can be efficiently evaluated via the pseudo-spectral method (2.13) given only the numerical solution $\hat{\psi}_{\boldsymbol{k}}(t)$. An almost identical method to that of evaluating $P(k_b,t)$ can be developed for the flux of the nonlinear energy H_4 (with a flux P_4). This allows for the measurement of the true "energy" flux, $P(k_b,t) + P_4(k_b,t)$, which is "valid"

even when the nonlinearity is large. More on this will be presented in Chapter 5. Note that the above expression also highlights the intimate connection between mean energy flux $\overline{P}$ and the wave kinetic description: the average of the second term in (2.53) is precisely the wave action evolution that the kinetic equation seeks to describe. Thus, energy flux is a natural quantity by which to study the WT closure, which brings us to our next topic.

2.6 An Interaction-based Flux Decomposition

In addition to the numerically efficient formulation of $P(t)$ just presented, there is a second useful formulation of the instantaneous energy flux. To understand its usefulness, however, we require a slight diversion. Very much along the lines of the action-angle formulation of the MMT model (2.19), there exists an exact expression for the evolution of wave action spectrum (i.e., the ensemble average of (2.19) without the assumption of a small parameter). In this case, the ensemble average is interpreted in the traditional sense, as the 1st moment of the probability distribution associated with a given observable under the Hamiltonian flow (2.5). Indeed, for wave action expressed as $n_{\boldsymbol{k}} = \langle |\hat{\psi}_{\boldsymbol{k}}|^2 \rangle$, one apply the product rule to $\frac{d|\hat{\psi}_{\boldsymbol{k}}|^2}{dt}$, simplify, and average to obtain

$$\frac{dn_{\boldsymbol{k}}}{dt} = 2\lambda \sum_{\boldsymbol{k}_1 \in \Lambda_L^2} \sum_{\boldsymbol{k}_2 \in \Lambda_L^2} \sum_{\boldsymbol{k}_3 \in \Lambda_L^2} (k_1 k_2 k_3 k)^{\beta/4} \mathrm{Im} \langle \hat{\psi}_{\boldsymbol{1}} \hat{\psi}_{\boldsymbol{2}} \hat{\psi}^*_{\boldsymbol{3}} \hat{\psi}^*_{\boldsymbol{k}} \rangle \delta_K(\boldsymbol{k}_1 + \boldsymbol{k}_2 - \boldsymbol{k}_3 - \boldsymbol{k}). \tag{2.54}$$

As promised in the introduction, the evolution of wave action, a second order field statistic, explicitly depends on the evolution of 4th order statistics. In fact, the evolution of wave action spectrum is expressed here as sum the high-order statistics associated with all valid quartets in the domain. The evolution of these statistics depend themselves on higher order statistics: by taking the time derivative of the 4th order statistics on the RHS of the above equation, and applying the product rule, one can easily show that each 4th order statistic evolves according to a sum of 6th order statistics.

The procedure detailed in Section 2.3 produces a closure to (2.54) when the kinetic limit is taken. We are inspired to devise an evaluation of energy flux that uses this interaction form of spectral evolution to provide a dynamical compliment to the kinematic description of finite-size effects, allowing for a more rich understanding of wave turbulence on bounded domains and the realization of the WT closure.

2.6.1 Frequency Mismatch Filtering

By introducing an additional Kronecker delta function that resembles the quasi-resonance condition (1.5), we are enabled to extract from (2.54) the spectral evolution of mode $\boldsymbol{k}$ due to interactions of

a certain frequency mismatch Ω. We define

$$\left.\frac{dn_{\boldsymbol{k}}}{dt}\right|_{\Omega} \equiv 2\lambda \sum_{\boldsymbol{k}_1\in\Lambda_L^2} \sum_{\boldsymbol{k}_2\in\Lambda_L^2} \sum_{\boldsymbol{k}_3\in\Lambda_L^2} (k_1k_2k_3k)^{\beta/4} \mathrm{Im}\left(\overline{\hat{\psi}_{\boldsymbol{1}}\hat{\psi}_{\boldsymbol{2}}\hat{\psi}^*_{\boldsymbol{3}}\hat{\psi}^*_{\boldsymbol{k}}}\right) \times\delta_K(\boldsymbol{k}_1+\boldsymbol{k}_2-\boldsymbol{k}_3-\boldsymbol{k})\delta_K(|\omega_{\boldsymbol{1}}+\omega_{\boldsymbol{2}}-\omega_{\boldsymbol{3}}-\omega_{\boldsymbol{k}}|-\Omega). \tag{2.55}$$

Explicitly, $\left.\frac{dn_{\boldsymbol{k}}}{dt}\right|_{\Omega}$ represents the contribution of all interactions with a frequency mismatch Ω to spectral evolution. Here, it becomes important to specify the domain dimension d and the dispersion relation power α. For the majority of this dissertation, $d = 2$ and $\alpha = 2$. Under these conditions, for a domain of size $2\pi \times 2\pi$, Ω takes exclusively even integer values for every quartet described by the wave number condition (1.3). Because we are interested in truncated (numerical) Fourier domains, there also exists a maximum value of Ω. Thus, we can sum over all Ω to recover

$$\frac{dn_{\boldsymbol{k}}}{dt} = \sum_{\Omega=0}^{\Omega_{\max}} \left.\frac{dn_{\boldsymbol{k}}}{dt}\right|_{\Omega}. \tag{2.56}$$

Hence, we refer to this filtering process as an interaction based decomposition.

We use this interaction-based decomposition of spectral evolution to define a interaction-based flux decomposition. We define

$$\overline{P}_{\Omega}(k_b) = -\sum_{k<k_b} \omega_{\boldsymbol{k}} \left.\frac{dn_{\boldsymbol{k}}}{dt}\right|_{\Omega}, \tag{2.57}$$

where $\overline{P}_{\Omega}(k_b)$ also enjoys the decomposition property (2.56). In the case of $d = 1$ and $\alpha = 1/2$, as in Chapter 5, quartets in the domain take a much larger variety of values, with $\Omega \notin \mathbb{Z}$ generally. To ensure the property (2.56), we instead use a finite-width Kronecker delta function, whose width is equal to a chosen resolution of Ω. We can additionally compute the full time distribution of each flux contribution via

$$P_{\Omega}(k_b, t) = -\sum_{k<k_b} \omega_{\boldsymbol{k}} \left.\frac{d|\hat{\psi}_{\boldsymbol{k}}|^2}{dt}\right|_{\Omega}(t), \tag{2.58}$$

where $\left.\frac{d|\hat{\psi}_{\boldsymbol{k}}|^2}{dt}\right|_{\Omega}(t)$ can be obtained from the unaveraged form of (2.55).

The advantage of this interaction-based approach is that we can assess the role of nonlinear broadening, quasi-resonance, and exact resonance in determining spectral evolution of wave turbulence on a finite domain. This approach is much more direct than measurements of the $k-\omega$ spectrum or of coherence, as it related directly to the nonlinear dynamics of interest without further assumptions. Therefore, these measurements of the dynamics will provide a clear look as to the validity of the kinematic model for understanding DWT and KWT. In fact, they also allow for a

precise measurement of the WT closure.

2.6.2 Method for the study of the WT Closure

We will interpret the WT closure on a finite domain. Inspired by (2.31), we assume some unspecified closure function $f(\Omega)$, and write an expression for the summand of (2.55). This leads us to an expression for the fourth-order statistic,

$$\lambda \mathrm{Im}\left(\overline{\hat{\psi}_{\mathbf{1}}\hat{\psi}_{\mathbf{2}}\hat{\psi}^*_{\mathbf{3}}\hat{\psi}^*_{\boldsymbol{k}}}\right) = 2(k_1k_2k_3k)^{\beta/4} n_{\mathbf{1}}n_{\mathbf{2}}n_{\mathbf{3}}n_{\boldsymbol{k}} \left(\frac{1}{n_{\boldsymbol{k}}} + \frac{1}{n_{\mathbf{3}}} - \frac{1}{n_{\mathbf{1}}} - \frac{1}{n_{\mathbf{2}}}\right) f(\Omega) \tag{2.59}$$

Provided the RHS up to the function f is nonzero, we can then use our DNS of the MMT model to measure the closure for an individual quartet via

$$f_Q(\Omega) \equiv \frac{\lambda \mathrm{Im}\left(\overline{\hat{\psi}_{\mathbf{1}}\hat{\psi}_{\mathbf{2}}\hat{\psi}^*_{\mathbf{3}}\hat{\psi}^*_{\boldsymbol{k}}}\right)}{2(k_1k_2k_3k)^{\beta/4} n_{\mathbf{1}}n_{\mathbf{2}}n_{\mathbf{3}}n_{\boldsymbol{k}} \left(\frac{1}{n_{\boldsymbol{k}}} + \frac{1}{n_{\mathbf{3}}} - \frac{1}{n_{\mathbf{1}}} - \frac{1}{n_{\mathbf{2}}}\right)} \tag{2.60}$$

According to (2.31), $f_Q(\Omega)$ should take the form of a generalized delta function that only depends on Ω and some additional parameter that determines its width. In the kinetic limit, we expect $f_Q(\Omega)$ to collapse to a true delta function. Because $f(\Omega)$ has no explicit dependence on wave number (only the frequency mismatch), we can assume that *same* closure function should apply to every quartet in the domain. If this assumption is correct, then we can also measure $f_P(\Omega)$, which is determined not from a single quartet interaction, but rather all interaction contributing to the energy cascade through wave number k_b for some frequency mismatch Ω. If the assumption is incorrect, than $f_P(\Omega)$ represents the closure function averaged over all interactions that contribute to $\overline{P}$. This naturally takes the form

$$f_P(\Omega) \equiv \frac{2\lambda \sum_{k<k_b} \omega_{\boldsymbol{k}} \sum_{\boldsymbol{k}_1\boldsymbol{k}_2\boldsymbol{k}_3} (k_1k_2k_3k)^{\beta/4} \mathrm{Im}\left(\overline{\hat{\psi}_{\mathbf{1}}\hat{\psi}_{\mathbf{2}}\hat{\psi}^*_{\mathbf{3}}\hat{\psi}^*_{\boldsymbol{k}}}\right) \delta_K(\Delta\boldsymbol{k}^{12}_{3k})\delta_K(\Omega)}{4 \sum_{k<k_b} \sum_{\boldsymbol{k}_1\boldsymbol{k}_2\boldsymbol{k}_3} (k_1k_2k_3k)^{\beta/2} n_{\mathbf{1}}n_{\mathbf{2}}n_{\mathbf{3}}n_{\boldsymbol{k}} \left(\frac{1}{n_{\boldsymbol{k}}} + \frac{1}{n_{\mathbf{3}}} - \frac{1}{n_{\mathbf{1}}} - \frac{1}{n_{\mathbf{2}}}\right) \delta_K(\Delta\boldsymbol{k}^{12}_{3k})\delta_K(\Omega)}. \tag{2.61}$$

Intermediate forms between (2.60) and (2.61) are also possible, where $f(\Omega)$ is determined from a simple sum over some number of quartets (in both the numerator and denominator). If the measured $f(\Omega)$ represents the true generalized delta function of the WT closure, then its integration (over only positive Ω) has

$$\int_0^\infty f(\Omega) d\Omega = \pi/2. \tag{2.62}$$

Therefore, $f(\Omega)$ allows for the quantitative study of the WT closure as realized in Direct Numerical Simulation (DNS) of a given wave equation evaluated on a finite domain.

CHAPTER 3

Wave Turbulence on Rational and Irrational Tori

In this chapter, we explore wave turbulence realized on two different 2D periodic domains (tori). The widely adopted kinematic picture of DWT outlined in Chapter 1 implies that deviation of bounded domain dynamics from WKE predictions depends only on the nonlinearity level and wave number discreteness. In the present work, we show that this traditional understanding overlooks a key property - the Discrete Resonant Manifold (DRM) that survives as nonlinear broadening Γ approaches zero, i.e., the discrete set of resonant quartets which satisfy (1.3) and (1.4) when $\boldsymbol{k}$ is restricted to a lattice. To illustrate this idea, we conduct controlled numerical simulations where the effect of wave number discreteness on the dynamics can be studied separately, i.e., isolated from the other factors such as broad-scale dissipation.

The MMT equation is simulated on both rational and irrational tori (periodic domains of rational and irrational aspect ratios), which correspond to different DRM structures. We show remarkably different power-law spectra on these two tori, with the rational-torus spectral slope approaching the WTT solution with decreasing nonlinearity, in contrast to the steepened spectrum on the irrational torus. The dynamical differences between the tori are interpreted through the different DRM structures, over which a summation of resonant interactions critically determines the energy cascade. It is found that the DRM approximates the continuous resonant manifold (CRM) of WTT (i.e., the continuous set satisfying (1.3) and (1.4) with $\Gamma = 0$) only on the rational torus. This can be tied to a recent number theoretic result [35], which rigorously equates the lattice sum over the DRM of the rational torus to the integration over the CRM with a constant factor difference. We conclude by outlining the implications of our findings to general physical wave contexts. This work was published in Physical Review E in 2020 [44], and the remainder of this chapter and Appendix B is adapted from the article.

3.1 Model Specification and Numerical Setup

The α-parameter in our MMT equation is tuned to yield a dispersion relation $\omega_{\boldsymbol{k}} = k^2$. This is the only dispersion relation for which a rigorous interpretation of our simulation results can be achieved, as we require the dispersion relation of the NLS. We choose $\beta = 4$, which corresponds to fast spectral evolution with nonlinear time scale decreasing with the increase of k [33].

The KZ spectrum for this system is given by $n_k = C_0 P^{1/3} k^{-14/3}$, so $\gamma_0 = -14/3$. In order to study the effect of DRM structure, we also consider (2.1) on rational and irrational tori $\mathbb{T}^2_r$ and $\mathbb{T}^2_{ir}$ of sizes $2\pi \times 2\pi/q$, with $q = 1$ for $\mathbb{T}^2_r$ and $q^2 = \sqrt{2}$ for $\mathbb{T}^2_{ir}$. The corresponding discrete wave numbers are taken from the sets $\mathbb{Z}^2_{r,ir} \equiv \mathbb{Z} \times q\mathbb{Z}$. While any irrational number q results in an irrational torus, the particular value $q^2 = \sqrt{2}$ eliminates the majority of resonant quartets that exist on $\mathbb{T}^2_r$ by restricting the orientation of quartets on the k-plane (see Appendix B for a detailed discussion).

We simulate (2.14) with 256×256 modes on both $\mathbb{T}^2_r$ and $\mathbb{T}^2_{ir}$. Multiple simulations of free-decay turbulence are conducted, starting from isotropic Gaussian spectra $n_{\boldsymbol{k}} = a_0 e^{-0.01(k-10)^2}$ with random phases and amplitude a_0 covering a broad range of nonlinearity levels. Since the integral of total linear energy corresponding to the KZ spectrum is convergent in the limit of $k \to \infty$, the (theoretical) forward cascade forms a finite-capacity spectrum [69] which is realizable in free-decay simulations even at very large wavenumbers. To model wave dissipation, we set $\nu_{\boldsymbol{k}} = \nu_0 k^8$ in (2.14). We remark that the k^8 dependence is sufficient to confine the dissipation at high wave numbers [61, 11], in contrast to some previous simulations [76] and experiments [65, 20]. The parameter ν_0 takes values $\nu_R \equiv [2.50 \times 10^{-17}, 2.50 \times 10^{-16}]$, for which clear power-law spectra can be observed at all nonlinearity levels of interest. We further consider an optimal value ν_{opt} (for each nonlinearity level on each torus) that corresponds to the smallest ν in ν_R without resulting in "bottleneck" energy accumulation at high wave numbers [34]. In the next section, we report results for ν_{opt} as well as uncertainty bars associated with ν_R.

3.2 Results

In this chapter, we define the nonlinearity level of a wave field as $\epsilon \equiv H_4/H$. In Figure 3.1, the angle-averaged initial and fully-developed spectra n_k at different values of ϵ obtained with ν_{opt} are plotted for $\mathbb{T}^2_r$ and $\mathbb{T}^2_{ir}$. We see that the fully-developed spectra exhibit power-law forms with inertial ranges of about 2/3~4/3 decades depending on ϵ on each torus. We evaluate the spectral slope γ over the the range of k for which an approximate power-law form appears the longest.

Figure 3.2 plots the spectral slope γ obtained with ν_{opt} as a function of ϵ (ranging two orders of magnitude) on both tori. We also include the uncertainty bars computed from the range ν_R, which demonstrates that ν_R only weakly impacts the values of γ (with an order of magnitude variation of

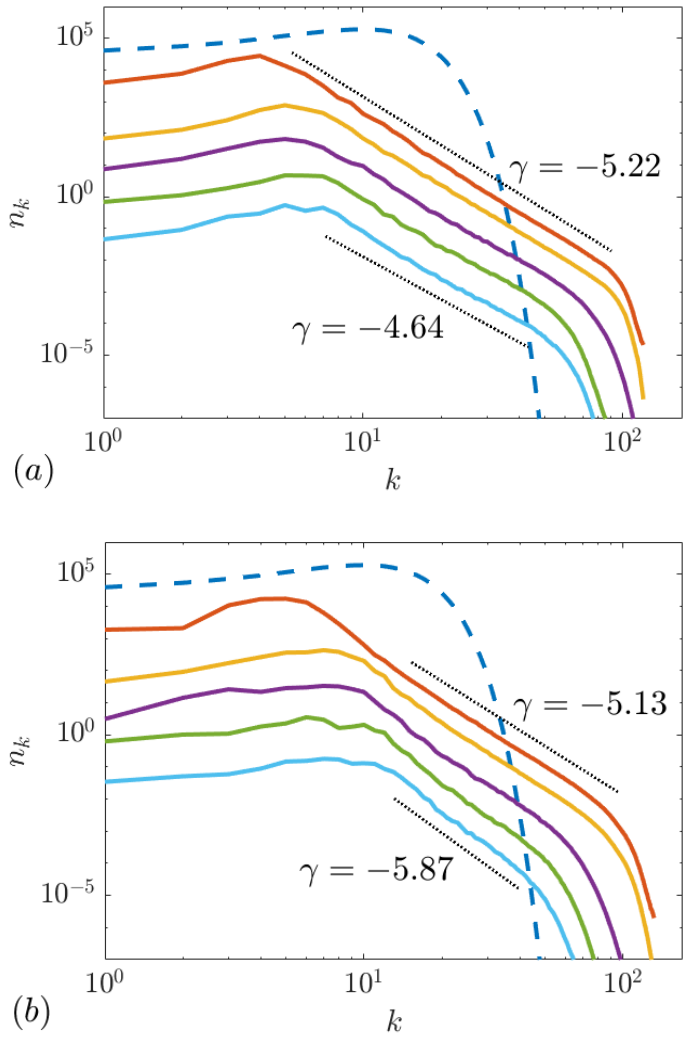

Figure 3.1: The initial spectra (– – –) and fully-developed power-law spectra n_k (——) calculated with ν_{opt} at different values of ϵ on (a) $\mathbb{T}^2_r$ and (b) $\mathbb{T}^2_{ir}$. The power-law spectra are shifted for clarity, representing ϵ=0.03, 0.01, 0.003, 0.001 and 0.0003 from top to bottom. The linear fit for the top and bottom spectra are indicated ($\cdot\ \cdot\ \cdot$).

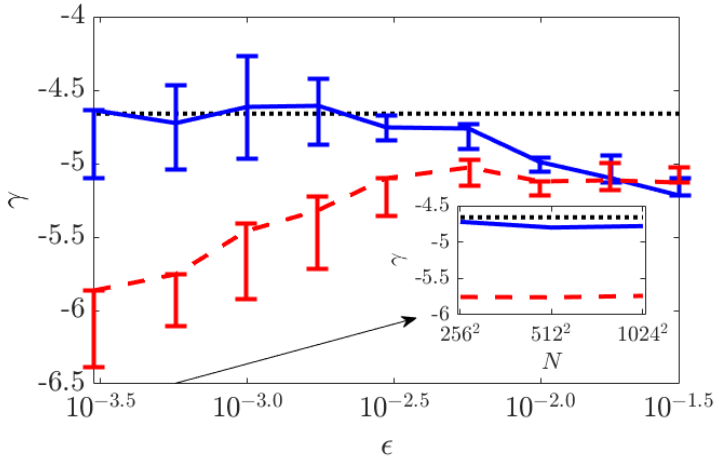

Figure 3.2: Spectral slope γ computed using ν_{opt} as a function of ϵ on $\mathbb{T}^2_r$ (——) and $\mathbb{T}^2_{ir}$ (– – –). The uncertainties associated with ν_R are shown by the vertical bars. The WTT analytical solution $\gamma_0 = -14/3$ is indicated ($\cdot\ \cdot\ \cdot$). (inset) Spectral slope γ computed with ν_{opt} at $\epsilon = 5.75 \times 10^{-4}$ as a function of number of modes N on $\mathbb{T}^2_r$ (——) and $\mathbb{T}^2_{ir}$ (– – –).

ν, the largest uncertainty in γ is $O(0.5)$). At high nonlinearity levels, the values of γ on both tori are almost identical, and about 0.5 smaller (i.e., steeper spectra) than the WTT value $\gamma_0 = -14/3$. With the decrease of nonlinearity, the spectral slope γ exhibits remarkably different behaviors on the two tori. On $\mathbb{T}^2_{ir}$, γ decreases with ϵ, indicating steepened spectra in agreement with previous observations in other wave systems [84, 78, 24, 42, 19]. However, on $\mathbb{T}^2_r$, γ approaches and remains at γ_0 with the decrease of ϵ, a trend unexplained by the traditional kinematic model. Convergence to the WTT spectral slope with the decrease of nonlinearity level, on the other hand, is also recently observed for a one-dimensional MMT equation [11] (whose resonant set may be considered as a subset of the 2D case without the depleting effect of q). To ensure the robustness of these results to varying grid resolutions, we select two cases at relatively low nonlinearity level on $\mathbb{T}^2_r$ and $\mathbb{T}^2_{ir}$, and check the spectral slope with increasing number of modes N in simulations. The results plotted in the inset of Figure 3.2 show that γ converges with the increase of N and that the results using 256^2 modes are sufficient to capture the physics of interest.

The behavior of γ cannot be interpreted by the bound wave mechanism as in some experiments [15, 63, 9], as analysed in detail from the k-ω spectrum in Appendix B. To understand the dominating mechanism, we further investigate the energy cascade on both tori. For this, we use the developments in section (2.5), in particular measurements of the mean flux via (2.53) and the contributions of strictly resonant interactions via (2.57) with $\Omega = 0$. Figure 3.3(a) shows the total mean flux $\overline{P}$ as a function of ϵ for both tori. The values of $\overline{P}$ on $\mathbb{T}^2_r$ are consistently larger than those on $\mathbb{T}^2_{ir}$, with a pronounced difference (about one decade) for small ϵ. This indicates that the energy cascade is far more efficient on $\mathbb{T}^2_r$, especially at low nonlinearity. We further plot

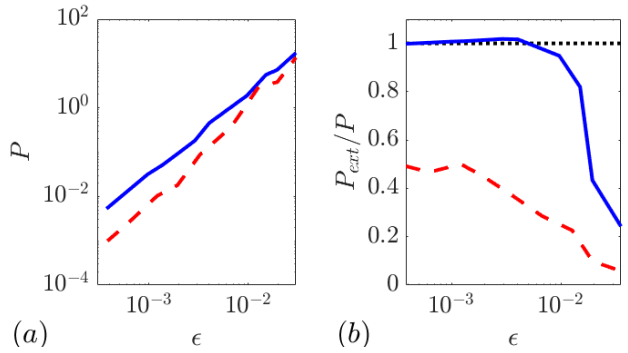

Figure 3.3: (a) $\overline{P}$ and (b) $\overline{P}_{\Omega=0}/\overline{P}$ as functions of ϵ on $\mathbb{T}^2_r$ (——) and $\mathbb{T}^2_{ir}$ (– – –). The line of $\overline{P}_{\Omega=0}/\overline{P}$ ($\cdot\ \cdot\ \cdot$) is indicated in (b).

$\overline{P}_{\Omega=0}/\overline{P}$ as a function of ϵ in Figure 3.3(b). With the decrease of ϵ, it is found that $\overline{P}_{\Omega=0}/\overline{P}$ on $\mathbb{T}^2_r$ quickly approaches unity, showing the dominance of exact resonance on the energy cascade at low nonlinearity. The regime of $\overline{P}_{\Omega=0}/\overline{P} \approx 1$ occurs consistently with $\gamma \approx \gamma_0$ for nonlinearity level $\epsilon \lesssim 0.005$ on $\mathbb{T}^2_r$. On the other hand, the ratio $\overline{P}_{\Omega=0}/\overline{P}$ on $\mathbb{T}^2_{ir}$ increases much slower, not exceeding 50% in the range of nonlinearities of interest. This analysis implies that the surviving exact resonances at low nonlinearity are critical in understanding the agreement between γ and γ_0 on $\mathbb{T}^2_r$, as well as the steepened spectrum on $\mathbb{T}^2_{ir}$.

3.3 Role of the DRM

In this section, we further investigate the structure of the resonant set $S_{\Omega=0}$, which becomes increasingly important to the dynamics with the decrease of nonlinearity level. We define $S_{\Omega=0}$ to be the set of all solutions to the wave number and resonance conditions (1.3) and (1.4). In particular, we will show that $\partial n_{\boldsymbol{k}}/\partial t|_{\Omega=0}$ defined by (2.55) is related to the WTT kinetic equation, which explains $\gamma = \gamma_0$ at low nonlinearity on $\mathbb{T}^2_r$.

To facilitate the description, we define the set $S_{\Omega=0} \cap \{\boldsymbol{k}, \boldsymbol{k}_1, \boldsymbol{k}_2, \boldsymbol{k}_3 \in \mathbb{T}^2_{r,ir}\}$ as the discrete resonant manifold (DRM) on $\mathbb{T}^2_r$ and $\mathbb{T}^2_{ir}$; and the set $S_{\Omega=0} \cap \{\boldsymbol{k}, \boldsymbol{k}_1, \boldsymbol{k}_2, \boldsymbol{k}_3 \in \mathbb{R}^2\}$ as the continuous resonant manifold (CRM) as in WTT. It has been rigorously proven by number theory [35] that for the dispersion relation $\omega = k^2$, the summation in (2.55) for $\Omega = 0$ (over the DRM) on $\mathbb{T}^2_r$ converges to an integral on the corresponding CRM with a factor difference in the limit of high wave numbers.

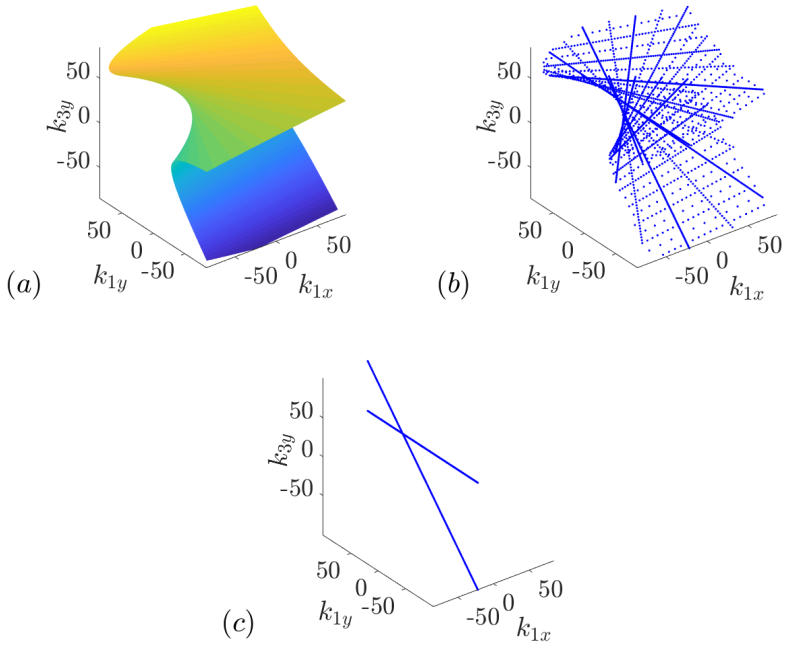

Figure 3.4: Visualizations of (a) the CRM, (b) the DRM on $\mathbb{T}^2_r$ and (c) the DRM on $\mathbb{T}^2_{ir}$ for $\boldsymbol{k}_2 = (-36, 31q)$ and $k_{3x} = -22$.

Built on the *continuous resonant* equation given in [35], we can derive (see Appendix B for details)

$$\begin{aligned} \left.\frac{\partial n_{\boldsymbol{k}}}{\partial t}\right|_{\Omega=0} \sim \int_{\boldsymbol{k}_1,\boldsymbol{k}_2,\boldsymbol{k}_3} & kk_1k_2k_3 \mathrm{Im}\langle \hat{\psi}_{\boldsymbol{1}}\hat{\psi}_{\boldsymbol{2}}\hat{\psi}^*_{\boldsymbol{3}}\hat{\psi}^*_{\boldsymbol{k}}\rangle \\ \times\delta(\boldsymbol{k}_1+\boldsymbol{k}_2-\boldsymbol{k}_3-\boldsymbol{k})\delta(\omega_{\boldsymbol{1}}+\omega_{\boldsymbol{1}}-\omega_{\boldsymbol{1}}-\omega_{\boldsymbol{k}})d\boldsymbol{k}_1 d\boldsymbol{k}_2 d\boldsymbol{k}_3, & \\ \text{for } \boldsymbol{k},\boldsymbol{k}_1,\boldsymbol{k}_2,\boldsymbol{k}_3 \in \mathbb{R}^2. & \end{aligned} \tag{3.1}$$

At low nonlinearity, $\partial n_{\boldsymbol{k}}/\partial t = \partial n_{\boldsymbol{k}}/\partial t|_{\Omega=0}$ on $\mathbb{T}^2_r$. We suggest that (3.1) can then be used to derive a system similar to the WKE (2.37), under quasi-Gaussian statistics which are valid at low nonlinearity. Under this argument, the spectral slope on $\mathbb{T}^2_r$ yields $\gamma = \gamma_0$ as in the stationary solution of (2.37). On the other hand, (3.1) is not satisfied for $\mathbb{T}^2_{ir}$, resulting in the steepened spectra at low nonlinearity level as previously explained in the kinematic model for DWT.

We further elaborate the structure of the DRMs on $\mathbb{T}^2_r$ and $\mathbb{T}^2_{ir}$ using a numerical visualization. To avoid viewing high-dimensional manifolds, we fix $\boldsymbol{k}_2 = (-36, 31q)$ and $k_{3x} = -22$, such that $S_{\Omega=0}$ is reduced to a two-dimensional structure embedded in a higher-dimensional space. Without loss of generality, we consider the higher-dimensional space to be $\{k_{1x}, k_{1y}, k_{3y}\}$, and plot the reduced CRM, and DRM on $\mathbb{T}^2_r$ and $\mathbb{T}^2_{ir}$ in Figure 3.4. While the DRM on $\mathbb{T}^2_r$ resembles the CRM, the DRM on $\mathbb{T}^2_{ir}$ is fundamentally different with a diminished number of resonant quartets. The

salient contrast in these DRM structures is the inherent reason for different DWT dynamics on $\mathbb{T}^2_r$ and $\mathbb{T}^2_{ir}$. Finally, we remark that both the density *and distribution* of resonances on the DRM affect the DWT dynamics. This is discussed in the contexts of other values of q in Appendix B, alongside a brief study on the effect of quasi-resonances under nonlinear broadening Γ.

3.4 Discussion

In general, the DRM structure relies on the physical wave properties and domain aspect ratio, with the former including dispersion relation and number of modes involved in each interaction. Therefore, different physical wave systems in different domains yield much richer DWT dynamics than that predicted by kinematic model of DWT, which does not have sensitivity to these factors. For example, capillary wave turbulence exhibits steepened spectra with the decrease of nonlinearity level on $\mathbb{T}^2_r$ [78], exactly opposite to MMT turbulence. This is due to the different DRM of capillary waves, which yields an empty set on $\mathbb{T}^2_r$ [49]. On the other hand, we speculate that it may be possible to use some irrational aspect ratio q to restore some exact resonances for capillary waves, which may provide a system where the spectral slope is less sensitive to the nonlinearity level. Experimentally, the effect of q can be observed by varying the aspect ratio of a wave tank as conducted in [42], although the effect of wall (instead of periodic) boundary conditions needs to be addressed. A more effective experimental setting is wave turbulence on a fluid torus [55] which provides naturally periodic boundary conditions. Further, given the wide applications of WTT, more investigations are warranted for understanding the DWT dynamics from the perspective of DRMs for different physical wave systems.

This chapter also establishes connections between pure mathematics and the physics of wave turbulence. The number theoretic properties of the DRM, in terms of its relation to CRM by (2.54) (for $\Omega = 0$) and (3.1), may allow for the development of the first quantitative model of energy flux in DWT (through a new DWT kinetic equation). To extend the DWT kinetic equation to other physical wave systems, number theoretic problems concerning DRMs associated with other dispersion relations must be resolved. The present work is also of interest to mathematicians in the field of harmonic analysis, in particular for the quantification of energy cascades on tori. Our finding of diminished energy flux for the MMT equation at low ϵ on $\mathbb{T}^2_{ir}$ is indeed consistent with recent rigorous analyses of the NLS [93, 46]. This is particularly well demonstrated in the numerical component to [46].

3.5 Summary

Through simulations of the 2D MMT equation (with dispersion relation $\omega = k^2$) on rational and irrational tori ($\mathbb{T}^2_r$ and $\mathbb{T}^2_{ir}$), we identify the critical effect of the structure of discrete resonant manifold (DRM) on DWT. On $\mathbb{T}^2_r$, the DRM structure resembles the continuous resonant manifold (CRM), with a lattice summation over the DRM converging to an integral over the CRM. The spectral slope thus approaches γ_0 for low nonlinearity as predicted by the WTT kinetic equation. On $\mathbb{T}^2_{ir}$, the DRM is altered by the diminished number of resonant quartets, leading to steepened spectrum and reduced energy cascade capacity with the decrease of nonlinearity.

CHAPTER 4

The Properties of Energy Flux in Wave Turbulence

In this chapter, we employ the precise methods for studying the energy cascade and WT closure developed in Section 2.5 to the study of stationary (forced-dissipated) WT in the 2D MMT model with $\alpha = 2$ and $\beta = 4$. These procedures are applied for fields of varying nonlinearity ε, allowing us to observe the DWT to KWT transition. In particular, we measure the full distribution of $P(t)$, as well statistics of the flux decomposition $P_\Omega(t)$. We use these flux measurements to obtain the flux scaling θ in both the DWT and KWT regimes, and relate this to the kinematic model of DWT/KWT. The decomposition technique also enables a study the WT closure as realized on a finite domain in the $\varepsilon \to 0$ limit, which we explore. This work was published in the Journal of Fluid Mechanics in 2022 [45], and the remainder of this chapter is adapted from the article.

4.1 Setup of Numerical Experiments

We compute the solution to (2.14) on a periodic domain of size $2\pi \times 2\pi$ containing 512×512 modes. Our purpose is to generate a long stationary state so that the distributions of P (and other quantities discussed in §2) are sufficiently resolved. Therefore, we force the system at large scales (in conjunction with small-scale dissipation) instead of considering free-decay turbulence. The dissipation parameter $\nu_{\boldsymbol{k}}$ in (2.14) is given by

$$\nu_{\boldsymbol{k}} = \begin{cases} 30k^{-4} & 0 < k \leq 7 \\ 6 \times 10^{-12}(k-100)^8 & k \geq 100 \\ 0 & \text{otherwise,} \end{cases} \tag{4.1}$$

Forcing and dissipation of this type have been demonstrated to produce results compatible with the WTT predictions in the one-dimensional MMT model [8].

We start the simulations from initial conditions $\hat{\psi}_{\boldsymbol{k}} = a_0 e^{-0.1|k-10|+\mathrm{i}\phi_{\boldsymbol{k}}}$, with $\phi_{\boldsymbol{k}}$ the uniformly-distributed, decorrelated random phases, and a_0 a real constant chosen to provide an energy close to that of the expected stationary state. To obtain the scaling θ over a range of $\overline{P}$, we run a collection of 19 simulations, differing only in forcing strength σ_F and initial spectral level a_0. These simulations cover a range of $\overline{P}$ spanning several orders of magnitude, with data collected in the stationary state for each case.

4.2 Results

Before presenting the results on energy flux, we first check the spectra at stationary states in simulations with different forcing magnitudes. Several typical one-dimensional angle-averaged spectra n_k at different levels are shown in Figure 4.1a, where we observe power-law ranges close to one decade for all spectra. Figure 4.1b shows the power-law exponent γ evaluated in all 19 simulations via a least-squares fit in $k \in [13, 60]$, as a function of the spectral level computed by an integral measure of the (conservatively taken) power-law range

$$N = \sum_{13<k<60} n_{\boldsymbol{k}}. \tag{4.2}$$

We note that N, as a measure of nonlinearity level, is monotonically related to the measure $\varepsilon = H_4/H_2$ in the range of N represented by our data, corresponding to $\varepsilon \in [0.002, 0.03]$ (a range where the linear part H_2 dominates the total Hamiltonian). This definition of ε is slightly different from the definition used in Chapter 3.

We see in Figure 4.1b that γ increases (i.e., the spectrum becomes shallower) with the decrease of N, reaching the WTT prediction $\gamma_0 = -14/3 = -4.67$ for low spectral levels (in particular, $\gamma_0 = -2s/3 - d$ with $d = 2$ the dimension and $s = 4$ the degree of homogeneity of the interaction kernel, as in [69]). This behavior of γ is consistent with our findings in Chapter 3. The deviation of γ from γ_0 at high nonlinearity may result from coherent structures, as suggested by [100] and [11] in the one-dimensional context, or some features of the 2D MMT model that are yet to be fully understood. For waves in different physical contexts, e.g., surface gravity waves [24, 102] and capillary waves [84, 78], the behaviors of γ are remarkably different.

We next present our full study of energy flux, with results organized into three sections. §4.2.1 discusses the distributions of P and its associated decomposition P_Ω. §4.2.2 focuses on the scaling of spectral level with P, with the results explained by the contributions of quasi/exact resonances to P. The study related to the closure model is then presented in §4.2.3.

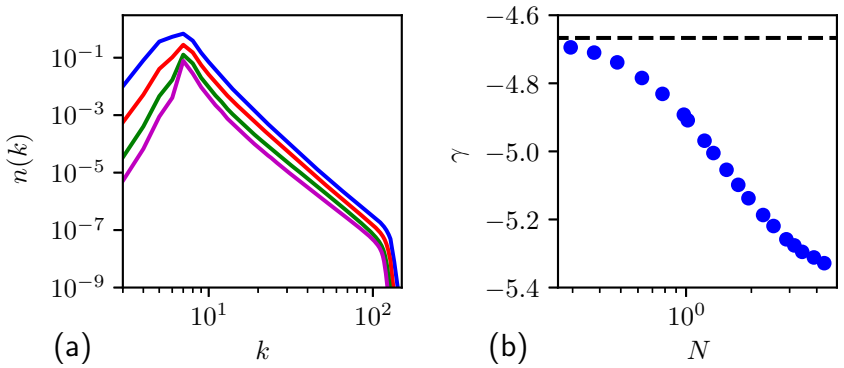

Figure 4.1: (a) A representative collection of fully-developed, angle-averaged wave action spectra $n(k)$. (b) Spectral slope γ as a function of N, with WTT value $\gamma_0 = -4.67$ indicated (- - - -).

4.2.1 Flux Distributions and Decomposition

A typical distribution of energy flux $P(t)$, computed with $k_b = 30$ from 2^{16} data points over a time window of $T_w = 256T_0$, is shown in Figure 4.2a (with $T_0 = 2\pi$ the fundamental period corresponding to the longest wave in the domain). We find that P closely follows a Gaussian distribution, with a standard deviation $\sigma(P) = 621.8$ several times larger than the mean value $\overline{P} = 77.02$. The very large standard deviation is consistent with previous studies in wave turbulence [32] and hydrodynamic turbulence [4]. However, the nearly perfect Gaussian form of the distribution has not been observed in these previous works, possibly because of differing turbulent systems and their different way of evaluating P. The reason for the Gaussianity of P is further explored in Chapter 5.

In addition, our method allows us to study the fully-resolved distribution of P at any scale (i.e., with arbitrary k_b). In Figures 4.2b and 4.2c, we plot the values of $\overline{P}$ and $\sigma(P)$ for k_b varying in the inertial range from 20 to 90. The mean flux $\overline{P}$ remains almost constant for all k_b, which is consistent with the WTT constant flux argument in the inertial range (this is only possible by avoiding broad-scale dissipation in simulations). The standard deviation $\sigma(P)$ increases with k_b, because more quartet interactions are included (as k becomes denser) resulting in more fluctuations in $P(t)$. We also include in Figures 4.2a and 4.2b the energy flux $\overline{P}$ computed from the high-wave-number dissipation rate (2.52) which agrees well with the majority values of $\overline{P}$, especially for larger k_b (to a relative difference within $O(1\%)$). Because of this, we will use $\overline{P}_d$ to represent the values of $\overline{P}$ for all 19 simulations in the subsequent analysis, since P_d yields a faster calculation due to an easier formulation and much smaller fluctuations (requiring less data points for averaging).

We next examine the relation between $\sigma(P)$ and nonlinearity level measured by $\overline{P}$, with $\sigma(P)$ as a function of $\overline{P}$ plotted in Figure 4.3. The result shows a power-law relation over two decades given by $\sigma(P) \sim \overline{P}^{0.8\pm0.05}$. Furthermore, we include in Figure 4.3 the standard deviation of the exact-resonant contributions to energy flux, $\sigma(P_{\Omega=0})$, with $P_{\Omega=0}$ calculated by the decomposition

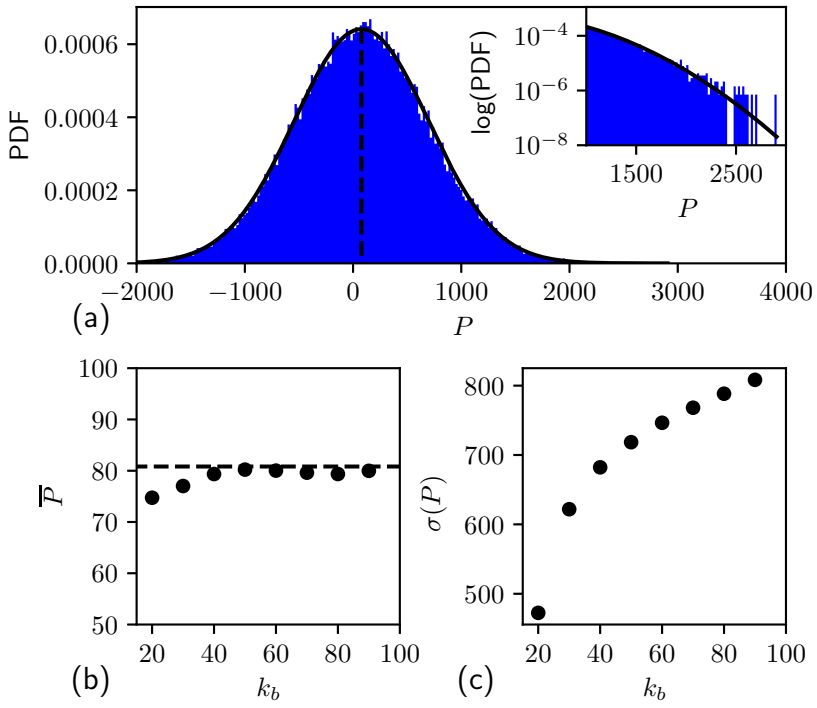

Figure 4.2: (a) The histogram of stationary time series $P(t)$ evaluated over $256T_0$, fitted with a Gaussian distribution of the same mean and standard deviation (——) for reference. Figure inset: tail of the distribution in logarithmic scale. (b) the mean $\overline{P}$ and (c) standard deviation $\sigma(P)$ evaluated for different k_b. The dissipation-based estimate of P_d is indicated in both (a) and (b) by (- - - -).

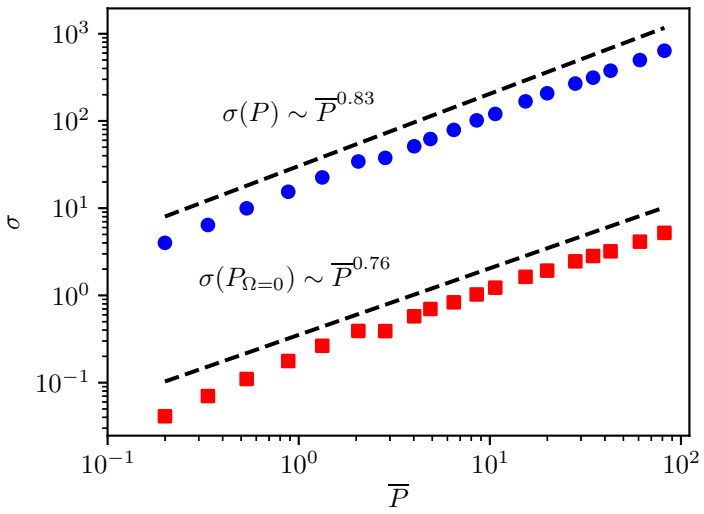

Figure 4.3: Dependence of $\sigma(P)$ (●) and $\sigma(P_{\Omega=0})$ (■) on $\overline{P}$, with the best fits indicated (- - - -).

method presented in §2. We observe a similar power-law relation between $\sigma(P_{\Omega=0})$ and $\sigma(P)$, but with the value of $\sigma(P_{\Omega=0})$ $O(10)$ times smaller than $\sigma(P)$ consistently for each nonlinearity level. This indicates that the large fluctuations in $P(t)$ are mainly generated due to quasi-resonant interactions.

A more detailed study about the contributions of exact and quasi resonances to $\overline{P}$ and $\sigma(P)$ can be conducted by looking into the components of P_Ω for varying values of Ω. In Figures 4.4a and 4.4b we plot $\overline{P}_\Omega$ and $\sigma(P_\Omega)$ for $\Omega \in [0, 30]$ at four different levels of nonlinearity. We note that Ω can only take even integer values for the dispersion relation $\omega_k = k^2$ on a periodic domain of $2\pi \times 2\pi$. The general trends in Figure 4.4a and 4.4b show that $\overline{P}_\Omega$ decreases, but $\sigma(P_\Omega)$ increases with the increase of Ω. This corresponds to a physical picture that as the interactions become more "quasi" (i.e., frequency mismatch Ω becomes larger), they contribute less to the mean flux but may contribute more to the fluctuations of the flux. We also emphasize here that while we always have $\sum_\Omega \overline{P}_\Omega = \overline{P}$, the quantity $\sum_\Omega \sigma^2(P_\Omega)$ is in general not equal to $\sigma^2(P)$ because $P_\Omega(t)$ with different Ω are not independent. Nevertheless, Figure 4.4b in conjunction with Figure 4.3 are sufficient to support the dominance of quasi-resonances in generating the large fluctuations in $P(t)$.

We conclude this section by summarizing two additional important results regarding P_Ω. First, the decomposition in terms of Ω enables a direct measure of nonlinear broadening by quantitatively considering the contribution of quasi-resonances to the total energy flux. To demonstrate this, we define a measure of nonlinear broadening $\Gamma \equiv \min\{\Omega | \overline{P}_\Omega < \alpha \overline{P}_{\Omega=0}\}$, which is plotted in 4.4c for $\alpha = 0.1$. While this choice of α can be varied, Γ clearly quantifies the nonlinear broadening by measuring the width of $\overline{P}_\Omega$ in Ω, showing that nonlinear broadening increases with $\overline{P}$. Second, the fluctuations seen in Figure 4.4a and 4.4b can be removed by considering the normalized flux $Q_\Omega(t) = P_\Omega(t)/\mathcal{N}_\Omega$. With $\mathcal{N}_\Omega$ (Figure 4.4d) counting the number of elements in $\sum_{\boldsymbol{k} \in \{\boldsymbol{k} | k < k_b\}} S_{\Omega, \boldsymbol{k}}$, $Q_\Omega(t)$ calculates the quartet-averaged flux (over quartets with frequency mismatch Ω), with both $\overline{Q}_\Omega$ and $\sigma(Q_\Omega)$ behaving smoothly for the range of Ω as shown in Figure 4.4e and 4.4f.

4.2.2 Scaling of Spectral Level with Flux

To understand the scaling of spectral level with energy flux, we plot in Figure 4.5 the spectral level N (see (4.2)) as a function of both $\overline{P}$ and $\overline{P}_{\Omega=0}$ representing total and exact-resonant flux respectively. Two salient scalings are observed over the 3 decades of energy flux. At high nonlinearity level with $\overline{P} \in [30, 100]$, we find a scaling approaching $N \sim \overline{P}^{1/3}$ (i.e., $\theta = 1/3$ with θ the scaling exponent defined in §2) consistent with the kinetic scaling of WTT. At low nonlinearity level with $\overline{P} \in [0.3, 3]$, the scaling behaves as $N \sim \overline{P}^{1/2}$ (i.e., $\theta = 1/2$) consistent with the dynamic scaling from (2.54). We next discuss the mechanisms underlying these two scalings.

For high nonlinearity, we see in Figure 4.5 that we have $\overline{P} \gg \overline{P}_{\Omega=0}$ consistent with observations

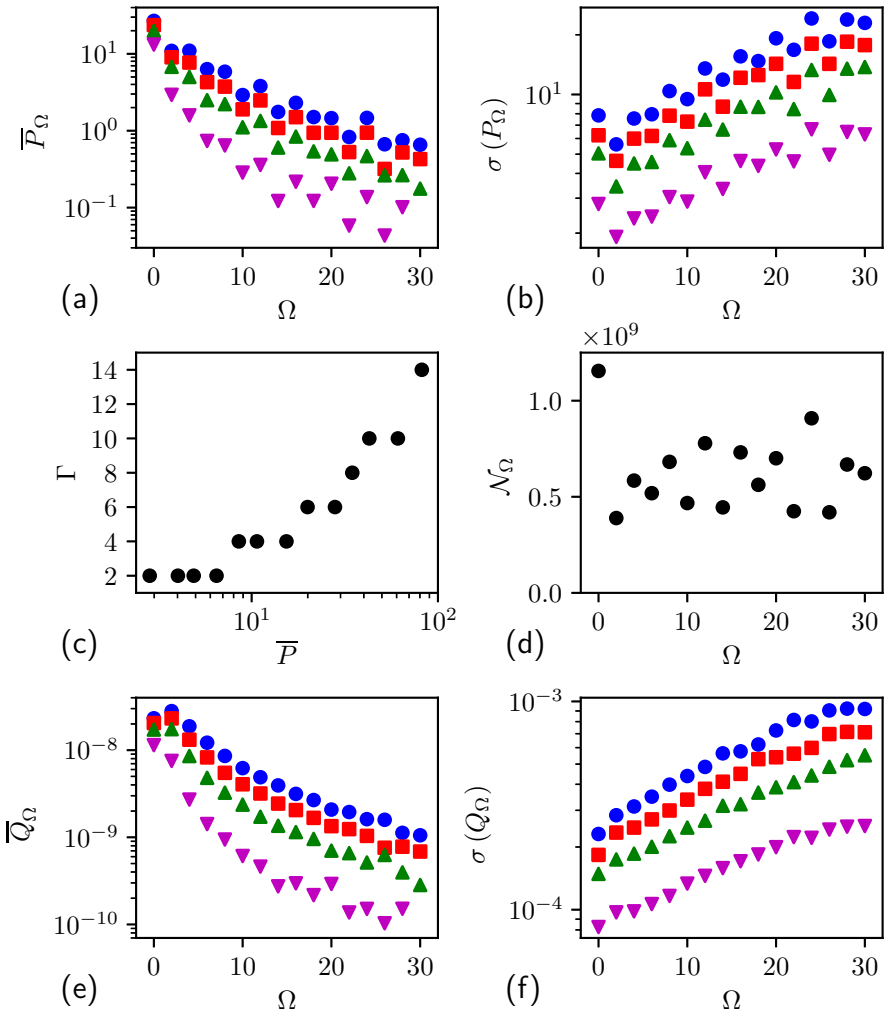

Figure 4.4: (a) $\overline{P}_\Omega$ and (b) $\sigma(P_\Omega)$ as functions of Ω, for four levels of nonlinearity with $\overline{P}$ = 81.9 (●), 61.0 (■), 42.8 (▲), and 20.0 (▼); (c) nonlinear broadening Γ as a function of $\overline{P}$; (d) number of quartet interactions $\mathcal{N}_\Omega$ for different Ω; (e) and (f) are similar to (a) and (b) but plotted for normalized flux Q_n. The computations to generate these results are conducted for k_b = 23 to reduce the computational cost associated with the number of involved quartets.

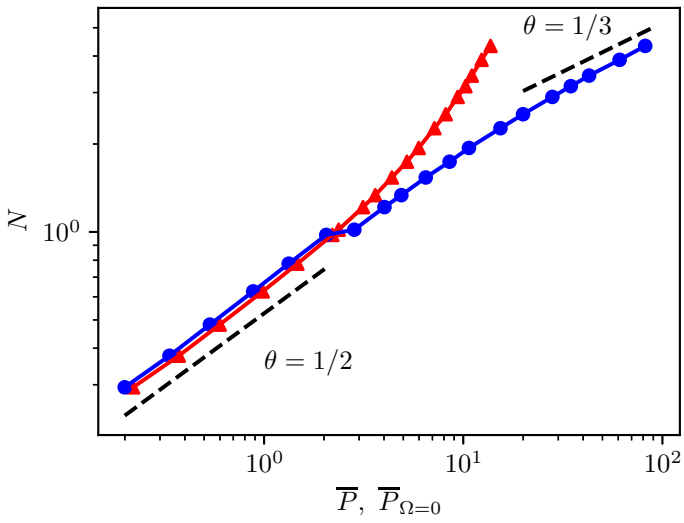

Figure 4.5: The scaling of inertial-range wave action N with $\overline{P}$ (—●—) and $\overline{P}_{\Omega=0}$ (—▲—). The dynamic scaling $\theta = 1/2$ and kinetic scaling $\theta = 1/3$ are indicated (- - - -).

in Figure 4.4a, indicating that quasi-resonances dominate the dynamics in this regime. This suggests that the kinetic scaling, developed from the WKE in the kinetic limit (infinite domain and small nonlinearity), is realized at relatively high nonlinearity in a finite domain as quasi-resonances overcome the discreteness. This physical picture is consistent with the results of [1, 60, 69, 80] which all suggest a kinetic wave turbulence regime dominated by quasi-resonance in a finite domain. In addition, recent mathematical justifications of the WKE [22, 23, 7] show that the kinetic limit should be taken according to particular scaling laws between the domain size and nonlinearity level, i.e., retaining the quasi-resonances as the large box limit is taken. More specifically, the quasi-resonances are the ones responsible for the emergence of the WKE in the large box limit [22]. However, it should be noted that these mathematical works only describe the initial evolution up to the kinetic time scale, and are not necessarily relevant to the stationary state we study here. In addition, the mathematical works are developed for the NLS ($\alpha = 2, \beta = 0$) and sometimes require a dimension $d \geq 3$ [22].

For low nonlinearity, $\overline{P} \approx \overline{P}_{\Omega=0}$ (as shown in Figure 4.5) due to the elimination of quasi-resonant contributions to $\overline{P}$, which has been previously observed in [44]. This is because the nonlinear broadening is not sufficient to overcome the discreteness of wavenumber in a finite domain. In this regime, kinetic wave turbulence is not supported (due to the lack of quasi-resonances) and the remaining exact resonances (on a discrete manifold) lead to a dynamic scaling that can be derived from (2.54). In addition, the dispersion relation $\omega_k = k^2$ is important for the realization of dynamic scaling because otherwise a frozen turbulence [84] behavior may be expected at low nonlinearity. For $\omega_k = k^2$, it has been proven (in the context of the NLS) that, for $N \to 0$, the dynamics at high

wavenumbers are described by a continuous resonant equation [35], i.e., the system behaves like a system of continuous wavenumber so that an energy cascade can be expected. In other words, the exact resonances on the discrete manifold determined by $\omega_k = k^2$ is sufficient to support an energy cascade.

In retrospect to Figure 4.1(b), we finally note that the kinetic scaling regime at high nonlinearity is associated with a spectral slope γ that is steeper than the WTT solution γ_0. This behavior is also observed in simulations of the MMT equation (in 1D with a different dispersion relation) by [11]. Further investigations on this problem (as well as the result of $\gamma = \gamma_0$ in the dynamic scaling range) are warranted. Here we simply remark that, in order for $\gamma = \gamma_0$ at high nonlinearity, one requires the solution of the WKE (i.e., the Kolmogorov-Zakharov spectrum) to be valid, which is a much stronger requirement than the kinetic scaling.

4.2.3 Investigation on the Closure Model

In this section, we use our numerical data to study the WTT closure model, in particular the magnitude and functional form of $f(\Omega)$. We perform this study for the nonlinearity levels associated with the kinetic scaling of $\overline{P}$, i.e., in the kinetic wave turbulence regime. The function $f(\Omega)$ in the WTT closure (as discussed in Chapter 2) is developed for this regime under a discrete setting before the large box limit is taken, and it is this form that we will study with our numerical data. Theoretically one expects $f(\Omega)$ to take the form of either a sinc-like function [47, 69] or $\epsilon/(\Omega^2+\epsilon^2)$ [101], with $\int_\Omega f(\Omega)d\Omega \sim O(1)$ since both forms are generalized delta functions. The numerical evaluation of $f(\Omega)$ will be performed at: (1) an individual quartet level using (2.60); (2) a family of quartets level using (2.60) in an average manner that will be introduced shortly; and (3) an inter-scale energy flux level using (2.61).

Figure 4.6 shows $f_Q(\Omega)$ evaluated for $O(50)$ quartets with $\Omega \in [0, 30]$, and with average quantities in (2.59) evaluated over a time window $T_w = 256T_0$. It is clear that no obvious functional pattern can be found for $f_Q(\Omega)$ (i.e., with different values of $f_Q(\Omega)$ obtained for the same Ω). This indicates that the WTT closure for fourth-order statistics cannot be used to describe the behavior of a single quartet (regardless of its associated frequency mismatch Ω) in the chosen finite time interval T_w. In other words, within T_w (which is long enough to resolve low-order statistics), the contributions of individual quartets to the energy cascade are not sufficiently resolved in our data to observe the WTT closure model. It is not clear from the current results whether there exist a sufficiently long time interval such that we can observe convergent behavior of fourth-order statistics and whether the convergent behavior is described by WTT. To have a definite answer on this question, longer simulations are needed which will be a topic of future work.

To consider the average behavior of a family of quartets, we use a similar technique to that

of [1] to create a cluster of modes around each of the four modes of an exact resonant quartet. Specifically, for an exact quartet $(\boldsymbol{k}_0^e, \boldsymbol{k}_1^e, \boldsymbol{k}_2^e, \boldsymbol{k}_3^e)$, we construct a family of quartets $(\boldsymbol{l}_0, \boldsymbol{l}_1, \boldsymbol{l}_2, \boldsymbol{l}_3)$ at its vicinity by choosing all $\boldsymbol{l}_i$ with $|\boldsymbol{l}_i - \boldsymbol{k}_i^e| \leq 4$ for $i = 0, 1, 2, 3$. We then evaluate $f_F(\Omega)$ from (2.59) by summing over those quartets $(\boldsymbol{l}_0, \boldsymbol{l}_1, \boldsymbol{l}_2, \boldsymbol{l}_3)$ with frequency mismatch Ω on both sides of the equation. Under this evaluation $f_F(\Omega)$ reflects the closure behavior averaged over $O(10^3)$ quartets. Figure 4.7 shows $f_F(\Omega)$ computed from three representative families of quartets, defined via exact quartets $(\boldsymbol{k}_0^e, \boldsymbol{k}_1^e, \boldsymbol{k}_2^e, \boldsymbol{k}_3^e)$. We see that $f_F(\Omega)$ is somewhat inversely proportional to Ω superposed with many fluctuations. While the general trend of $f_F(\Omega)$ seems consistent for different families, the details (e.g, the value of $f_F(0)$ as well as the fluctuation patterns) vary considerably across different families.

We finally examine the closure behavior considering the average over an enormous number of quartets, chosen as all quartets contributing to the energy flux across $k_b = 23$. Under (2.61), $f_P(\Omega)$ is computed via summation over $O(10^9)$ elements for each Ω (see Figure 4.4d). The numerically resolved $f_P(\Omega)$ is plotted in Figure 4.8 at several different nonlinearity levels. We remark that these results are convergent in the sense that they are not sensitive to the length of the time window T_w (we have checked that using $T_w/4$ as the time window leads to the same result). It is clear that under this level of average, $\int_\Omega f(\Omega) d\Omega \sim O(\pi/2)$ is consistent with WTT. We do not expect $\int_\Omega f(\Omega) d\Omega$ to be exactly $\pi/2$ unless we can numerically reach the kinetic limit (see our evaluations of $f_P(\Omega)$ in Chapter 5). To quantify the profile of $f_P(\Omega)$, we use a least-square method to fit the data to a general functional form of $f_P(\Omega) = C/(\rho + \Omega^\beta)$, where ρ is needed as a desingularisation factor for $f_P(0)$. These fittings, as shown in Figure 4.8, agree with all data points remarkably well, with $C = [1.06, 0.982, 0.875]$, $\rho = [6.176, 3.44, 2.26]$, and $\beta = [1.35, 1.47, 1.52]$ from high to low nonlinearity level. Instead of a sinc-like function (which involves either negative values or oscillatory behavior with neither observed), the functional form of $f_P(\Omega)$ is somewhat closer to the WTT form of $\epsilon/(\Omega^2 + \epsilon^2)$, but with different exponents β. This is probably why [77] find that the WKE employing this WTT form of generalized delta function produces physically reasonable results in terms of the spectral slope and energy flux for capillary waves.

4.3 Discussion

While this chapter sheds new light on the physics of energy flux in wave turbulence, more unanswered questions, especially regarding the closure model, are raised. The closure model is a subject that has received insufficient attention from a numerical perspective, especially in terms of analysis utilizing data generated directly from the primitive dynamic equation. The few exceptions to this [e.g. 61, 1, 92] have not considered the detailed functional form and magnitude of $f(\Omega)$, as studied in this work. Therefore, we consider the primary importance of this work as to provide

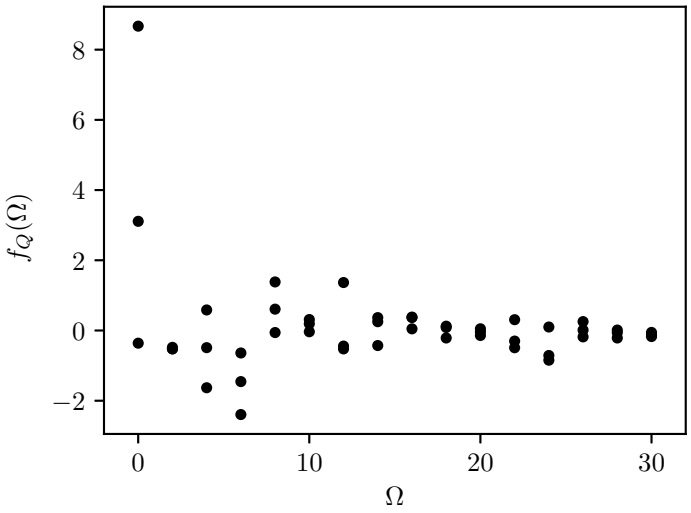

Figure 4.6: The function $f_Q(\Omega)$ evaluated for $O(50)$ selected quartets (with 3 quartets for each Ω) with $T_w = 256T_0$, for the highest nonlinearity level with $\overline{P} = 81.9$.

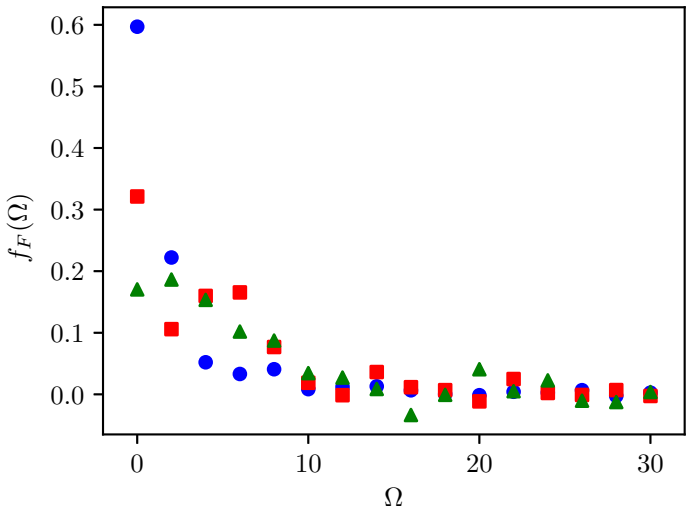

Figure 4.7: The function $f_F(\Omega)$ for three representative families of quartets defined by $\boldsymbol{k}_0^e = (-2, 8)$, $\boldsymbol{k}_1^e = (-10, 0)$, $\boldsymbol{k}_2^e = (14 + 4j, -8 - 4j)$, and $\boldsymbol{k}_3^e = (6 + 4j, -16 - 4j)$ for $j = 0$ (●), $j = 1$ (■), and $j = 2$ (▲). The evaluation is for the highest nonlinearity case of $\overline{P} = 81.9$ with $T_w = 256T_0$.

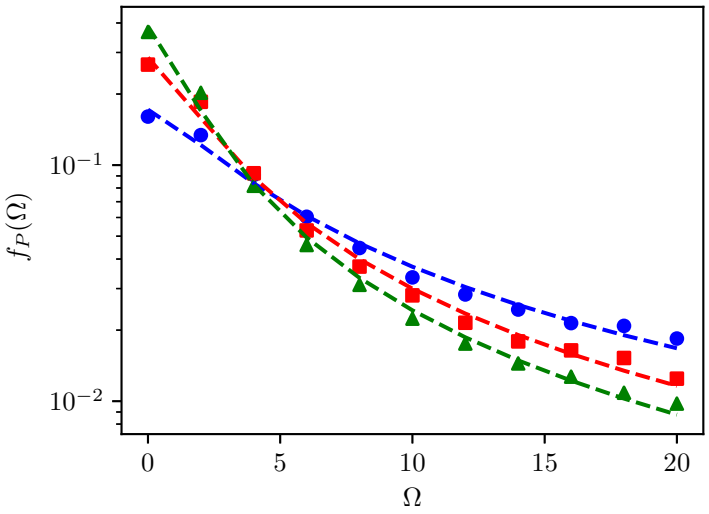

Figure 4.8: The function $f_P(\Omega)$ with $k_b = 23$ and $T_w = 256T_0$, for different nonlinearity levels with $\overline{P} = 81.9$ (●), 42.8 (■), and 28.0 (▲). Fits to the data of the form $f(\Omega) = C/(\rho + \Omega^\beta)$ are indicated (- - - -).

a methodology such that many open questions in wave turbulence can be directly studied using vast numerical data. Within the presented results, for example, the function $f_Q(\Omega)$ in Figure 4.6 is still sensitive to the time window T_w used for averaging for each individual quartet. It is not clear whether a convergent behavior (close to the quartet-averaged result $f_P(\Omega)$) can be found if a time average over an extremely long time window is performed. In addition, will the smooth behavior associated with function Q_Ω be preserved in different domain geometries (e.g., an irrational torus as in [46]) where the normalization factor $\mathcal{N}_\Omega$ substantially varies? While we did not detect such a relationship in our study in Chapter 5, there remains much work to be done on this problem.

Questions such as these can be explored in greater detail with increasing computational resources, and it is certainly not unreasonable to think about studying wave turbulence with "exascale computing", an area under development for hydrodynamic turbulence [e.g. 98]. For wave turbulence, these resources may be better utilized in conjunction with an understanding of WTT, rather than simply boosting the resolution of simulations. This is demonstrated by the strong results in Chapter 5 regarding $f_P(\Omega)$ on the 1D MMT model, and we envision similar, more extensive studied may performed on the plethora of physical systems that exhibit WT.

4.4 Summary

In this chapter, we numerically study the properties of inter-scale energy flux P for wave turbulence in the context of the 2D MMT equation. Unlike previous evaluations of P based on energy

input or dissipation rate, our formulation of P computes the exact instantaneous energy flux across arbitrary scale k_b directly from the nonlinear terms in the MMT equation, and allows a quartet-level decomposition of P into P_Ω according to the frequency mismatch Ω of the quartets. Our results show that the energy flux P across any scale in the inertial range closely follows a Gaussian distribution, with their mean value $\overline{P}$ almost a constant for any k_b, and standard deviation $\sigma(P)$ increasing with k_b. In addition, values of $\sigma(P)$ are generally several orders of magnitude larger than $\overline{P}$, mainly due to the contributions to $\sigma(P)$ from quasi-resonances, i.e., $P_{\Omega>0}$. The decomposition of P into P_Ω also allows an alternative but more direct measure of nonlinear broadening by quantitatively considering the contribution of quasi-resonances to the mean energy flux. We further study the scaling of spectral level N with the energy flux and find that $N \sim \overline{P}^{1/3}$ (consistent with the kinetic scaling) at high nonlinearity and $N \sim \overline{P}^{1/2}$ (dynamic scaling) at low nonlinearity. The former and latter are due to the dominance of the quasi-resonant and exact-resonant contributions to $\overline{P}$, respectively. Finally, our numerical study on the wave-turbulence closure model shows that the fourth-order correlator evaluated over a finite time window is in disagreement with the description by the theoretical closure on a single quartet level. When considering the average over all quartets contributing to the inter-scale energy flux (over $O(10^9)$ quartets for each Ω), a more consistent behavior to the theoretical closure is observed, but with the broadening function exhibiting $1/\Omega^\beta$ (with β between 1.3 and 1.6) different from the forms derived in WTT.

CHAPTER 5

Wave Turbulence in the Kinetic Limit

In this chapter, we evaluate the 1D MMT model with $\alpha = 1/2$ and $\beta = 0$, the equation for which we derived the KZ spectrum in Chapter 2. While Chapters 3 and 4 explored the transition between the DWT and KWT regimes via novel numerical techniques, in this chapter we apply those ideas to study wave turbulence *in the kinetic limit*. The goal of this study is therefore to develop and employ precise, quantitative assessments of how well the WT closure and the KZ spectrum represent the statistics of MMT model as we approach the kinetic limit. To do this, we set up a series of forced-dissipated numerical experiments that form stationary wave turbulence. We choose the forcing such that a range of nonlinearities ε are represented, and for each of these cases, we progressively double the domain size while keeping the maximum wave number constant. As ε is made small and L made large, this numerically approximates the kinetic limit. We then study the spectra and energy cascades associated with these fields, placing a particular focus on convergence of these quantities to WTT predictions.

5.1 Setup of Numerical Experiment

We solve (2.1) on a 1D domain of length L. To create a steady forward energy cascade, we add Gaussian forcing between for all modes $10 \leq |k| \leq 20$. We additionally add dissipation of the form (2.14), where

$$\nu_{\boldsymbol{k}} = \begin{cases} 3k^{-4} & 0 < k \leq 10 \\ 1 \times 10^{-14}(k - 900)^8 & k \geq 900 \\ 0 & \text{otherwise.} \end{cases} \tag{5.1}$$

Every simulation we perform in this Chapter begins with $\hat{\psi}_k = 0$. The final nonlinearity of the field is determined by the forcing strength σ_F, the standard deviation of the Gaussian forcing in (2.14), and we simulate each field until a steady spectrum is reached, after which we collect statistics from time data.

To numerically approximate the kinetic limit, we choose four domain sizes of $L \in [2\pi, 4\pi, 8\pi, 16\pi]$ where the number of modes used in each of these domains is selected such that $k_{\max} = 1024$ is always the maximum resolved wave number. Recall that the effect of doubling L is to half the wave number spacing Δk. Thus, on the largest of these domains, we simulate 3 decades of k in the positive and negative wave number directions, with $\Delta k = 1/8$ requiring 16385 alias free modes. For each domain size, we choose four values of forcing strength, leading to four fields of very different nonlinear strength $\varepsilon \equiv H_4/H_2$.

The parameters of these numerical simulations are chosen very carefully to ensure that, for each forcing strength, key aspects of the dynamics remain close to constant as L is made large, while others are allowed to vary. This turns out to be a non-trivial task. Given the definition (2.2), the spectral amplitude $\hat{\psi}_{\boldsymbol{k}}$ is normalized such that the length-averaged total action does not depend on L, as can be seen via Parseval's theorem [69],

$$\frac{1}{L}\int_0^L |\psi_{\boldsymbol{x}}|^2 d\boldsymbol{x} = \sum_{\boldsymbol{k}\in\Lambda_L^2} |\hat{\psi}_{\boldsymbol{k}}|^2. \tag{5.2}$$

For a fair comparison between domains of different L, we would like to keep the length-averaged Hamiltonian density H approximately constant as L increases. We attempt this by keeping the action injection rate, controlled by σ_F, and the dissipation rate, controlled by $\nu_{\boldsymbol{k}}$, the same across domains of different L at each ε of interest. After a careful scaling analysis, we determine that this is achieved by $\nu_{\boldsymbol{k}}$ remaining constant in L, while $\sigma_F \sim 1/\sqrt{L}$. Under this scheme, we find the length averaged quantities of total action N, total energy H, and the nonlinearity ε remain close to constant as L increases. More generally, we are interested in observing convergent behavior in all of these quantities we increase L, to determine their limiting behavior. On the other hand, by (5.2), a fair comparison of quantities evaluated at an individual mode must be somehow scaled by L. Hence, we slightly modify the definition (2.51) for this chapter, to now be $n_{\boldsymbol{k}} = \frac{L}{2\pi}\overline{|\hat{\psi}_{\boldsymbol{k}}|^2}$. Additionally, in this chapter, all dimensional quantities involving total action or energy, including P, will be length averaged. We proceed by discussing the wave action spectra.

5.2 Spectra

We begin by presenting the steady, directionally-averaged spectra for all 16 simulations in Figure 5.1a. From highest to lowest spectral level, an order of magnitude in nonlinearity is spanned, with $\varepsilon \in [0.0066, 0.067]$. We define $\varepsilon \equiv H_4/H_2$. For the higher nonlinearity results, we see excellent agreement in spectral form for all L, suggesting all represented domain sizes represent the large-L limiting spectral form of the KWT regime. In the weakest nonlinearity case, however, we see the

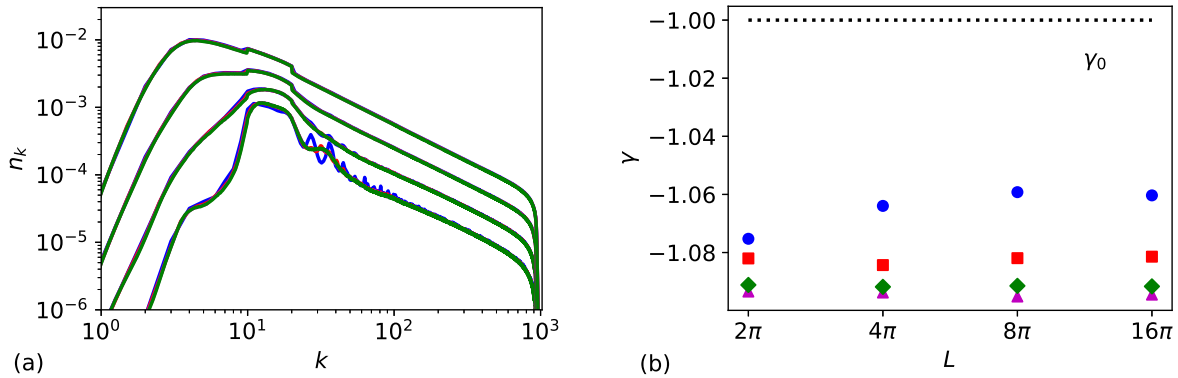

Figure 5.1: (a) A representative collection of fully-developed, angle-averaged wave action spectra n_k. (b) Spectral slope γ as a function of L.

region near the spectral peak changes substantially. These secondary peaks for $L = 2\pi$ and $L = 4\pi$ are representative of finite-size effects [102], however at larger L, these peaks disappear, suggesting a transition from the DWT regime to the KWT regime.

The inertial range spectra at all four ε take a power-law form, each spanning at least 1 order of magnitude. We define the inertial range to a reasonable $k \in [70, 700]$, and plot the measured γ in Figure 5.1b. At higher nonlinearities, the spectral slope γ is mostly invariant in L, with the second highest nonlinearity case slightly steeper than the highest. At lower nonlinearities, we observe a relatively weak trend towards the KZ value of $\gamma_0 = -1$. The lowest nonlinearity, smallest L cases that exhibited secondary peaks also exhibit slightly steeper spectra, which are often associated with finite-size effects (see Section 1.3.2). As L is increased, these cases approach a shallower value for γ. We emphasize that these trends are subtle, however. Perhaps the strongest spectral feature of the inertial range dynamics is that, as ε decreases, the width of the power-law region shrinks substantially. Also, at low nonlinearity, we see slightly greater fluctuations around a true power-law form near the ends of the inertial interval. We discuss some possible reasons for this later in this chapter. Next, we present our measurements of energy flux.

5.3 Energy Flux

Figure 5.2 depicts the mean energy flux $\overline{P}$ through $k_b = 300$ for every simulation. Several decades of energy flux are represented by our data, with minimal variation in L. Next, we look at the flux distribution $P(k_b = 300, t)$ and the flux of the nonlinear energy H_4 (given by P_4), depicted in Figure 5.3a/b. Results only for the highest nonlinearity case are shown, however they are representative of the other cases. Both P and P_4 take a Gaussian distribution whose standard deviation is much

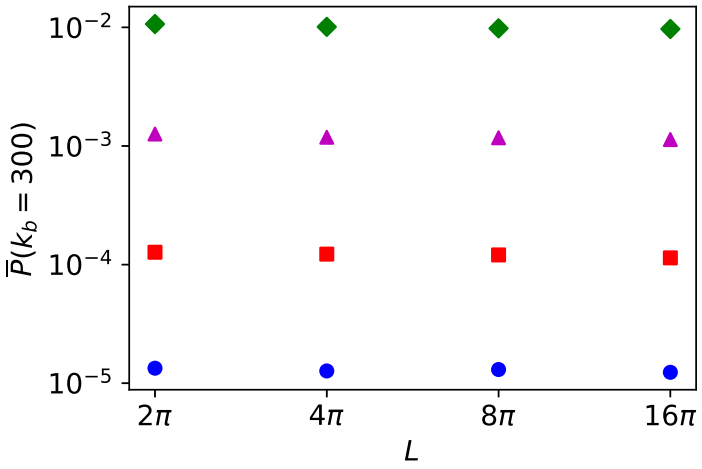

Figure 5.2: The mean energy flux $\overline{P}$ through $k_b = 300$ as a function of L, for $\varepsilon = 0.067$ (♦), $\varepsilon = 0.030$ (▲), $\varepsilon = 0.014$ (■), and $\varepsilon = 0.0067$ (●).

larger than its mean. This is an identical result to that of Chapter 4, where the 2D case with the NLS dispersion relation was evaluated. This similarity suggests a Gaussian energy cascade is a general feature of wave turbulence. In fact, a simple argument supports a Gaussian energy cascade: first, consider the form of (2.53), which expresses the instantaneous inter-scale flux as a sum over a large number of modes. If the the instantaneous time rate of change of H_2 at each of these modes is assumed to be independent, as is suggested by WTT [69, 30], then the Central Limit Theorem (CLT) can be used to show $P(k_b, t)$ approaches a Gaussian distribution as the number of modes in the domain becomes large. As L is increased, the standard deviation of both fluxes is decreased, as indicated in Figure 5.3c. The data shows a clear trend where $\sigma(P) \sim 1/\sqrt{L}$. This too can be explained in the context of the CLT, as the variance of $P(k_b, t)$ is given by a large sum over $\sigma^2(\frac{d|\hat{\psi}_{\boldsymbol{k}}|^2}{dt})$. This scales linearly with the number of modes with $k < k_b$, which scales linearly with L. On the other hand, one can use the instantaneous form of (2.54) to show that $\sigma^2(\frac{d|\hat{\psi}_{\boldsymbol{k}}|^2}{dt}) \sim 1/L^2$, given that $|\hat{\psi}_{\boldsymbol{k}}| \sim 1/\sqrt{L}$ by Parseval's theorem (5.2). The end result is that $\sigma^2(P(k_b, t)) \sim 1/L$, leading to the desired $\sigma(P(k_b, t)) \sim 1/\sqrt{L}$. Interestingly, the flux of P_4 is negative on average, i.e., goes from the small scale to the large scale. This is better depicted in Figure 5.3d, where the averaged $\overline{P}(k_b)$, $\overline{P}_4(k_b)$ and their sum is shown. The slight variation in $\overline{P}(k_b)$ throughout the inertial range is due to uncertainty in the estimate of the mean from high-variance data. We also note the relative difference between the mean flux of the linear energy H_2 ($\overline{P}(k_b)$) and the flux of true energy H ($\overline{P}(k_b) + \overline{P}_4(k_b)$) is on the order of the nonlinearity represented in this figure ($\varepsilon = 0.067$).

In Figure 5.4, we provide the steady time distribution of dissipation rate, defined via the

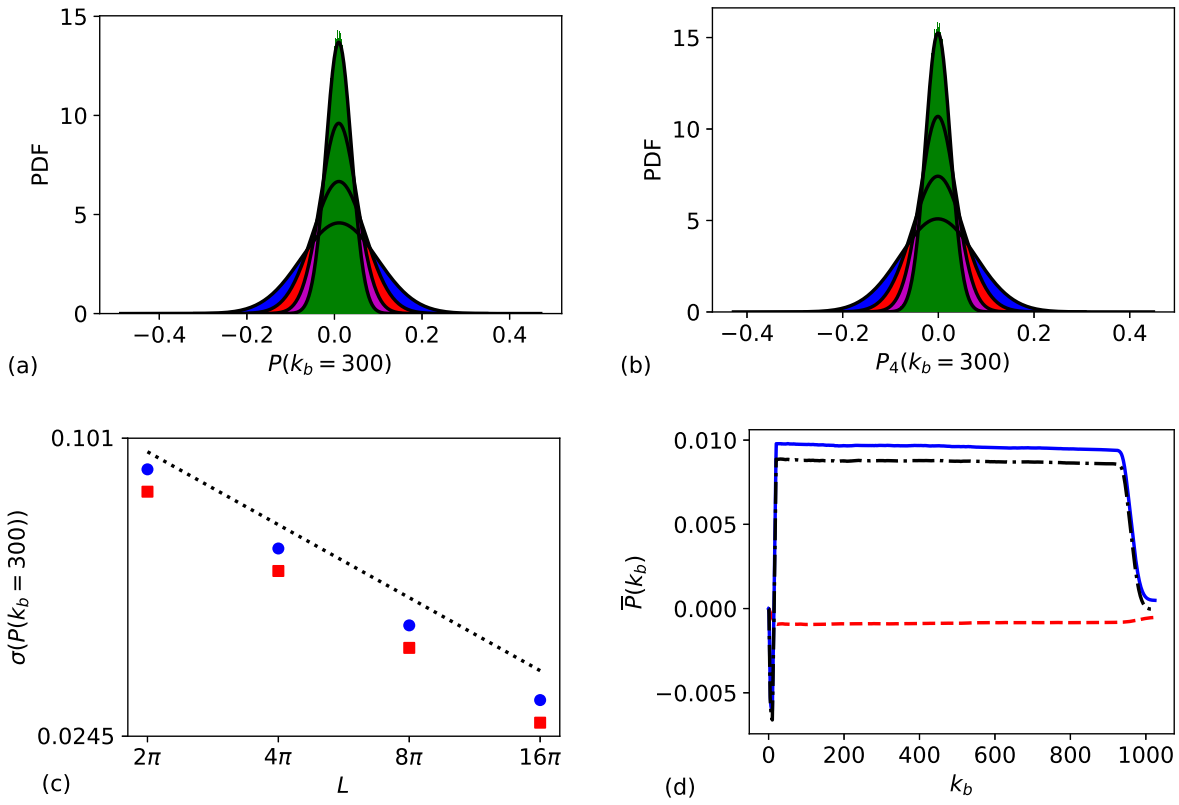

Figure 5.3: The time-distribution, through $k_b = 300$, of linear energy flux P (a) and nonlinear energy flux P_4 (b) for the $\varepsilon = 0.067$ data for various L, with higher peak height corresponding to larger L. Gaussian distributions of equal mean and standard deviation are marked (——). (c) The log-log-scale standard deviation of P (●) and P_4 (■) as a function of L with (· · · · · ·) indicating $\sigma \sim 1/\sqrt{L}$. (d) The time-averaged $\overline{P}$ (——), $\overline{P}_4$ (- - - -), and their sum (— · —) as a function of k_b.

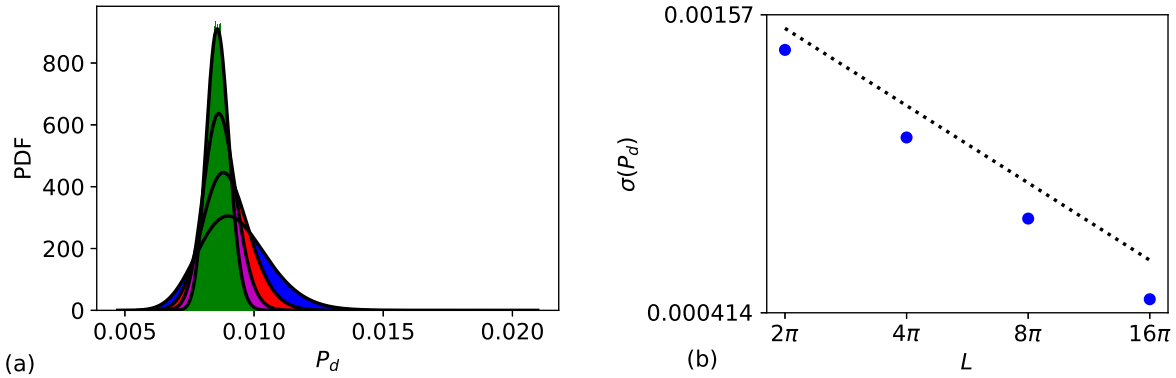

Figure 5.4: (a) The time-distribution of linear energy dissipation rate P_d for the $\varepsilon = 0.067$ data for various L, with higher peak height corresponding to larger L. Log-normal distributions of equal mean and standard deviation are marked (——). (b) The log-log-scale standard deviation of P_d as a function of L with $(\cdots\cdots)$ indicating $\sigma \sim 1/\sqrt{L}$.

instantaneous form of (2.52). The data exhibits the same scaling of standard deviation with respect to L by vary similar arguments, however the distribution is Log-normal, rather than Normal (Gaussian). Log-normal distributions of dissipation rate in flow turbulence have received some attention [62], however we are not aware of similar results in WT. We discuss this finding in detail in the discussion section of this chapter.

To study the energy cascade further, we employ the decomposition technique (2.57). The resulting decomposition of the flux through $k_b = 100$ is depicted in Figure 5.5a. We reduce to $k_b = 100$ to lessen the computational cost of obtaining this decomposition, which scales with k_b. As depicted in Figure 5.5b, this system has very few exactly resonant interactions ($\Omega = 0$), which differs significantly from the case of $d = 2$ and $\alpha = 2$ explored in earlier chapters. In fact, the argument regarding rectangles presented in Chapter 1 and Appendix B does not apply for this system with $d = 1$ and $\alpha = 1/2$. Instead, via arguments similar to those used in Appendix A, one can show that the Continuous Resonant Manifold for this system seldom aligns with a rational wave number grid. As a result of this, even when ε is very small, (effectively) the entirety of the energy flux is carried by quasi-resonant interactions. We measure the contribution due to exactly resonant interactions to be orders of magnitude lower than the near-resonant interactions. Further, we see that, as expected by the kinematic model and our results in Chapter 4, nonlinear broadening Γ grows considerably as ε is increased. Here Γ is the width (alternatively, the decay rate) of the decomposition in Ω. While the total mean flux should stay constant through the inertial range due to the stationary n_k, it is not *a priori* clear that the flux decomposition should remain invariant. We have verified that, for larger k_b in the inertial range, an almost identical plot is recovered. This fact extends to following analysis of the closure as well. We also show in Figure 5.5b that the

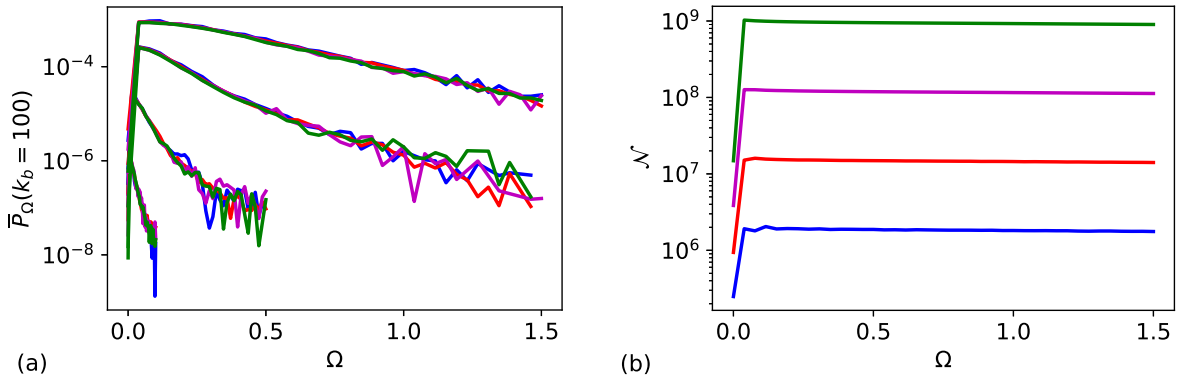

Figure 5.5: (a) The Ω-decomposition of $\overline{P}$ for all of our data, with (blue) indicating $L = 2\pi$, (red) indicating $L = 4\pi$, (magenta) indicating $L = 8\pi$, (green) indicating $L = 16\pi$, with higher data corresponding to higher ε. (b) The number of interactions $\mathcal{N}$ of each Ω that contribute to $\overline{P}_\Omega$ for the measurement at $\varepsilon = 0.067$.

number of interactions at each Ω is strongly influenced by L. Despite this, the length-averaged mean flux carried by all interactions with a given Ω is mostly constant in L. Finally, we note that, as the tails of these decompositions approach 0, the relative uncertainty in their measurement increases (again, due to a highly-variable distribution), which leads to fluctuations, sometimes even to negative values of $\overline{P}_\Omega$. For this reason, we have omitted the few negative tail values for the clarity of Figure 5.5a, as well as the coming Figure 5.6, which is directly computed from $\overline{P}_\Omega$.

5.4 Closure Model Study

We now compute the closure function $f_P(\Omega)$, which is presented for the largest L case at each nonlinearity in Figure 5.6. In this figure, the very few interactions with $\Omega = 0$ are excluded from the plot, as a low uncertainty measurement of $f_P(\Omega)$ is not possible with our data. This is not an issue, however, as the WT closure is said to describe the effective behavior of quasi-resonant interactions. As observed in Chapter 4, we find that f_P takes the expected form of a generalized Delta function. We note in particular the peak measured value of $f_P(\Omega)$ varies by a factor of 30 given a single order of magnitude difference in ε, demonstrating expected δ-concentration on the resonant manifold as the kinetic limit is approached. Also depicted in Figure 5.6 is a fit of the form $f_P(\Omega) = a/(a^2 + \Omega^2)$, which fits the data reasonably well. We prefer a fit to this form of generalized delta function over the more general form used in Chapter 4, as this form more directly resembles the theoretical form obtained by Zakharov in [101]. As with our other results, we do not see large variation in the closure function at any given ε for changes in L (not shown here). We do, however, detect subtle and important changes in the area under $f_P(\Omega)$ across our data, which we

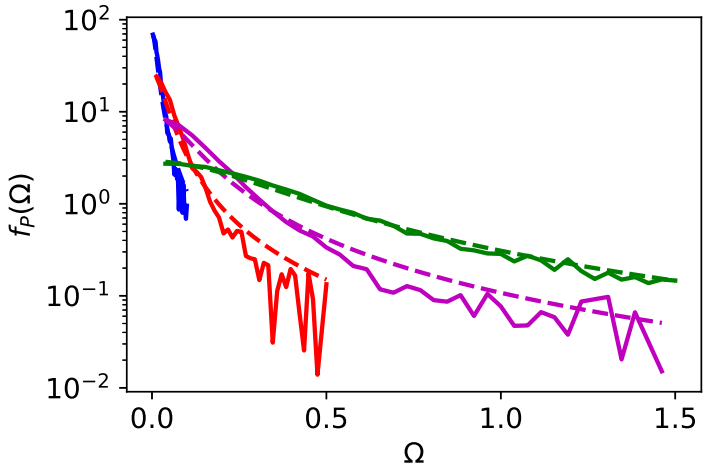

Figure 5.6: The closure function $f_P(\Omega)$ (——), with steeper data corresponding to smaller ε. A fit to the form $a/(a^2 + \Omega^2)$ is at each ε is provided (- - - -).

discuss next.

According to WTT, our generalized Delta function $f_P(\Omega)$ is expected to integrate to $\pi/2$ in the kinetic limit. This is an extremely important aspect of WTT, as it effectively determines the Kolmogorov constant and, in a very related way, quantifies the convergence of a sum over a lattice of quasi-resonant interactions to an integral over the continuous (exactly) resonant manifold. Therefore, we assess the relative error in the integral of f_P from $\pi/2$, given by

$$\rho = \frac{\pi/2 - \int_0^{\Omega_{\max}} f_P(\Omega) d\Omega}{\pi/2}, \tag{5.3}$$

where $\Omega_{\max}$ is chosen to be sufficiently large. The result is depicted in Figure 5.7, where there is clear convergence towards the expected value of ρ in the kinetic limit. This result is in contrast to the other results of this chapter, in which little variation is shown in L - here, it is clear that the WT closure, as realized on a finite domain, is quantitatively a better model for mean energy flux as L becomes large for sufficiently small ε. We expect that, in the smallest nonlinearity case, the trend towards decreasing ρ would continue on larger L. It is also interesting that, for $L = 2\pi$ with a fairly large separation of forcing and dissipation scale, that the limiting behavior of L is not well resolved for any ε. On the other hand, the relative error ρ is never too large, indicating the WT closure is never far from well-predicting the inter-scale flux on any of these domains.

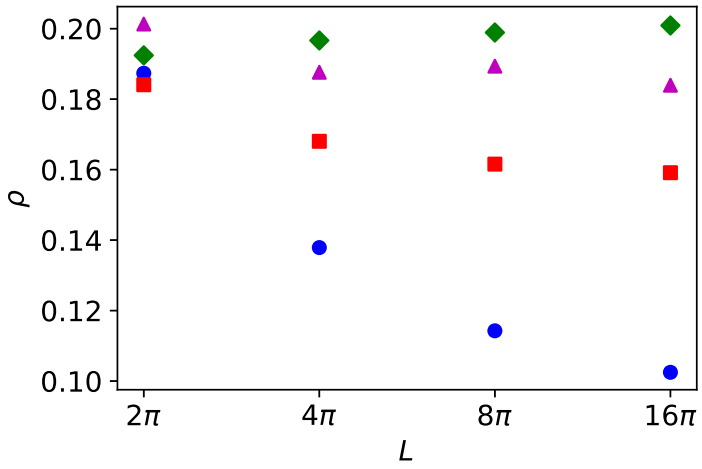

Figure 5.7: The relative error in the integral measure of $f_P(\Omega)$ from theory, given by ρ for $\varepsilon = 0.067$ (♦), $\varepsilon = 0.030$ (▲), $\varepsilon = 0.014$ (■), and $\varepsilon = 0.0067$ (●).

5.5 Discussion

With regards to the implications of this work, we start by pointing out that WT studies that vary both L and ε with the goal of studying the WT closure are few and far between, particularly so for studies of stationary, out-of-equilibrium spectra. We find for all tested L that the majority of quantities of interest are close to their large-L limiting values. This is an encouraging result for the application of WTT to finite-domain dynamics, particularly with regards to existing numerical studies of the WT closure on domains of size $L = 2\pi$ with similiarly large inertial intervals to ours. We also find that the WT closure is found to well-approximate the energy flux quantitatively on every domain of interest, with the error tending towards zero in the kinetic limit. This is a striking result, particularly given that this is found after integration over many times the kinetic time scale, a regime of time scale for which the WKE is not explicitly derived. On a related note, our new insights extend also to the form of the measured $f_P(\Omega)$, which conspicuously agrees with the derivation in [101]. We remark that that a major difference in various derivations of the WKE is the form of the closure function $f(\Omega)$, which shares a connection to the definition of kinetic time scale, as shown in Chapter 2. We hope that our measurements may point the way towards a unification of the theory in this regard, if only by providing the form of $f(\Omega)$ in the long time limit. This is all predicated on the fact that $f(\Omega)$ is indeed the same for each quartet in the domain. With enhanced computational power, this may be validated as future work using techniques similar to ours.

The WKE closure may further be studied by comparison of our numerical results to the Kolmogorov constant C_0, which we have derived for this system (see Chapter 2). The comparison

of numerically obtained, finite-domain spectra and energy fluxes to the derived KZ spectrum is a non-trivial task, however, as the comparison must be accurate to a constant in order to be meaningful. This requires careful consideration of the manner in which finite-domain and infinite-domain quantities are compared, which we leave to future work. That γ subtly approaches γ_0 is an encouraging result for observing convergence in the numerical kinetic limit. On the other hand, such a study may also help elucidate the reason for the shrinking inertial interval as $\varepsilon \to 0$, as it would reveal discrepancies between the KZ spectrum, derived for an infinite inertial interval without explicit forcing and dissipation, and the steady, out-of-equilibrium spectra obtained by DNS that violates these assumptions. As discussed in the introduction, the breakdown of KZ spectra is often associated with instabilities and non-locality [101]. If these mechanisms depend somehow on ε, it may help explain the trend in inertial interval size. This also remains for future work.

On the topic of flux distributions, we place our findings in the context of a growing trend towards probabilistic approaches to WT, in which full probability distributions are described by the WT formalism [69, 30, 12, 70], rather than only single moments. In particular, we draw attention to the Log-normal PDF of dissipation rate observed in this work. The Log-normal distribution is often associated with multiplicative random processes, and even multi-fractal physics [62]. Further development of WTT along these lines may reveal undiscovered physics of dissipation in WT. On the practical side, the arguments and observations of this work indicate that dissipation rate variance is inversely proportional to the number of modes involved in the dissipative process. While further study is required, this suggests broadening the dissipation range by choice of $\nu_{\boldsymbol{k}}$ may reduce variation in dissipation rate.

5.6 Summary

In this chapter, we present numerical studies of statistically steady wave turbulence with a forward cascade of energy. By changing forcing strength to vary the nonlinearity of steady WT, and through carefully doubling the corresponding domain sizes, we can approximate the kinetic limit of WTT. This allows us to evaluate convergence to WTT predictions via quantitative analysis. We find that, for all tested ε and L, our data is close representative of the large L limit, with the exception of the weakest nonlinearity results. For the range of parameters tested, we observe that the spectral form is in fairly good agreement with the KZ value of γ_0, however the inertial interval shrinks in the small nonlinearity limit, regardless of tested domain size. We show both the linear and nonlinear energy flux are Gaussian in distribution, with strong fluctuations, and that dissipation rate is Log-normally distributed. The variance of these quantities is inversely proportional to L. Further, the mean flux of H_4 is in the inverse direction. Our flux decomposition technique reveals nonlinear broadening decreases with ε. Critically, we find via a quantitative study of the closure model that the error in

the WT closure in predicting energy flux becomes small in the numerical kinetic limit.

CHAPTER 6

Weakly Nonlinear Breather Solutions

In this chapter, we demonstrate the existence of breather solutions to the MMT model realized in 2D domain with periodic boundary conditions. This corresponds to a family of (non-local) derivative Nonlinear Schroedinger equations (NLS) without potentials. Here we use a physical definition of breather as spatial localization of energy occurring in a periodic or quasi-periodic pattern in time. In addition to being a novel 2D breather in a continuous field, other remarkable and distinguishing features of the breather include: (1) the breather spontaneously emerges from a stochastic wave field after long-time evolution, not relying on specific initial conditions; (2) the breather appears equivalently for both the focusing and defocusing cases, but exists only in the weak nonlinearity regime. As the nonlinearity of the system increases, we find a breakdown of the breather state with the field relaxing to the Rayleigh-Jeans spectrum. Further analysis suggests a connection of these results with Kolmogorov-Arnold-Moser (KAM) Theory.

6.1 Setup of Numerical Experiments

We compute the unforced, undissipated, defocusing ($\lambda = 1$) MMT model (2.1) with $\alpha = 2$ on a 2D domain with periodic boundary conditions, starting from an initial field $\psi_0 \equiv \psi(\boldsymbol{x}, t = 0)$, with 128×128 modes. Higher resolution results available in Appendix C. The initial field ψ_0 is set as an exponential form in Fourier space as $\hat{\psi}_0(\boldsymbol{k}) = A\exp[-0.1|k - k_p| + i\theta_{\boldsymbol{k}}]$, where $k_p = 4$, and $\theta_{\boldsymbol{k}}$ is a random phase that is decorrelated for all $\boldsymbol{k}$ (i.e., $\theta_{\boldsymbol{k}}$ for each $\boldsymbol{k}$ can be thought of as independent, identically-distributed random variables). In order to investigate dynamics at different nonlinearity levels, we choose a range of A leading to approximately $\varepsilon \in [0.0005, 0.1]$ for each β value of interest, where $\varepsilon \equiv H_4/H_2$.

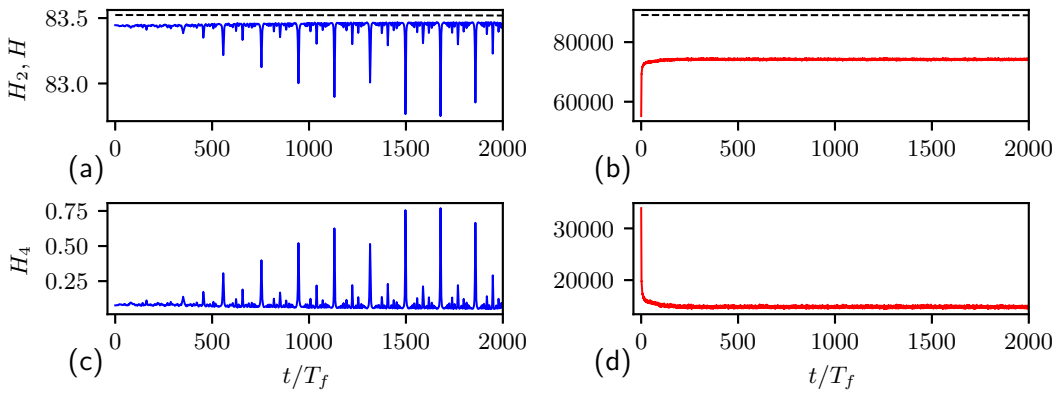

Figure 6.1: The time series of H (dashed) and H_2 (solid) for (a) $\varepsilon = 0.00071$ and (b) $\varepsilon = 0.20$, as well as the corresponding H_4 for (c) $\varepsilon = 0.00071$ and (d) $\varepsilon = 0.20$. Note that a low sampling frequency is used to plot the figure to improve its readability, leading to aliasing. Therefore, only a small portion of all $O(1600)$ peaks are visible.

6.2 Results

We start by describing a typical simulation leading to a breather state, with parameters $\beta = 3$ and $A = 35$ (corresponding to $\varepsilon = 0.00071$). Figures 1a and 1c show the long-time evolution of H_2 and H_4 from $t = 0$ to $2000T_f$, with $T_f = 2\pi$ the period of the fundamental wave mode. The total Hamiltonian H, as shown in Figure 1a, is well conserved over $2000T_f$. After an initial evolution of about $400T_f$ with smooth profiles of H_2 and H_4, we observe that H_4 undergoes strong periodic jumps with corresponding dips in H_2. These jumps are associated with coherent structures, which are only present at low nonlinearity. In contrast, as demonstrated in Figures 1b and 1d, the field evolution at a higher nonlinearity ($\varepsilon = 0.20$) exhibits smooth profiles of H_2 and H_4 over the same time interval.

The oscillations in H_4 correspond to oscillations of a breather. To better visualize this breather state, we plot in Figure 6.2 the real part of $\psi_{\boldsymbol{x}}$ at different phases of its oscillations (i.e., different stages of the oscillation pattern in H_4). Fig. 6.2a shows the field right before the first jump of H_4, where a concentric wave appears and later converges into a breather peak seen in Fig. 6.2b. This peak then collapses, with a second one emerging after about $T_f/2$ (according to Fig. 6.2e) at the maximally distant location in the periodic domain, shown in 6.2c. The cycle then repeats itself with a peak emerging in Fig. 6.2d (at the same location as in 6.2a), forming a breather solution coexisting with a stochastic wave background. The smaller peaks of H_4 seen in Fig. 6.2e correspond to groups of secondary peaks in $\psi_{\boldsymbol{x}}$. From Figure 6.2 we see that the breather oscillates with a fundamental period very close to T_f. Therefore, the simulation in Figure 1a/c covers $O(1600)$ cycles of the breather, demonstrating a very long (perhaps infinite) time of existence.

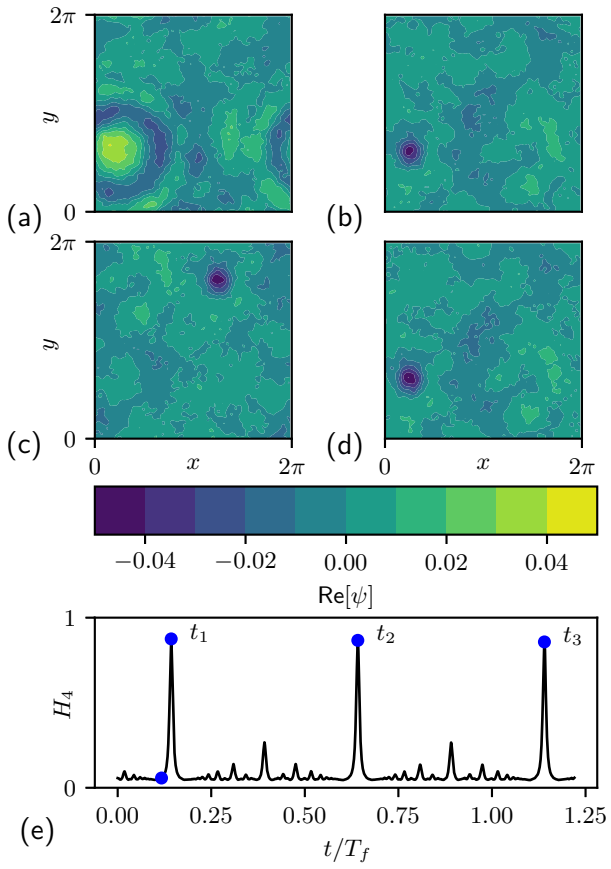

Figure 6.2: Contour plots of $\mathrm{Re}[\psi_{\boldsymbol{x}}]$ at $\beta = 3$ for $\varepsilon = 0.00071$ at various stages of the cycle of the breather (a/b/c/d), corresponding chronologically to the times marked by the blue circles in (e) the time series of H_4. Note that this plot of H_4 has sufficient sampling to resolve all features.

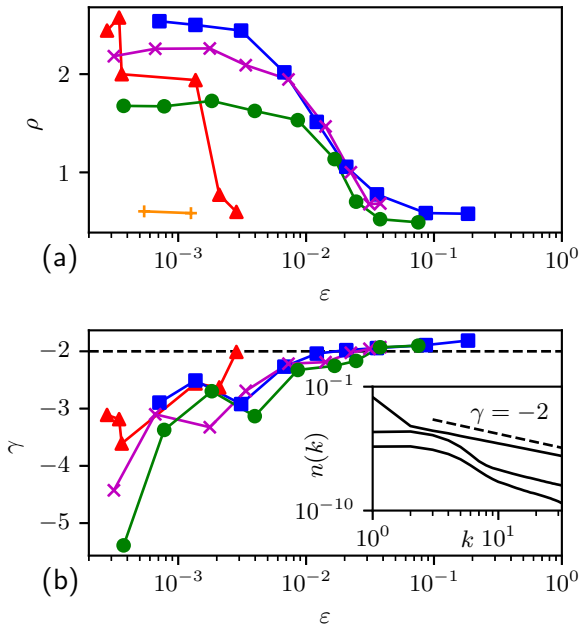

Figure 6.3: The quantities (a) ρ and (b) γ as functions of ε for $\beta = 0$ (orange +), $\beta = 1$ (green ●), $\beta = 2$ (magenta ×), $\beta = 3$ (blue ■), and $\beta = 4$ (red ▲). The inset of (b) shows fully-developed, angle-averaged wave action spectra at a few nonlinearity levels (for $\beta = 3$), with the Rayleigh-Jeans spectral slope of $\gamma = -2$ indicated (dashed).

We next investigate the existence and intensity of the breathers for varying values of β and ϵ. To measure the relative intensity of the breather, we define the peak-to-background ratio as

$$\rho = \frac{\text{avgmax}[|\psi_{\boldsymbol{x}}|]}{4\sigma_{|\psi_{\boldsymbol{x}}|}}, \tag{6.1}$$

where the avgmax operator returns the average of the maximum height of primary peaks (as in Fig. 6.2b/c/d) over many cycles of the breather, and $\sigma_{|\psi_{\boldsymbol{x}}|}$ is the total standard deviation of the field $|\psi_{\boldsymbol{x}}|$ over space and time. By definition (6.1), $\rho = 2$ corresponds to the typical rogue wave criterion used in many fields [26].

Figure 6.3a shows the value of ρ obtained for $\beta = 0, 1, 2, 3, 4$ and ε across three orders of magnitude. In general, we see that the breather state is present for smaller ε (i.e., weak nonlinearity) and becomes stronger when β is closer to 3. The case with $\beta = 0$ (corresponding to NLS) leads to no breathers, indicating the derivative is necessary for their emergence. We note that when the breathers are not present, the value of ρ is evaluated by taking the average of the maximum of the field $|\psi_{\boldsymbol{x}}|$ every $T_f/2$ as the numerator in (6.1).

Furthermore, we examine in Figure 6.3b the slope γ of the stationary wave action spectrum $n_{\boldsymbol{k}}$ across all values of β and ε. The inset of Figure 6.3b shows a typical example of fully-developed,

angle-averaged n_k for $\beta = 2$ and several values of ε. We see that the Rayleigh-Jeans spectrum with $\gamma = -2$ is only achieved at higher nonlinearity when the breather is not present. This trend is generally true for all values of β as shown in Figure 6.3b.

A few additional remarks are in order. First, we note that the breather also emerges for the focusing equation (D.6) with $\lambda = -1$ under the same conditions. Second, the breather can also be observed under a forced/dissipated system presented in Chapter 4, but with relaxation to wave turbulence spectra at high nonlinearity. Last but not least, we have performed extensive numerical analysis to verify that the breather we observe is not a numerical artifact. This includes the verification of the robustness of our results under symplectic integration, higher resolution, and different dealiasing schemes. Details of all of the above points can be found in the Appendix C.

6.3 Discussion

The breather solution in our simulation is not exactly periodic, which is evident from the slightly varying field at each moment of the breather peak (not shown here). We are interested in whether there exists a nearby trajectory which corresponds to a periodic breather. For this purpose, we have employed both a traditional spectral method [36] and a very recent variational method [3] for seeking nearby periodic solutions. As discussed in detail in Appendix D, both methods return no nearby periodic solutions. This suggests that our breather solution may be in nature quasi-periodic and requires new physical interpretation, which we provide below.

We start by stating that there exists an exact periodic solution to the linear system of (D.6), i.e., $H_4 = 0$, that closely resembles the breather we observe. What we mean precisely is that, starting from an initial condition with a breather peak (say Figure 6.2b), the field propagated by the linear equation returns to the same state after exactly T_f, which is consistent with the pattern of a breather. This is because the linear system only contains integer frequencies due to the NLS dispersion relation $\omega = k^2$, so that T_f is the period of the linear system. This fact suggests that the breather solution to the nonlinear system arises from a deformed trajectory of the linear system.

Since visualizing the high-dimensional trajectory is very difficult, we define a projection of the trajectory to some physically meaningful reference field [90]:

$$I_n = \left| \frac{\int \psi_R^*(\boldsymbol{x}, t_n)\psi(\boldsymbol{x}, t)d\boldsymbol{x}}{\int \psi_R^*(\boldsymbol{x}, t_n)\psi_R(\boldsymbol{x}, t_n)d\boldsymbol{x}} \right| \tag{6.2}$$

where $\psi_R^*(\boldsymbol{x}, t_n)$ is the reference field where a breather peak is present, e.g., taken from t_1 in Figure 6.2e, and $\psi(\boldsymbol{x}, t)$ is the solution of either the linear or nonlinear system propagated from $\psi_R^*(\boldsymbol{x}, t_n)$. Figure 6.4 shows the evolution of I_1 from both linear and nonlinear systems for a range of four

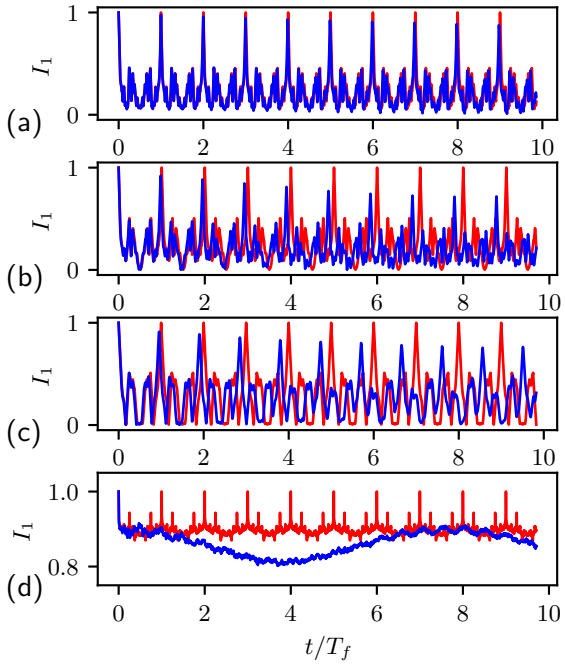

Figure 6.4: I_1 evaluated for the nonlinear system $\beta = 3$ (blue) and the linear system (red) for (a) $\varepsilon = 0.00071$, (b) $\varepsilon = 0.0084$, (c) $\varepsilon = 0.013$, and (d) $\varepsilon = 0.20$.

nonlinearity levels. It is clear that the linear system evolution exhibits a period of T_f in all subfigures as expected. When the nonlinearity level is low, the trajectory identified by I_1 shows a small deformation from the linear trajectory, as seen in Fig. 6.4a. Such deformation is consistent with a high-dimensional quasi-periodic trajectory that is evident from not only the gradual time shift of the I_1 peak, but also the deviation of I_1 peak from 1. As nonlinearity level increases, we observe an increased deformation of the trajectory, until the linear trajectory is entirely destroyed at high nonlinearity in fig 6.4d. This trajectory deformation can also be observed in the (I_1, I_2) plane in Figure 6.5.

The trajectory deformation visualized above can be connected to Kolmogorov-Arnold-Moser (KAM) theory. Specifically, if we consider the linear system as the base integrable system, then the nonlinear term can be considered the perturbation added to the system to form a nearly integrable system. Generally speaking, if the perturbation is sufficiently small, some quasi-periodic trajectories of integrable system can be preserved with small deformation to a KAM torus [27]. In our case, these preserved trajectories (i.e., KAM tori) would correspond to those associated with the breather solution observed in Figure 6.2. We also note that the linear system of equation (D.6) (or more generally the NLS) is resonant, which makes it difficult to directly apply the KAM theory. Most mathematical work of KAM on NLS relies on some way to introduce irrational frequencies, e.g., by including a potential term as in [5], and only a handful of results are available for application

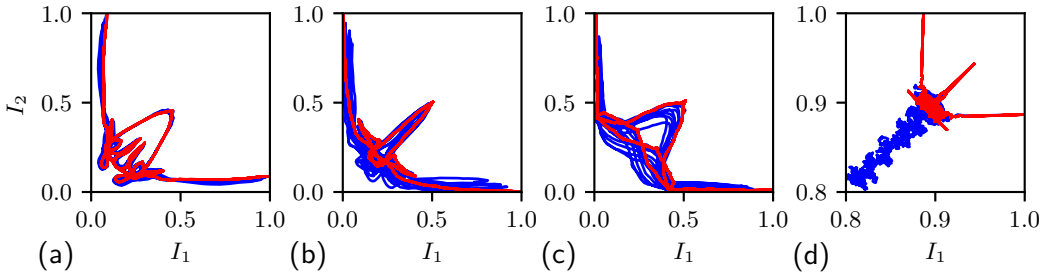

Figure 6.5: The trajectory of $\psi_{\boldsymbol{x}}$ projected on to I_1 and I_2 for several fundamental periods of $\psi_{\boldsymbol{x}}$ computed via the nonlinear system $\beta = 3$ (blue) and the linear system (red) for (a) $\varepsilon = 0.00071$, (b) $\varepsilon = 0.0084$, (c) $\varepsilon = 0.013$, and (d) $\varepsilon = 0.20$.

of KAM to NLS itself (see [40, 82]). Our results therefore suggest breather solutions supported on quasi-periodic KAM tori when a non-local derivative is included in the NLS. The breather solution breaks down at high nonlinearity due to the sufficiently strong perturbation to the KAM tori.

The current analysis of this breather solution clearly does not resolve all questions this chapter raises. One issue is that finite-time numerical simulations cannot be used as the rigorous proof for the existence of KAM tori (which must exist for infinite time). Therefore, our interpretation may need to be understood in terms of the Nekhoroshev theorem, which states existence for finite but very long times [27], and is known as the "physicists" KAM theorem. Another critical question is the stochastic emergence of these stable breather solutions. One possible interpretation is that they lie on some type of statistical "attractor" [54], such that a variety of initial conditions lead to the breather state. In addition, while the 2D breather we find here is for a derivative NLS not specific to a physical system, we remark that such equations are generally involved in the fields of nonlinear water waves, optics and others. For example, the breather recently found both experimentally and numerically in Bose-Einstein condensate [90] may bear a similar physical interpretation as we provide here.

6.4 Summary

In this chapter, we present results regarding a novel breather which spontaneously emerges from a 2D non-local derivative NLS. We show that the breather emerges at low nonlinearity with parameter β close to 3. A phase space analysis reveals that the trajectory associated with the breather solution is close to that of the linear system, but with aperiodicity introduced by the nonlinearity. The numerical findings support an explanation of the breather solution by KAM theory, in the sense that a trajectory with the breather solution of the linear system is deformed but preserved when a small nonlinearity is introduced.

CHAPTER 7

Discussion

Overall, this dissertation succeeds in developing a quantitative picture of WT in finite domains via numerical experiment. Our approach of generating high-resolution data, particularly in terms of resolution of statistical quantities, combined with the development of precise new numerical tools for the study of WT, reveals much about the physics of finite-size effects. In some cases, we are able to provide a quantitative dynamical view to the kinematic picture of finite-size effects that dominates the literature. This includes a new, interaction-based methods for the measurement of nonlinear broadening that emerges naturally from the dynamical equations for the energy cascade, without *a priori* assumptions regarding the role of nonlinear broadening in shaping the WT closure. This natural dependency of energy flux on the WT closure motivates our method for the evaluation of the closure function $f_P(\Omega)$, which provides a precise method for studying error of the WT closure in the DNS of bounded systems, while simultaneously shedding light on the physics WT closure itself by providing the form of $f(\Omega)$ measured from real data. We hope our methods are used widely for the study of the realization of the wave turbulence closure in finite domains, as we feel they still have much more to offer.

In other cases, we illuminate new physics, as is the case with wave turbulence on irrational tori. To our knowledge, these are the first numerical experiments of their kind. The DWT regime of our NLS-like model on the rational torus subverts the expectations of the traditional view of DWT (with γ=γ_0) due to the underlying Continuous Resonant System. Work by the mathematics and physics communities that draws connections between the Continuous Resonant System and the Wave Kinetic Equation may pave the way towards more quantitative and precise models of the DWT regime. We also demonstrate a novel breather solution that dominates finite domain dynamics at low nonlinearity, with a possible connection the KAM theory. The study of the KAM theorem in these high-dimensional systems is a relatively young field with many open questions, to which our numerical study hopefully can provide some insights. With respect to finite-size effects, we also provide evidence of the long hypothesized [49, 60] KAM tori that dominate stochastic dynamics in the DWT regime.

Our findings regarding the role of the Discrete Resonant Manifold in the DWT regime also indicate an avenue for improvement of the kinematic model for finite-size effects. We suggest a pseudo-quantitative extension of the kinematic model may be possible by comparing the structure of the Continuous Resonant Manifold of a given system to the corresponding Discrete Resonant Manifold and Discrete Quasi-resonant Manifolds of interest. Such a comparison may allow for better estimates of the "minimum" nonlinear broadening to observe the KWT regime, particularly over the traditional approach of making simple comparisons between frequency discreteness and nonlinear broadening without detailed consideration of the structure of the resonant manifold. This approach may have enhanced utility in the special case of systems where the Discrete Resonant Manifold's structure supports kinetic physics, as we have demonstrated.

Finally, we raise critical new questions that pave the way for an exciting future in wave turbulence research. In particular, our kinetic limit results on the 1D MMT system suggest that the WT closure holds for this system - in contrast to the alternative closure by MMT [61]. We suggest further study of the closure by comparison to the KZ spectrum, which may reveal convergence to the KZ spectrum over a finite-width inertial range. On the other hand, such a study could reveal a discrepancy that might be linked to one of the many reasons for the breakdown of the KZ spectrum via further study of non-locality and instability within the MMT model. Research in this direction may finally settle the debate as to the cause of MMT's original findings nearly three decades ago. Our study of the Gaussian energy flux distribution and Log-normal dissipation rate fits nicely into the broader trend of viewing WT via probabilistic formulations and higher-order statistical quantities, while raising questions on the role of the multiplicative random processes in shaping dissipation range dynamics. Further, recent theoretical developments [30, 23] are moving towards descriptions of WT that can incorporate intermittency into the WT formalism, in which case precise measurements of high-order statistics from numerical data will be key validation. We hope to have demonstrated how this might be done in a reliable and robust way, with our flux decomposition and WT closure study as examples. We have also demonstrated the utility in using large data sets to study WT - which also enables data-driven modeling of the WT closure. Flow turbulence has enjoyed much success in this direction, and the WT community would benefit from approaches that make the most of its data sets. We present in this dissertation powerful physics-based approaches, and speculate that using physics-informed data-driven models, perhaps inspired by the developments in this dissertation, may lead to even further discoveries on the fundamental physics of wave turbulence.

APPENDIX A

Numerical Method for Computing the Kolmogorov Constant

We are interested in integrating (2.49), provided again below for convenience:

$$S = \lim_{y\to 1} \frac{dI(y)}{dy} = \int_0^1 \int_0^1 \int_0^1 (\xi_1\xi_2\xi_3)^{-1} \left(1 + \xi_3^2 - \xi_1^2 - \xi_2^2\right) \tag{A.1}$$
$$\times(\xi_3 \ln \xi_3 - \xi_1 \ln \xi_1 - \xi_2 \ln \xi_2)\delta(\xi_1 + \xi_2 - \xi_3 - 1)\delta(\xi_1^2 + \xi_2^2 + \xi_3^2 - 1)d\xi_1 d\xi_2 d\xi_3,$$

As remarked in Section 2.4, the delta functions express the quartet and resonance conditions, which represent the intersection of the plane $\xi_1 + \xi_2 - \xi_3 - 1 = 0$ and the sphere $\xi_1^2 + \xi_2^2 + \xi_3^2 = 1$. While there is a temptation to take the geometric approach and simply parameterize over this manifold to compute S as a line integral, one must be careful to avoid parameterizations that lead to singularities in the integrand, as we require a precise numerical evaluation. Also, just like the WKE, the Kolmogorov constant requires notoriously precise bookkeeping to avoid missing factors. To ensure our bookkeeping is careful, we will solve this in a more algebraic way, relying heavily on properties of the Dirac delta function. For simplicity, we will refer the non-delta part of the integrand by $f(\xi_1, \xi_2, \xi_3)$ so that

$$f(\xi_1, \xi_2, \xi_3) \equiv (\xi_1\xi_2\xi_3)^{-1} \left(1 + \xi_3^2 - \xi_1^2 - \xi_2^2\right) (\xi_3 \ln \xi_3 - \xi_1 \ln \xi_1 - \xi_2 \ln \xi_2). \tag{A.2}$$

This leaves

$$S = \int_0^1 \int_0^1 \int_0^1 f(\xi_1, \xi_2, \xi_3)\delta(\xi_1 + \xi_2 - \xi_3 - 1)\delta(\xi_1^2 + \xi_2^2 + \xi_3^2 - 1)d\xi_1 d\xi_2 d\xi_3. \tag{A.3}$$

The first of these delta functions is linear in ξ_1. Making use of the property

$$\int_0^1 g(x)\delta(x-a)dx = g(a) \text{ for } 0 \leq a \leq 1, \tag{A.4}$$

we can integrate over ξ_3 to obtain

$$S = \iint_{\Delta(\xi_1,\xi_2)} f(\xi_1, \xi_2, \xi_1 + \xi_2 - 1)\delta\left(\xi_1^2 + \xi_2^2 + (\xi_1 + \xi_2 - 1)^2 - 1\right) d\xi_1 d\xi_2. \tag{A.5}$$

Integrating over the region $\Delta(\xi_1, \xi_2) \equiv \{0 < \xi_1 < 1, 0 < \xi_2 < 1, 1 < \xi_1 + \xi_2 < 2\}$ simply ensures $0 < \xi_3 < 1$. We would like to now apply (A.4) again, however in order to do this, we require a transformation so that the argument $\xi_1^2 + \xi_2^2 + \xi_3^2 - 1$ is of the required form. To do this, we transform the inner integral to one with respect to du, where $u = \xi_1^2 + \xi_2^2 + (\xi_1 + \xi_2 - 1)^2 - 1$ and $du = 2(2\xi_1 + \xi_2 - 1)d\xi_1$. This leaves

$$S = \iint_{\Delta(u,\xi_2)} \frac{f(\xi_1(u), \xi_2, \xi_1(u) + \xi_2 - 1)}{2(2\xi_1(u) + \xi_2 - 1)} \delta(u)\, du d\xi_2. \tag{A.6}$$

Now, we may apply (A.4), being careful to include only the part of $u(\xi_1, \xi_2) = 0$ that lies in $\Delta(\xi_1, \xi_2)$. After some manipulation of our definition of u we find that, of the two branches for which $u = 0$, the one with

$$\xi_1 = \frac{1 - \xi_2 + \sqrt{(1 - \xi_2)(3\xi_2 + 1)}}{2}, \quad 0 < \xi_2 < 1 \tag{A.7}$$

is in the region $\Delta(\xi_1, \xi_2)$. After applying (A.4),

$$S = \int_0^1 \frac{f(\xi_1(\xi_2), \xi_2, \xi_3(\xi_2))}{2\sqrt{(1 - \xi_2)(3\xi_2 + 1)}} d\xi_2. \tag{A.8}$$

This form of S is suitable for numerical integration, where the integrand as $\xi_2 \to 1$ (from below) can be shown to approach zero via L'Hospital's rule.

APPENDIX B

Supplemental Analysis on the Discrete Resonant Manifold

In this Appendix, we provide:

1. formulation of the *continuous resonant* system
2. the configurations of the resonant quartets on $\mathbb{T}^2_r$ and $\mathbb{T}^2_{ir}$, including a range of q and their effects on the spectral slopes
3. quantification of nonlinear frequency broadening and visualization of the discrete quasi-resonant manifold (quasi-DRM)

B.1 Continuous Resonant System

For the nonlinear Schrödinger equation $-i\partial_t\psi_x + \Delta\psi_x = \epsilon^2|\psi_x|^2\psi_x$ on $\mathbb{T}^2_L$ of size L^2, a theorem is proven in [35] that in weakly nonlinear large box limit, a *continuous resonant* equation holds

$$-i\frac{\partial\tilde{a}_{\boldsymbol{k}}}{\partial t} = \frac{2\epsilon^2\log L}{\zeta(2)L^2}\int \tilde{a}_{\boldsymbol{k}_1}\tilde{a}_{\boldsymbol{k}_2}\tilde{a}^*_{\boldsymbol{k}_3}\delta\left(\boldsymbol{k}_1+\boldsymbol{k}_2-\boldsymbol{k}_3-\boldsymbol{k}\right)\delta\left(\omega_{\boldsymbol{k}_1}+\omega_{\boldsymbol{k}_2}-\omega_{\boldsymbol{k}_3}-\omega_{\boldsymbol{k}}\right)d\boldsymbol{k}_1 d\boldsymbol{k}_2 d\boldsymbol{k}_3, \tag{B.1}$$

where ζ is the Riemann zeta function, $\tilde{a}_{\boldsymbol{k}} = e^{-ik^2t}\hat{a}_{\boldsymbol{k}}$, and $a(\boldsymbol{x}) = L^{-2}\sum_{k\in\mathbb{Z}^2_L}\hat{a}_{\boldsymbol{k}}exp(2\pi i\boldsymbol{k}\cdot\boldsymbol{x})$ with $\mathbb{Z}^2_L \equiv (L^{-1}\mathbb{Z})^2$ (note that this Fourier transform is different in normalization from that in Chapter 2, but is consistent with [35]).

Two important components in the derivation of (B.1) require further clarification: First, the weak nonlinearity limit is taken to eliminate the contribution of quasi-resonant interactions, so only resonant interactions are involved in (B.1). Note that this differs from the kinetic limit used in WTT. This is observed in our numerical results and mathematically achieved by the normal form transformation. Second, the large box limit is taken such that the summation over $S_{\Omega=0}$ can be

considered to be like a Riemann sum which is related to the continuous integration in (B.1). For this purpose, the key equation established through number theory reads

$$\sum_{\substack{\boldsymbol{k}_1,\boldsymbol{k}_2,\boldsymbol{k}_3\in\mathbb{Z}_L^2\\(\boldsymbol{k}_1,\boldsymbol{k}_2,\boldsymbol{k}_3)\in S_{\Omega=0}}} \hat{a}_{\boldsymbol{k}_1}\hat{a}_{\boldsymbol{k}_2}\hat{a}^*_{\boldsymbol{k}_3} \sim \frac{2L^2\log L}{\zeta(2)} \int_{\substack{\boldsymbol{k}_1,\boldsymbol{k}_2,\boldsymbol{k}_3\in\mathbb{R}^2\\(\boldsymbol{k}_1,\boldsymbol{k}_2,\boldsymbol{k}_3)\in S_{\Omega=0}}} \hat{a}_{\boldsymbol{k}_1}\hat{a}_{\boldsymbol{k}_2}\hat{a}^*_{\boldsymbol{k}_3} d\boldsymbol{k}_1 d\boldsymbol{k}_2 d\boldsymbol{k}_3. \tag{B.2}$$

An alternative way to take the large box limit is to consider $k \to \infty$ for a given L [35]. Therefore, equation (B.2) can be reformulated for our configuration (changing from $\mathbb{Z}_L^2$ to $\mathbb{Z}_r^2$ and setting $\hat{a}_{\boldsymbol{k}} = k\hat{\psi}_{\boldsymbol{k}}$), leading to

$$\sum_{\substack{\boldsymbol{k}_1,\boldsymbol{k}_2,\boldsymbol{k}_3\in\mathbb{Z}_r^2\\(\boldsymbol{k}_1,\boldsymbol{k}_2,\boldsymbol{k}_3)\in S_{\Omega=0}}} k_1k_2k_3\hat{\psi}_{\boldsymbol{k}_1}\hat{\psi}_{\boldsymbol{k}_2}\hat{\psi}^*_{\boldsymbol{k}_3} \sim \int_{\substack{\boldsymbol{k}_1,\boldsymbol{k}_2,\boldsymbol{k}_3\in\mathbb{R}^2\\(\boldsymbol{k}_1,\boldsymbol{k}_2,\boldsymbol{k}_3)\in S_{\Omega=0}}} k_1k_2k_3\hat{\psi}_{\boldsymbol{k}_1}\hat{\psi}_{\boldsymbol{k}_2}\hat{\psi}^*_{\boldsymbol{k}_3} d\boldsymbol{k}_1 d\boldsymbol{k}_2 d\boldsymbol{k}_3, \tag{B.3}$$

where we have omitted the prefactor (the treatment of which will involve more subtlety and is not necessary for the purpose of this work). Equation (B.3) can then be used to replace the summation over $S_{\Omega=0}$ on $\mathbb{T}_r^2$ in (2.55) with $\Omega = 0$ into an integral. Under low nonlinearity, we arrive at

$$\frac{\partial n_{\boldsymbol{k}}}{\partial t} = \left.\frac{\partial n_{\boldsymbol{k}}}{\partial t}\right|_{\Omega=0} \sim \int_{\substack{\boldsymbol{k}_1,\boldsymbol{k}_2,\boldsymbol{k}_3\in\mathbb{R}^2\\(\boldsymbol{k}_1,\boldsymbol{k}_2,\boldsymbol{k}_3)\in S_{\Omega=0}}} 2kk_1k_2k_3\mathrm{Im}\langle\hat{\psi}^*_{\boldsymbol{k}}\hat{\psi}_{\boldsymbol{k}_1}\hat{\psi}_{\boldsymbol{k}_2}\hat{\psi}^*_{\boldsymbol{k}_3}\rangle d\boldsymbol{k}_1 d\boldsymbol{k}_2 d\boldsymbol{k}_3, \text{ on } \mathbb{T}_r^2. \tag{B.4}$$

B.2 Resonant Quartets on $\mathbb{T}_r^2$ and $\mathbb{T}_{ir}^2$

We consider the exact resonance condition for a quartet:

$$\begin{aligned} \boldsymbol{k}_1 + \boldsymbol{k}_2 - \boldsymbol{k}_3 - \boldsymbol{k} &= 0, \\ \omega_{\boldsymbol{k}_1} + \omega_{\boldsymbol{k}_2} - \omega_{\boldsymbol{k}_3} - \omega_{\boldsymbol{k}} &= 0, \end{aligned} \tag{B.5}$$

with dispersion relation $\omega_{\boldsymbol{k}} = |\boldsymbol{k}|^2$. For discrete wave number $\boldsymbol{k} = (n, qm)$ with $m, n \in \mathbb{Z}$ on $\mathbb{T}_r^2$ ($q = 1$) and $\mathbb{T}_{ir}^2$ ($q^2 = \sqrt{2}$), the resonance condition (B.5) can be expanded as

$$n_1 + n_2 - n_3 - n = 0 \tag{B.6}$$

$$m_1 + m_2 - m_3 - m = 0 \tag{B.7}$$

$$n_1^2 + n_2^2 - n_3^2 - n^2 = -q^2\left(m_1^2 + m_2^2 - m_3^2 - m^2\right) \tag{B.8}$$

Substituting (B.6) and (B.7) into (B.8) yields

$$(n_1 - n)(n_2 - n) = -q^2(m_1 - m)(m_2 - m) \tag{B.9}$$

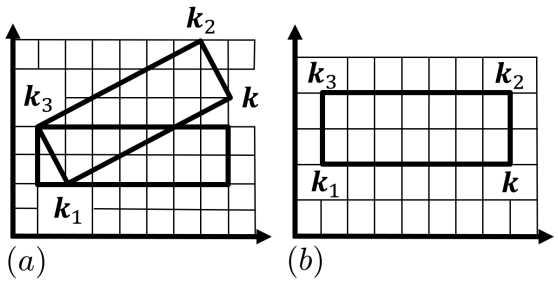

Figure B.1: Sketches of the quadrilaterals formed by vertices $\boldsymbol{k}$, $\boldsymbol{k}_1$, $\boldsymbol{k}_2$ and $\boldsymbol{k}_3$ on (a) $\mathbb{T}^2_r$ and (b) $\mathbb{T}^2_{ir}$.

For $\mathbb{T}^2_r$ ($q = 1$), (B.9) is reduced to $(\boldsymbol{k}_1 - \boldsymbol{k}) \cdot (\boldsymbol{k}_2 - \boldsymbol{k}) = 0$, i.e., $(\boldsymbol{k}_1 - \boldsymbol{k}) \perp (\boldsymbol{k}_2 - \boldsymbol{k})$. Combined with (B.6) and (B.7), it can be understood that the four vertices represented by $\boldsymbol{k}$, $\boldsymbol{k}_1$, $\boldsymbol{k}_2$ and $\boldsymbol{k}_3$ form a quadrilateral with arbitrary orientations allowed on the discrete wave number grid (Figure B.1(a)). For $\mathbb{T}^2_{ir}$ ($q^2 = \sqrt{2}$), (B.9) holds only if LHS=RHS=0, i.e., $n \in \{n_1, n_2\}$ and $m \in \{m_1, m_2\}$. Therefore, the four vertices $\boldsymbol{k}$, $\boldsymbol{k}_1$, $\boldsymbol{k}_2$ and $\boldsymbol{k}_3$ form a quadrilateral with only horizontal/vertical orientations allowed, i.e., aligned with the axes in Figure B.1(b).

We further provide a quantitative study on the effect of q to the number of exact resonances (i.e., the sparsity/density of resonances on the DRM). For $\boldsymbol{k}, \boldsymbol{k}_1, \boldsymbol{k}_2, \boldsymbol{k}_3 \in ([-M, M], q[-M, M])$ with $M = 85$, we plot in Figure B.2(a) the cardinality $|S_{\Omega=0}|$, i.e., number of elements in $S_{\Omega=0}$, for $q^4 \in \{n | n \in \mathbb{Z}, 1 \le n \le 16\}$. We see that when q^2 is irrational (red points), $|S_{\Omega=0}|$ is minimized due to the reason associated with Figure B.1. For rational q^2, $|S_{\Omega=0}|$ is significantly larger with the maximum attained at $q = 1$ (in the test range). This can be understood in terms of the number of solutions of (B.9) which is reduced due to the constrain in the prime factors introduced by $q \neq 1$. Therefore, our choices of $q^2 = \sqrt{2}$ and $q = 1$ are the two extremes in terms of $|S_{\Omega=0}|$.

The spectral slopes for four selected values of q are shown in Figure B.2(b). These include the existing two cases of $q^2 = \sqrt{2}$ and $q = 1$, with additional two cases of $q = \sqrt{2}$ and $q = 2$. It can be seen that the case with $q^2 = \sqrt{2}$ leads to the largest deviation of γ to the WTT solution γ_0. Among the other three values of q, $\gamma(q = 1)$ is closest to γ_0, consistent with the largest number of exact resonances. However, $\gamma(q = 2)$ is slightly closer to γ_0 than $\gamma(q = \sqrt{2})$ even though considerably more resonances are identified for the case with $q = \sqrt{2}$. This suggests that the "sparsity" of the DRM is not the only factor to consider for the DWT dynamics, but that the distribution of the resonances also plays a role. A criterion to measure the "closeness" of the DWT dynamics to WTT

may be established through the *continuous resonant* equation, which is only proved for the $q = 1$ case. The discrete wave numbers of $q = 1$ align periodically with those in $q = 2$, but never overlap with those in $q = \sqrt{2}$. This may lead to the spectral slope γ for $q = 2$ being closer to γ_0 even though fewer exact resonances are present than in the case of $q = \sqrt{2}$. The argument may be generalized to the comparison between (a) rational q and (b) irrational q but rational q^2 in the large wave number limit, but more theoretical and numerical studies are required.

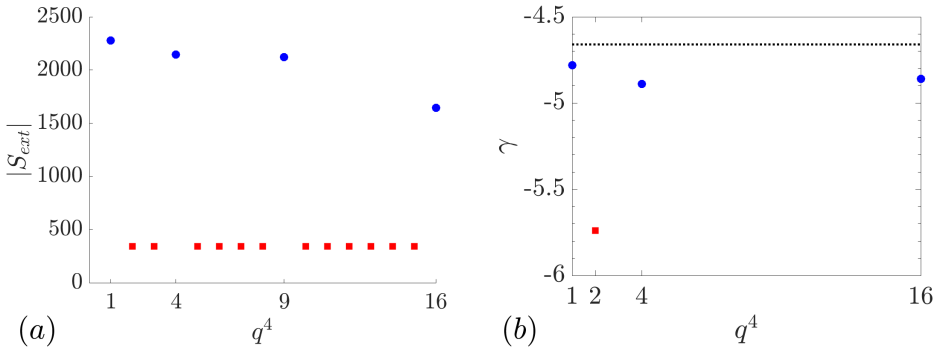

Figure B.2: (a) $|S_{\Omega=0}|$ computed for rational (•) and irrational (▪) q^2, with $\boldsymbol{k}_2 = (-36, 31q)$ and $k_{3x} = -22$ as considered in Chapter 3. (b) Spectral slope γ computed using ν_{opt} with $N = 1024^2$ modes for rational (•) and irrational (▪) q^2. The WTT analytical solution $\gamma_0 = -14/3$ is indicated $(\cdot\ \cdot\ \cdot)$.

B.3 $k - \omega$ spectral analysis and quasi-DRM visualization

We plot the (angle-averaged) $k - \omega$ spectra $E(k, \omega)$ on $\mathbb{T}^2_r$ and $\mathbb{T}^2_{ir}$ for $\epsilon = 3.00 \times 10^{-2}$ and $\epsilon = 3.00 \times 10^{-4}$ in Figure B.3. We confirm that the majority of the energy is concentrated near the linear dispersion relation $\omega = k^2$ for all the cases. While some bound wave components exist at higher nonlinearity level, they are insignificant for lower nonlinearity level (and similar on $\mathbb{T}^2_r$ and $\mathbb{T}^2_{ir}$). Therefore, bound waves cannot be used to interpret the spectral slope difference between $\mathbb{T}^2_r$ and $\mathbb{T}^2_{ir}$. The nonlinear frequency broadening Γ can be estimated for all cases by taking the width of $E(k, \omega)$ around $\omega = k^2$ at $k = 25$ in the inertial range (without loss of generality). Measuring the width by covering up to the 50% of the maximum value [6], we obtain the nonlinear frequency broadening $\Gamma \approx 10$ and $\Gamma \approx 1$ for higher and lower nonlinearity levels on both $\mathbb{T}^2_r$ and $\mathbb{T}^2_{ir}$, respectively.

We define the quasi-DRM(Γ) as the set $S_{\Omega<\Gamma} \setminus S_{\Omega=0}$, where $S_{\Omega<\Gamma} \equiv \{(\boldsymbol{k}_1, \boldsymbol{k}_2, \boldsymbol{k}_3) | \boldsymbol{k}_1 + \boldsymbol{k}_2 - \boldsymbol{k}_3 - \boldsymbol{k} = 0,\ |\omega_{\boldsymbol{k}_1} + \omega_{\boldsymbol{k}_2} - \omega_{\boldsymbol{k}_3} - \omega_{\boldsymbol{k}}| < \Gamma\}$. By setting $\boldsymbol{k}_2 = (-36, 31q)$ and $k_{3x} = -22$, Figure B.4 shows the quasi-DRM(Γ) on both $\mathbb{T}^2_r$ and $\mathbb{T}^2_{ir}$. On $\mathbb{T}^2_r$, we find an empty set for the lower nonlinearity level, indicating the dominance of exact resonance, in contrast to the quasi-DRM at higher nonlinearity

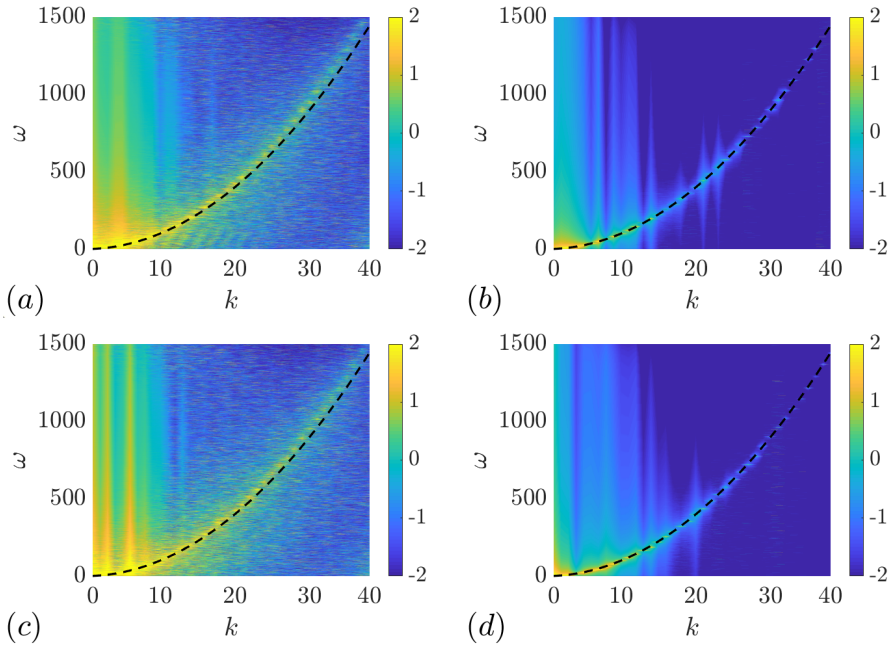

Figure B.3: $\omega - k$ spectra on $\mathbb{T}^2_r$ for (a) $\epsilon = 3 \times 10^{-2}$ and (b) $\epsilon = 3 \times 10^{-4}$, and on $\mathbb{T}^2_{ir}$ for (c) $\epsilon = 3 \times 10^{-2}$ and (d) $\epsilon = 3 \times 10^{-4}$. The dispersion relation $\omega = k^2$ is indicated $(- - -)$.

level which provides a considerable portion of P. On $\mathbb{T}^2_{ir}$, the quasi-DRM at higher nonlinearity is significantly "denser" than that at lower nonlinearity, resulting in the variation of spectral slope and energy cascade with ϵ observed in Chapter 3.

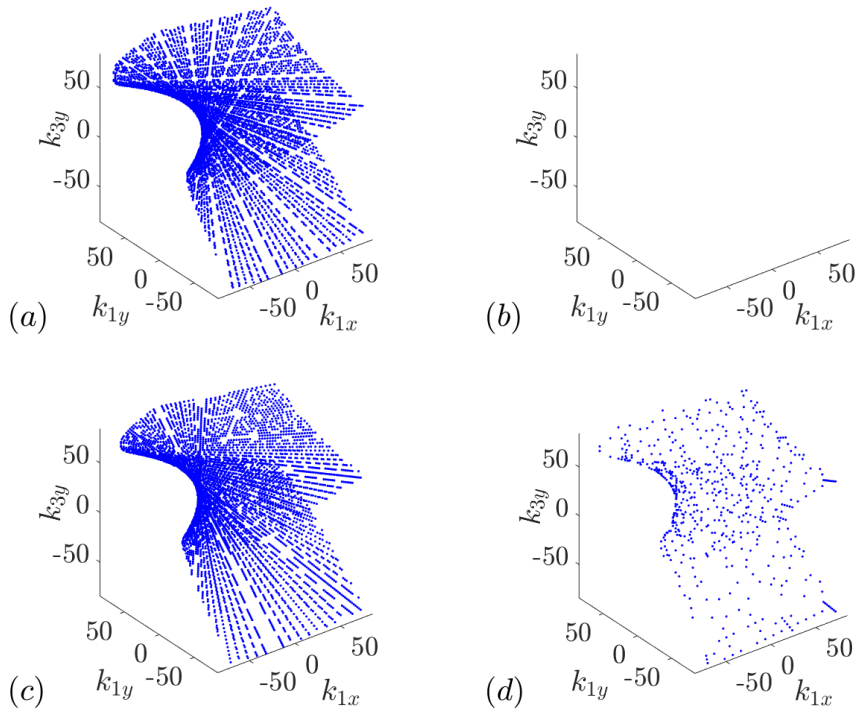

Figure B.4: $S_{\Omega<\Gamma} \setminus S_{\Omega=0}$ on $\mathbb{T}^2_r$ for (a) $\Gamma = 10$ and (b) $\Gamma = 1$, and on $\mathbb{T}^2_{ir}$ for (c) $\Gamma = 10$ and (d) $\Gamma = 1$.

APPENDIX C

Supplemental Analysis on the Breather Solution

C.1 Breather solutions in other situations

In Chapter 6, we restrict our focus to a two-dimensional (2D), defocusing Majda-McLaughlin-Tabak (MMT) model without forcing or dissipation. In this section, we show the occurrence of the breather in additional contexts: the MMT model with a focusing nonlinearity, as well as a defocusing forced-dissipated model.

We begin with the focusing MMT model, given by $\lambda = -1$. The parameter λ is well-known to control the modulational instability of the Nonlinear Schrödinger Equation (NLS) as well as the MMT model. In the context of the MMT model, the sign of λ has been shown to affect the emergence of coherent structures in a one-dimensional MMT model with dispersion relation $\omega = k^{1/2}$ [87]. In our results, however, we find no significant change in the breather behavior between the focusing/defocusing equations, suggesting (along with the fact that the breather exists only at *weak* nonlinearity) that modulational instability is not responsible for our breather. In Figure C.1a/c, we show 5 fundamental periods T_f of H and its components H_2 and H_4 in a fully-developed breather state for the focusing equation with $\beta = 2$. These results were obtained with an identical numerical setup to that of Chapter 6, and the presented results occur at low nonlinearity. The pattern of the oscillating breather is also similar to that in the defocusing case.

Next, we present results obtained for the forced-dissipated system presented in Chapter 4, however with $\beta = 2$. For this test, we use a larger domain of 512×512 modes. In Figure C.1b, H and its two components are plotted for $5T_f$ in the breather state. In this case, we do not expect the total Hamiltonian to be conserved, but rather to be quasi-steady for the fully developed system. Nevertheless, the signature of the breather is clearly present. Just as in the unforced case, we find that the wave action spectrum of the system is altered when the breather is present. In Figure C.2, we provide the fully developed spectra of the forced-dissipated system for several different orders of nonlinearity. When the nonlinearity is low and the breather is present, we again see departure from a power-law spectrum, with a steeper tail region. When nonlinearity is raised, we observe the

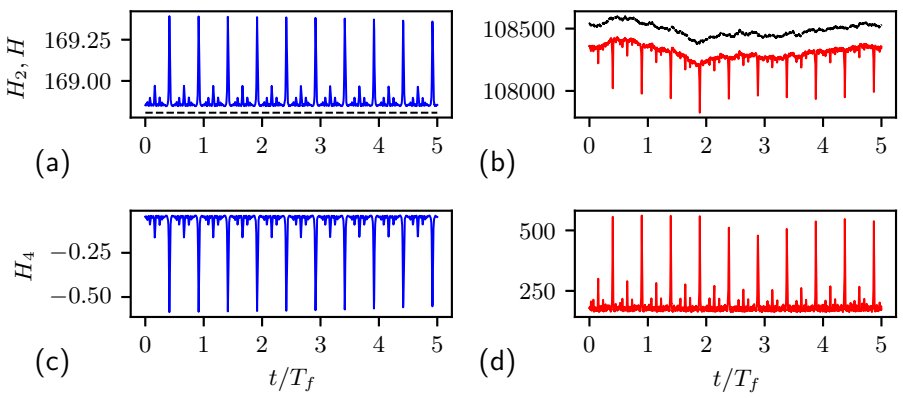

Figure C.1: $5T_f$ of the time series of H (dashed) and H_2 (solid) for a fully-developed breather solution to the (a) focusing MMT equation with $\beta = 3$ and (b) forced-dissipated MMT equation with $\beta = 2$. The corresponding H_4 for (c) the focusing system and (d) the forced-dissipated system are also provided. The focusing system has $\varepsilon = 0.00028$ and the forced-dissipated system has $\varepsilon = 0.0016$.

the spectra of wave turbulence are restored (and an associated forward energy cascade develops).

C.2 secondary peaks in the breather cycle

We include in this section plots of the secondary peaks of $|\psi|$ in the breather cycle, supplementing Figure 2 in Chapter 6. We choose $|\psi|$ rather than $\mathrm{Re}[\psi]$ (as in Chapter 6) to better resolve the smaller amplitudes of these secondary structures. While the largest peaks in H_4 (Fig. C.3e) correspond to single peaks in $|\psi|$, the secondary peaks in H_4 correspond to grids of smaller peaks in $|\psi|$ (Fig. C.3a/b/c/d).

C.3 Numerical Validation of the Breather

In this section, we provide analyses and numerical tests that rule out the possibility that the breather we discuss is a numerical artifact. In particular, we show that the breather solution is consistent under

1. the change of integration scheme to a symplectic integrator.
2. the change of our dealiasing procedure.
3. an increase in the number of Fourier modes (spatial resolution).

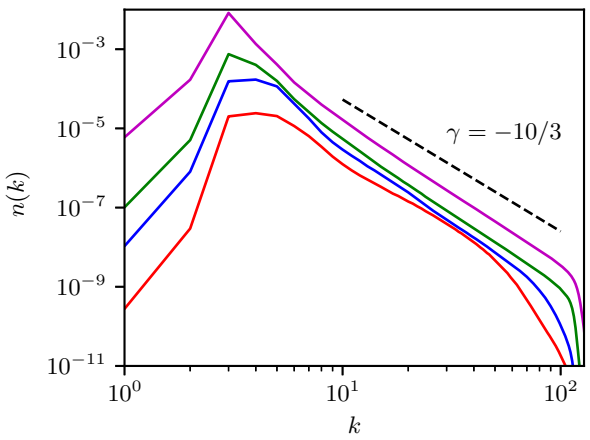

Figure C.2: The fully-developed, angle-averaged wave action spectra at a few nonlinearity levels of the forced-dissipated system, with the Kolmogorov-Zakharov spectral slope of $\gamma = -10/3$ indicated (dashed).

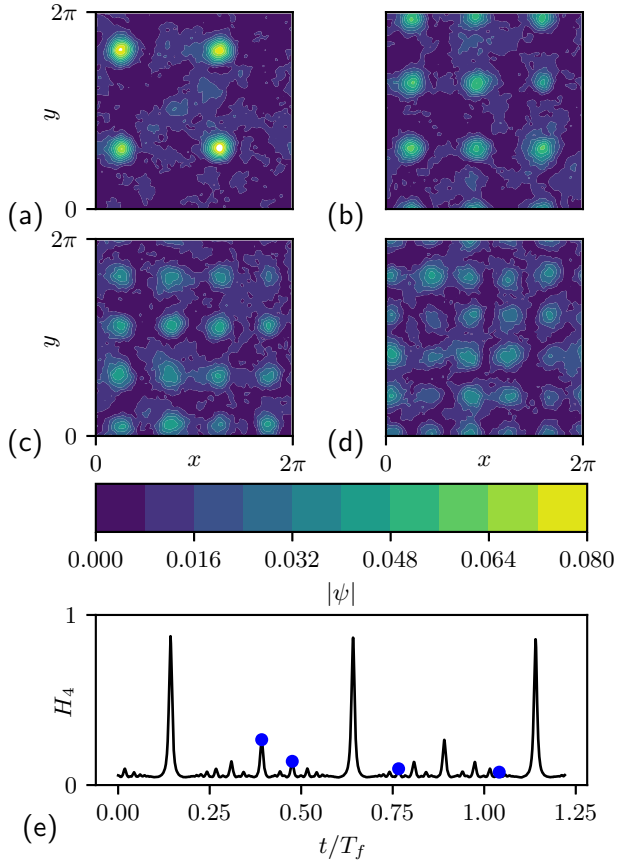

Figure C.3: Contour plots of $|\psi|$ at $\beta = 3$ for $\varepsilon = 0.00071$ at various stages of the cycle of the breather (a/b/c/d), corresponding chronologically to the times marked by the blue circles in (e) the time series of H_4.

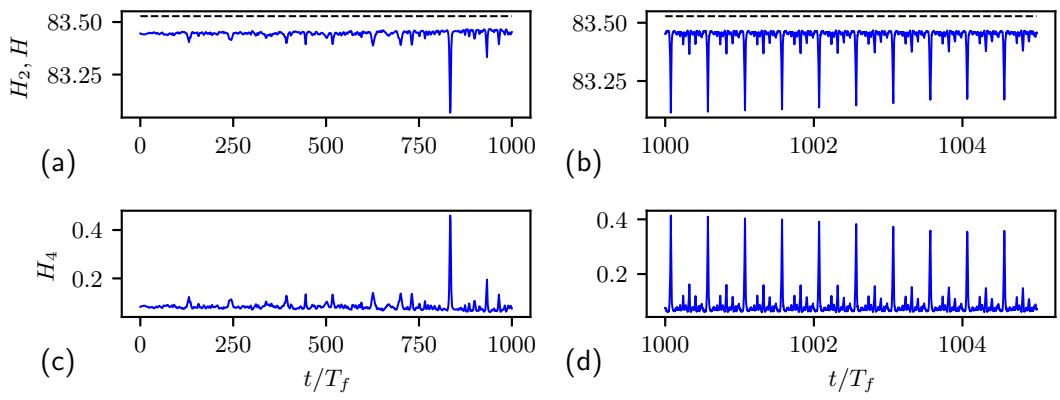

Figure C.4: The time series of (a) H (dashed) and H_2 (solid) starting from $t = 0$ for the defocusing MMT equation with $\beta = 3$ under symplectic integration, with the corresponding time series of (c) H_4. A detailed view beginning at $t = 1000T_f$ of (b) H, H_2 and (d) H_4 over $5T_f$.

We begin with point 1. Symplectic integration of a Hamiltonian system preserves the phase space geometry of its solution. Specifically, under Hamiltonian flow, structures such as sinks and limit cycles are forbidden by Liouville's theorem. When using an integrator such as an explicit 4th-order Runge-Kutta scheme (RK4), however, these structures can be erroneously introduced into the solution, which may change the dynamics. To ensure our breather is not an artifact introduced by non-symplectic integration, we implement a simple symplectic integrator, the implicit midpoint method (IMP) [91], to verify that we still obtain (and preserve) the breather solution. In the IMP method, we solve the implicit nonlinear problem via fixed-point iteration. For an identical numerical setup to that of Chapter 6, we allow the system to freely evolve under the IMP integration scheme. We set $\beta = 3$ and simulate at the low nonlinearity of $\varepsilon = 0.001$.

We provide in Figure C.4a the evolution of H and H_2 from $t = 0$, with H very well conserved and H_2 indicating that the breather has already formed by $t = 1000T_f$. The corresponding plot of H_4 is provided in C.4c. Just as in Chapter 6, these plots of the initial evolution have a low sampling rate, leading to aliasing. To confirm that the breather has the same signature in H_2 and H_4 as in the case of non-symplectic integration, high-sampling rate plots of H, H_2 (Fig. C.4b) and H_4 (Fig. C.4d) are also provided over $5T_f$, showing no difference to those results of Chapter 6. Thus, the breather is not an artifact of non-symplectic integration.

Next, we address point 2. In order to prevent the aliasing of modes due to the cubic nonlinearity of the MMT model, a standard $1/2$ dealiasing rule is applied after each product during the evaluation of the nonlinear term. The $1/2$ dealiasing rule is typically implemented via zero-padding the truncated wave number domain: if k_m is the maximum resolved wave number in our simulation (that is oriented along the x and y axes), then, in each direction, zero-padding is included such that for a computation domain of size $[-2k_m, 2k_m]^2$, the non-zero (resolved) Fourier modes are only

contained in the box $[-k_m, k_m]^2$. The zero-padding is enforced by setting all modes outside the box $[-k_m, k_m]^2$ to zero after each product is taken.

This procedure, however, has the effect of subtly changing the evolution of the system. In order to be assured that the breather is not an artifact of our dealiasing scheme, we first show that our dealiasing leads to a slightly modified Hamiltonian system (analytically), then we show that the breather is preserved in the original system without modification. We start by writing down the truncated Hamiltonian that we aim to numerically simulate:

$$H = \sum_{\substack{\boldsymbol{k} \\ |\boldsymbol{k}|_\infty \in [-k_m, k_m]}} k^2 \hat{\psi}_{\boldsymbol{k}} \hat{\psi}^*_{\boldsymbol{k}} + \frac{1}{2}\lambda \sum_{\substack{\boldsymbol{k_1}, \boldsymbol{k_2}, \boldsymbol{k_3}, \boldsymbol{k} \\ \boldsymbol{k_1} + \boldsymbol{k_2} = \boldsymbol{k_3} + \boldsymbol{k} \\ |\boldsymbol{k_i}|_\infty \in [-k_m, k_m]}} (k_1 k_2 k_3 k_4)^{\beta/4} \hat{\psi}_{\boldsymbol{k1}} \hat{\psi}_{\boldsymbol{k2}} \hat{\psi}^*_{\boldsymbol{k3}} \hat{\psi}^*_{\boldsymbol{k}}, \tag{C.1}$$

where the summation is over every permutation over the subscript wave numbers. When computing the nonlinear term, we evaluate (via the Fourier transform)

$$(\psi_{\boldsymbol{x}} \psi^*_{\boldsymbol{x}}) \psi_{\boldsymbol{x}} = \left(\sum_{\substack{\boldsymbol{k_1}, \boldsymbol{k_3} \\ |\boldsymbol{k_i}|_\infty \in [-k_m, k_m] \\ |\boldsymbol{k_1} - \boldsymbol{k_3}|_\infty \in [-k_m, k_m]}} \hat{\psi}_{\boldsymbol{k1}} \hat{\psi}^*_{\boldsymbol{k3}} e^{i(\boldsymbol{k1} - \boldsymbol{k3}) \cdot \boldsymbol{x}} \right) \times \sum_{\substack{\boldsymbol{k_2} \\ |\boldsymbol{k_2}|_\infty \in [-k_m, k_m]}} \hat{\psi}_{\boldsymbol{k2}} e^{i \boldsymbol{k2} \cdot \boldsymbol{x}} \tag{C.2}$$

where the derivatives have been neglected for clarity ($\beta = 0$). The second condition under the first sum (red) is the first dealiasing step, where any product of modes that is mapped outside the bounded computational domain is excluded from the sum. The effect of dealiasing is therefore to remove certain interactions from the original system. It is not hard to show that including this extra condition modifies the Hamiltonian such that

$$H' = \sum_{\substack{\boldsymbol{k} \\ |\boldsymbol{k}|_\infty \in [-k_m, k_m]}} k^2 \hat{\psi}_{\boldsymbol{k}} \hat{\psi}^*_{\boldsymbol{k}} + \frac{1}{2}\lambda \sum_{\substack{\boldsymbol{k_1}, \boldsymbol{k_2}, \boldsymbol{k_3}, \boldsymbol{k} \\ \boldsymbol{k_1} + \boldsymbol{k_2} = \boldsymbol{k_3} + \boldsymbol{k} \\ |\boldsymbol{k_i}|_\infty \in [-k_m, k_m] \\ |\boldsymbol{k_1} - \boldsymbol{k_3}|_\infty \in [-k_m, k_m]}} (k_1 k_2 k_3 k_4)^{\beta/4} \hat{\psi}_{\boldsymbol{k1}} \hat{\psi}_{\boldsymbol{k2}} \hat{\psi}^*_{\boldsymbol{k3}} \hat{\psi}^*_{\boldsymbol{k}}, \tag{C.3}$$

where H' represents the effective Hamiltonian when dealiasing is used. While a second dealiasing step is included after the second product is taken in (C.2), no additional interactions are removed from H' by the second dealiasing step: $|\boldsymbol{k}_1 + \boldsymbol{k}_2 - \boldsymbol{k}_3|_\infty \in [-k_m, k_m]$ is accounted for by the fact that we already require $\boldsymbol{k}_1 + \boldsymbol{k}_2 - \boldsymbol{k}_3 = \boldsymbol{k}$ and $|\boldsymbol{k}|_\infty \in [-k_m, k_m]$. We remark that it is not *a priori* clear that the dealiased system is still Hamiltonian, but this fact is discovered when one attempts to write H'.

In order to show that the system evolution according to (C.1) also leads to the breather solution,

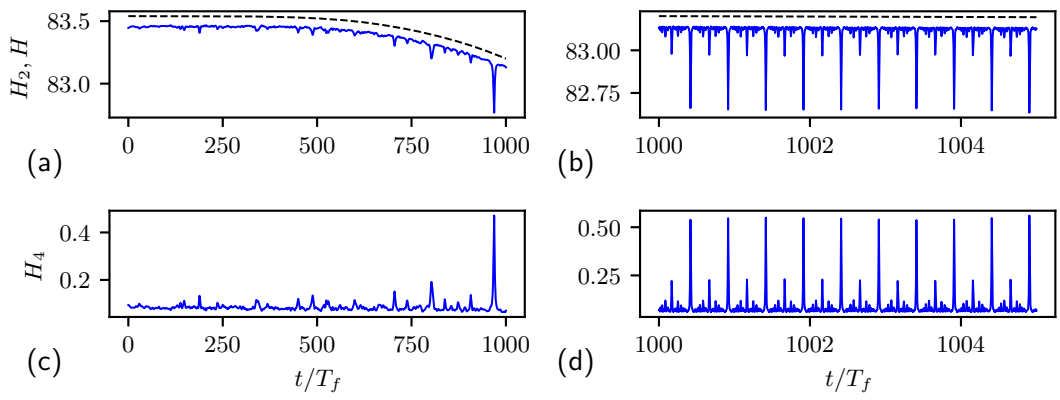

Figure C.5: The time series of (a) H (dashed) and H_2 (solid) starting from $t = 0$ for the defocusing MMT equation with $\beta = 3$ using a scheme that avoids the dealiasing step, with the corresponding time series of (c) H_4. A detailed view beginning at $t = 1000T_f$ of (b) H, H_2 and (d) H_4 over $5T_f$.

we perform a different dealiasing scheme for the simulation. Specifically, we skip the dealiasing step in the intermediate stage of computing the cubic term, and only dealias once after cubic multiplication is completed. Since this dealiasing step is equivalent to keeping only the Fourier modes up to k_m, this strategy produces evolution consistent with the system given by H (rather than H'). We use this scheme in an otherwise identical setup to Chapter 6, with $\beta = 3$ and $\varepsilon = 0.001$, simulating until a breather emerges.

The evolution of the Hamiltonian H and the component H_2 from $t = 0$ are presented in Figure C.5a, and the corresponding H_4 in Figure C.5c. For this supplemental test we use a larger time step that leads to larger dissipation, though the energy loss over $1000T_f$ is still only 0.5% of the total energy. We see that a clear peak in H_4 has formed before $t = 1000T_f$, indicating the breather has formed. Again, due to the low sampling rate, aliasing is present in the Figures C.5a and C.5c. We provide detailed plots over $5T_f$ of H, H_2 in C.5b and H_4 in C.5d with sufficient sampling such that no aliasing is present. It is clear that the breather remains unchanged under our second scheme which preserves the truncated Hamiltonian system, indicating that the breather is not an artifact of dealiasing.

Finally, we address point 3. The forced-dissipated results shown in this Appendix are computed on a domain with 16 times as many modes, which shows that the breather emerges and persists in simulations with higher spatial resolution.

APPENDIX D

Search for Nearby Periodic Solutions

In this section, we detail our search for exactly periodic solutions to the 2D, defocusing Majda-McLaughlin-Tabak (MMT) model without forcing or dissipation. We employ two different methods: First, a traditional method by Flach [36] used to obtain breathers in Hamiltonian lattice problems. Second, a very recent variational method by Azimi et al. [3] for high degree-of-freedom dynamical systems. Both methods use as an initial condition the numerically-obtained breather solution we discuss in Chapter 6, and our objective is to find a "numerically exact", periodic breather whose state space trajectory is close to the near-periodic one we have observed and reported.

In the following subsections, we adapt these methods for our problem, and we present and discuss the results of our implementations. Although these analyses are in some regards insightful, neither of these techniques return a periodic solution that resembles the breather we have observed. While this certainly may be due to limitations of the methods we employ, it suggests a lack of periodic structures close to our near-periodic breather solution. We begin with the method of Flach.

D.1 Spectral Fixed-point Method

The fixed-point method by Flach exploits two different fixed-point maps to obtain breathers in a Hamiltonian lattice. Our problem is in some sense similar, as we can interpret our problem on a lattice of Fourier modes in wave number domain. First, we will introduce the fixed-point method for our problem, and then we will discuss the results.

D.1.1 Adaptation of the Fixed-point Method

To implement this method, we require the MMT equation in wave number form, which is given by

$$i\frac{\partial \hat{\psi}_{\boldsymbol{k}}}{\partial t} = k^2\hat{\psi}_{\boldsymbol{k}} + \gamma \sum_{\boldsymbol{k}_1,\boldsymbol{k}_2,\boldsymbol{k}_3} (k_1k_2k_3k)^{\beta/4}\hat{\psi}_{\boldsymbol{k1}}\hat{\psi}_{\boldsymbol{k2}}\hat{\psi}^*_{\boldsymbol{k3}}\delta_K(\boldsymbol{k}_1+\boldsymbol{k}_2-\boldsymbol{k}_3-\boldsymbol{k}). \tag{D.1}$$

We introduce the parameter γ to control the size of the nonlinear term, i.e., the nonlinearity level in Chapter 6. We now assert that $\hat{\psi}_{\boldsymbol{k}}(t)$ is periodic in time, such that we can write a Fourier series for the solution,

$$\hat{\psi}_{\boldsymbol{k}} = \sum_n A_{\boldsymbol{k}n} e^{-i\Omega_n t}. \tag{D.2}$$

Here we define $\Omega_1 = 2\pi/T$, where we T is the prescribed period of the solution. The MMT equation (D.6) now becomes the system of nonlinear equations

$$(k^2 - \Omega_n) A_{\boldsymbol{k}n} + F_{\boldsymbol{k}n} = 0, \tag{D.3}$$

where $F_{\boldsymbol{k}n}$ is the full spectral form of the nonlinear term in (D.6). We now follow the arguments of [36], and write two fixed-point iterations schemes to find solutions to (D.3):

$$A_{\boldsymbol{k}n}^{(i+1)} = \frac{k^2}{\Omega_n} A_{\boldsymbol{k}n}^{(i)} + \frac{1}{\Omega_n} F_{\boldsymbol{k}n}^{(i)} \tag{D.4}$$

$$A_{\boldsymbol{k}n}^{(i+1)} = \frac{\Omega_n}{k^2} A_{\boldsymbol{k}n}^{(i)} - \frac{1}{k^2} F_{\boldsymbol{k}n}^{(i)} \tag{D.5}$$

These schemes share identical fixed points. In the small $A_{\boldsymbol{k}n}$ approximation, the eigenvalues of (D.4) and (D.5) are given by k^2/Ω_n and Ω_n/k^2, respectively. These are inverse to one another, such that if the eigenvalue of one map is greater than 1, the other is less than 1. Thus, for any $(\boldsymbol{k}, n)$, we can choose whether or not the mode shrinks or grows in size in the linear approximation. The approach put forth in [36] is to select the fixed-point map for each $(\boldsymbol{k}, n)$ that ensures only the fundamental energy containing mode of the breather grows in the linear approximation. As the $A_{\boldsymbol{k}n}$ evolve under fixed-point iteration, the hope is that a stable fixed point is identified corresponding to a breather with non-negligible amplitude of the energy-containing mode.

We implement the above scheme starting from an initial condition as the breather solution at nonlinearity level $\varepsilon = 0.0008$ and $\beta = 3$ obtained in Chapter 6, with the period set as $T = 2\pi$. We find using a map with an eigenvalue greater than 1 leads to quick divergence of the energy-containing mode upon iteration. Therefore, we also apply a modified scheme, where we choose the map with eigenvalue less than 1 for each mode, with the result presented below.

D.1.2 Results of the Fixed-point Method

The (squared) L^2 norm of the residual $||R||_2^2$ of (D.3) is provided at each iteration up to $N_{iter} = 20$ for a wide variety of γ in figure D.1. It is clear that, even for the smallest γ, the residual does not drop to zero. In fact, the residue always diverges with finite number of iterations. Thus, our adaption of Flach's fixed-point method does not furnish the desired periodic breather solution.

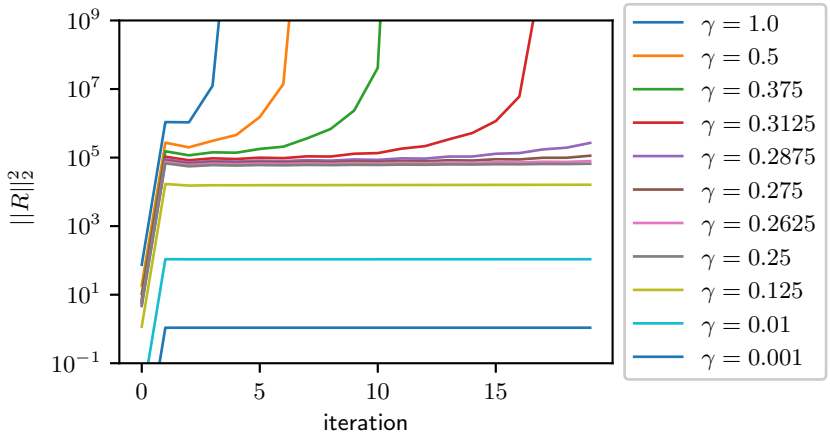

Figure D.1: The residual of (D.3) against iteration number for various choices of γ.

D.2 Variational Method

In this subsection, we adapt the variational method by Azimi et al. [3] for finding periodic solutions to nonlinear systems of high dimension. While we strongly encourage the reader to first review their article before reading this section, we provide a short summary of their method here, with additional details contained in our derivation.

The goal of their method is to numerically obtain periodic solutions to high degree-of-freedom systems. This is done by finding a new dynamical system whose attractors are (potentially) periodic solutions to the equation of interest. This new dynamical system is defined in the space of all periodic orbits that obey the periodic boundary conditions (the "loop space"). Thus, evolution of this new dynamical system is with respect to not the physical time (which is a dimension of the loop space), but rather a parameter τ referred to as "fictitious time". As this system is propagated in τ, the initial loop (a guess of a periodic solution) relaxes towards true periodic solutions to the equation of interest. If a residual of zero is obtained, a periodic solution has been identified.

Before directly applying their method for obtaining such a system, however, we first must modify it to accommodate the MMT equation. Due to nonlocal derivatives, it is better to consider the wave number form of the MMT equation. In addition, ψ_x is a complex scalar, so their method will need to be modified to handle complex fields. These two changes are significant enough to warrant a short discussion. Thus, we first provide a brief overview of our adaption of their variational approach in the following subsection. Then, we present the results of our search for periodic solutions that resemble the breather.

D.2.1 Adaptation of the Variational Method

We begin by writing the MMT equation in wave number form, given by

$$i\frac{\partial\hat{\psi}_{\boldsymbol{k}}}{\partial t} = k^2\hat{\psi}_{\boldsymbol{k}} + \sum_{\boldsymbol{k}_1,\boldsymbol{k}_2,\boldsymbol{k}_3} (k_1k_2k_3k)^{\beta/4}\hat{\psi}_{\boldsymbol{k1}}\hat{\psi}_{\boldsymbol{k2}}\hat{\psi}^*_{\boldsymbol{k3}}\delta_K(\boldsymbol{k}_1+\boldsymbol{k}_2-\boldsymbol{k}_3-\boldsymbol{k}). \tag{D.6}$$

Because this is an evolution equation for the coefficients of a Fourier series, the periodic boundary conditions imposed on our physical domain are automatically satisfied. Thus, the loop space is simply the set of all possible sets of Fourier modes $\{\hat{\psi}_{\boldsymbol{k}}\}$ that are periodic with a period of T. We then can the express a loop I in this loop space as

$$I = \begin{bmatrix} \hat{\psi}_{\boldsymbol{k}}(t) \\ \hat{\psi}^*_{\boldsymbol{k}}(t) \\ T \end{bmatrix}. \tag{D.7}$$

where $t \in [0,T]$ and $\boldsymbol{k}$ represents all resolved wave numbers in (D.6). Note that we have included the conjugate $\hat{\psi}^*_{\boldsymbol{k}}$ to ensure gradients with respect to I are well defined for the complex variables $\hat{\psi}_{\boldsymbol{k}}$ [53]. Just as in [3], we make a substitution of variables such that $t = sT$. Next, we require a suitable inner product on the loop space. For this, we use the Hermitian inner product

$$\langle I, I'\rangle = \int_0^1 \sum_{\boldsymbol{k}} \left(\hat{\psi}^*_{\boldsymbol{k}}\hat{\psi}'_{\boldsymbol{k}} + \hat{\psi}_{\boldsymbol{k}}\hat{\psi}^{*\prime}_{\boldsymbol{k}}\right) ds + TT'. \tag{D.8}$$

For this choice of loop space and inner product, the method and conclusions of [3] hold for a periodic complex field subject to non-local derivatives as in (D.6).

We proceed by outlining our derivation of the τ-evolution equation for I. For a given initial loop I_0, we seek a derivative $\frac{\partial I}{\partial \tau}$ for which the square residual norm $J(I)$ monotonically decreases. The square residual norm is defined by $J(I) \equiv \langle R(I), R(I)\rangle$, where the MMT equation residual is given by

$$R(I) = \begin{bmatrix} R_1 \\ R_2 \\ R_3 \end{bmatrix} \equiv \begin{bmatrix} -\frac{1}{T}\frac{\partial\hat{\psi}_{\boldsymbol{k}}}{\partial s} - ik^2\hat{\psi}_{\boldsymbol{k}} - i\sum_{(\boldsymbol{k}_1,\boldsymbol{k}_2,\boldsymbol{k}_3)}(k_1k_2k_3k)^{\beta/4}\hat{\psi}_{\boldsymbol{k1}}\hat{\psi}_{\boldsymbol{k2}}\hat{\psi}^*_{\boldsymbol{k3}}\delta_K(\boldsymbol{k}_1+\boldsymbol{k}_2-\boldsymbol{k}_3-\boldsymbol{k}) \\ \text{c.c.} \\ 0 \end{bmatrix}. \tag{D.9}$$

We now assume some $G(I)$ to be the derivative of interest ($\frac{\partial I}{\partial \tau} = G(I)$), and then define

$$\mathcal{L}(I;G) = \lim_{h\to 0}\frac{R(I+hG) - R(I)}{h} \tag{D.10}$$

as the derivative of the residual in the direction of the evolution of I. The paper [3] shows that if $G(I) = -\mathcal{L}^\dagger(I;R)$, where $\mathcal{L}^\dagger(I;R)$ is the adjoint operator to $\mathcal{L}(I;G)$ defined by

$$\langle G, \mathcal{L}^\dagger(I;R)\rangle = \langle \mathcal{L}(I;G), R\rangle, \tag{D.11}$$

then $\frac{\partial J}{\partial \tau} \leq 0$ is guaranteed for all τ. It then follows that, for this choice of $G(I)$, any initial guess at a periodic solution to the MMT equation I_0 will evolve in τ until a minimum of J is achieved. If $J \neq 0$, no periodic solution is contained within the basin of attraction. If $J = 0$, a periodic solution has been identified. For our system, the adjoint operator can be found according to (D.11) as

$$\mathcal{L}^\dagger(I;R) = \begin{bmatrix} \dfrac{1}{T}\dfrac{\partial R_1}{\partial s} + ik^2 R_1 + 2iR_1 k^{-\beta/2} \displaystyle\sum_{\boldsymbol{k}_1} k_1^{-\beta/2} \hat{\psi}_{\boldsymbol{k1}} \hat{\psi}^*_{\boldsymbol{k1}} \\ -iR_1^* k^{-\beta/2} \displaystyle\sum_{(\boldsymbol{k}_1,\boldsymbol{k}_2)} (k_1 k_2)^{-\beta/4} \hat{\psi}_{\boldsymbol{k1}} \hat{\psi}_{\boldsymbol{k2}} \delta_K(\boldsymbol{k}_1 + \boldsymbol{k}_2 - 2\boldsymbol{k}) \\ \text{c.c.} \\ \frac{2}{T^2} \int_0^1 \sum_{\boldsymbol{k}} \mathrm{Re}\left[\frac{\partial \hat{\psi}^*}{\partial s} R_1\right] ds \end{bmatrix}. \tag{D.12}$$

D.2.2 Results of the Variational Method

We now present the results of this analysis. We choose as an initial condition one full cycle of the breather at very low nonlinearity ($\varepsilon = 0.0004$), for which the system is very close to periodic. To reduce stiffness of the system, we choose the $\beta = 1$ case. A snapshot of initial condition is contained in Figure D.2a. The system is then evolved according to the presented procedure. As expected, the residual norm J decreases monotonically, as depicted in Figure D.3a. We do not simulate long enough to reach a steady value of J, as after just $\tau = 50$ ($\sim$ 5000 time steps) we already can see that the loop has strongly diverged from the expected breather pattern. The corresponding snapshot of the initial breather peak after $\tau = 50$ is contained in Figure D.2b. Both the position, shape, and magnitude of the resolved peak are drastically different from the exactly periodic breather we seek. This is also depicted in a growth of T (Fig. D.3b) beyond the expected $T \approx 2\pi$. From the above observations, it is clear that the variational method also does not find a nearby exact periodic breather solution. We also note that there may be certain modifications we can make on the basis of this method, e.g., to preserve the Hamiltonian of the solution through a Lagrangian multiplier term, which may provide a different solution. These challenges will not be tackled in the current work.

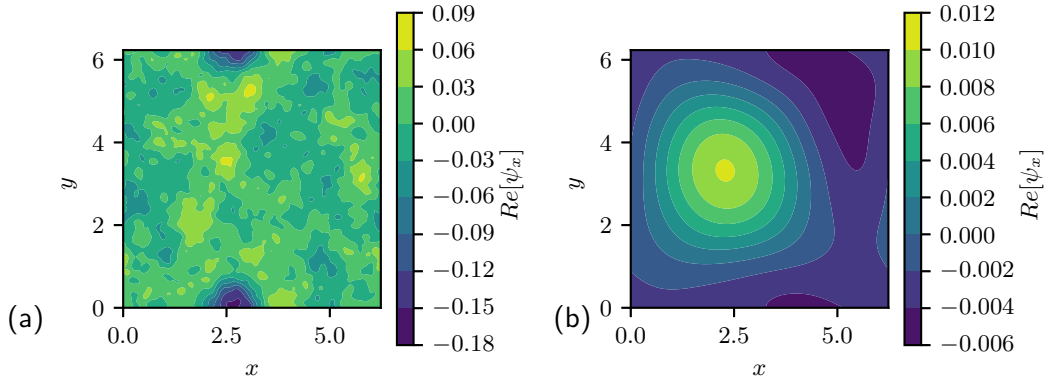

Figure D.2: (a) a snapshot of the initial condition I_0 in the variational method; (b) a snapshot of the solution at $\tau = 50$, i.e., after 5000 time steps.

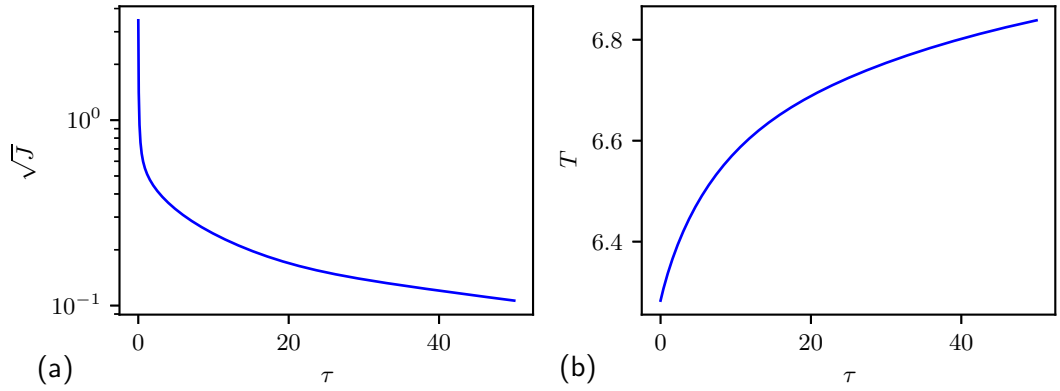

Figure D.3: The change of (a) residue norm $\sqrt{J}$ and (b) period T as functions of τ in variational method.

BIBLIOGRAPHY

[1] Sergei Yu Annenkov and Victor I. Shrira. Role of non-resonant interactions in the evolution of nonlinear random water wave fields. *Journal of Fluid Mechanics*, 561:181–207, August 2006. Publisher: Cambridge University Press.

[2] Quentin Aubourg and Nicolas Mordant. Nonlocal Resonances in Weak Turbulence of Gravity-Capillary Waves. *Physical Review Letters*, 114(14):144501, April 2015. Number: 14 Publisher: American Physical Society.

[3] Sajjad Azimi, Omid Ashtari, and Tobias M. Schneider. Constructing periodic orbits of high-dimensional chaotic systems by an adjoint-based variational method. *Physical Review E*, 105(1):014217, January 2022. Publisher: American Physical Society.

[4] M. M. Bandi, W. I. Goldburg, J. R. Cressman, and A. Pumir. Energy flux fluctuations in a finite volume of turbulent flow. *Physical Review E*, 73(2):026308, February 2006. Number: 2 Publisher: American Physical Society.

[5] J. Bourgain. Quasi-Periodic Solutions of Hamiltonian Perturbations of 2D Linear Schrödinger Equations. *Annals of Mathematics*, 148(2):363–439, 1998. Publisher: Annals of Mathematics.

[6] Laurent Boué, Ratul Dasgupta, Jason Laurie, Victor L'vov, Sergey Nazarenko, and Itamar Procaccia. Exact solution for the energy spectrum of Kelvin-wave turbulence in superfluids. *Physical Review B*, 84(6):064516, August 2011. Publisher: American Physical Society.

[7] T. Buckmaster, P. Germain, Z. Hani, and J. Shatah. Onset of the wave turbulence description of the longtime behavior of the nonlinear Schrödinger equation. *Inventiones mathematicae*, 225(3):787–855, September 2021. Number: 3.

[8] David Cai, Andrew J. Majda, David W. McLaughlin, and Esteban G. Tabak. Spectral bifurcations in dispersive wave turbulence. *Proceedings of the National Academy of Sciences*, 96(25):14216–14221, December 1999. Number: 25 Publisher: National Academy of Sciences Section: Physical Sciences.

[9] Antoine Campagne, Roumaissa Hassaini, Ivan Redor, Thomas Valran, Samuel Viboud, Joël Sommeria, and Nicolas Mordant. Identifying four-wave-resonant interactions in a surface gravity wave turbulence experiment. *Physical Review Fluids*, 4(7):074801, July 2019. Publisher: American Physical Society.

[10] A. Cazaubiel, S. Mawet, A. Darras, G. Grosjean, J.J.W.A. van Loon, S. Dorbolo, and E. Falcon. Wave Turbulence on the Surface of a Fluid in a High-Gravity Environment. *Physical Review Letters*, 123(24):244501, December 2019. Publisher: American Physical Society.

[11] S. Chibbaro, F. De Lillo, and M. Onorato. Weak versus strong wave turbulence in the Majda-McLaughlin-Tabak model. *Physical Review Fluids*, 2(5):052603, May 2017. Number: 5 Publisher: American Physical Society.

[12] Sergio Chibbaro, Giovanni Dematteis, and Lamberto Rondoni. 4-wave dynamics in kinetic wave turbulence. *Physica D: Nonlinear Phenomena*, 362:24–59, January 2018.

[13] K. W. Chow, R. H. J. Grimshaw, and E. Ding. Interactions of breathers and solitons in the extended Korteweg–de Vries equation. *Wave Motion*, 43(2):158–166, December 2005.

[14] Simon Clarke, Roger Grimshaw, Peter Miller, Efim Pelinovsky, and Tatiana Talipova. On the generation of solitons and breathers in the modified Korteweg–de Vries equation. *Chaos: An Interdisciplinary Journal of Nonlinear Science*, 10(2):383–392, June 2000. Publisher: American Institute of Physics.

[15] P. Cobelli, A. Przadka, P. Petitjeans, G. Lagubeau, V. Pagneux, and A. Maurel. Different Regimes for Water Wave Turbulence. *Physical Review Letters*, 107(21):214503, November 2011. Publisher: American Physical Society.

[16] Colm Connaughton, Sergey Nazarenko, and Andrei Pushkarev. Discreteness and quasiresonances in weak turbulence of capillary waves. *Physical Review E*, 63(4):046306, March 2001. Publisher: American Physical Society.

[17] Thierry Cretegny, Thierry Dauxois, Stefano Ruffo, and Alessandro Torcini. Localization and equipartition of energy in the -FPU chain: Chaotic breathers. *Physica D: Nonlinear Phenomena*, 121(1):109–126, October 1998.

[18] Jesús Cuevas-Maraver, Panayotis G. Kevrekidis, and Floyd Williams, editors. *The sine-Gordon Model and its Applications*, volume 10 of *Nonlinear Systems and Complexity*. Springer International Publishing, Cham, 2014.

[19] L. Deike, B. Miquel, P. Gutiérrez, T. Jamin, B. Semin, M. Berhanu, E. Falcon, and F. Bonnefoy. Role of the basin boundary conditions in gravity wave turbulence. *Journal of Fluid Mechanics*, 781:196–225, October 2015. Publisher: Cambridge University Press.

[20] Luc Deike, Michael Berhanu, and Eric Falcon. Energy flux measurement from the dissipated energy in capillary wave turbulence. *Physical Review E*, 89(2):023003, February 2014. Publisher: American Physical Society.

[21] Luc Deike, Daniel Fuster, Michael Berhanu, and Eric Falcon. Direct Numerical Simulations of Capillary Wave Turbulence. *Physical Review Letters*, 112(23):234501, June 2014. Number: 23 Publisher: American Physical Society.

[22] Yu Deng and Zaher Hani. Full derivation of the wave kinetic equation. *arXiv:2104.11204 [math-ph]*, May 2021. arXiv: 2104.11204.

[23] Yu Deng and Zaher Hani. On the derivation of the wave kinetic equation for NLS. *Forum of Mathematics, Pi*, 9:e6, January 2021. Publisher: Cambridge University Press.

[24] Petr Denissenko, Sergei Lukaschuk, and Sergey Nazarenko. Gravity Wave Turbulence in a Laboratory Flume. *Physical Review Letters*, 99(1):014501, July 2007. Publisher: American Physical Society.

[25] Cui-Cui Ding, Yi-Tian Gao, and Liu-Qing Li. Breathers and rogue waves on the periodic background for the Gerdjikov-Ivanov equation for the Alfvén waves in an astrophysical plasma. *Chaos, Solitons & Fractals*, 120:259–265, March 2019.

[26] John M. Dudley, Frédéric Dias, Miro Erkintalo, and Goëry Genty. Instabilities, breathers and rogue waves in optics. *Nature Photonics*, 8(10):755–764, October 2014. Number: 10 Publisher: Nature Publishing Group.

[27] H Scott Dumas. *The KAM Story: A Friendly Introduction to the Content, History, and Significance of Classical Kolmogorov–Arnold–Moser Theory*. WORLD SCIENTIFIC, April 2014.

[28] Kristian B. Dysthe and Karsten Trulsen. Note on Breather Type Solutions of the NLS as Models for Freak-Waves. *Physica Scripta*, 1999(T82):48, January 1999. Publisher: IOP Publishing.

[29] Gustavo Düring, Christophe Josserand, and Sergio Rica. Wave turbulence theory of elastic plates. *Physica D: Nonlinear Phenomena*, 347:42–73, May 2017.

[30] Gregory L. Eyink and Yi-Kang Shi. Kinetic wave turbulence. *Physica D: Nonlinear Phenomena*, 241(18):1487–1511, September 2012.

[31] Eric Falcon and Nicolas Mordant. Experiments in Surface Gravity–Capillary Wave Turbulence. *Annual Review of Fluid Mechanics*, 54(1):1–25, 2022. _eprint: https://doi.org/10.1146/annurev-fluid-021021-102043.

[32] Éric Falcon, Sébastien Aumaître, Claudio Falcón, Claude Laroche, and Stéphan Fauve. Fluctuations of Energy Flux in Wave Turbulence. *Physical Review Letters*, 100(6):064503, February 2008. Number: 6 Publisher: American Physical Society.

[33] G. E. Falkovich and A. V. Shafarenko. Nonstationary wave turbulence. *Journal of Nonlinear Science*, 1(4):457–480, December 1991. Number: 4.

[34] Gregory Falkovich. Bottleneck phenomenon in developed turbulence. *Physics of Fluids*, 6(4):1411–1414, April 1994.

[35] Erwan Faou, Pierre Germain, and Zaher Hani. The weakly nonlinear large-box limit of the 2D cubic nonlinear Schrödinger equation. *Journal of the American Mathematical Society*, 29(4):915–982, 2016. Publisher: American Mathematical Society.

[36] S. Flach. Obtaining breathers in nonlinear Hamiltonian lattices. *Physical Review E*, 51(4):3579–3587, April 1995. Number: 4 Publisher: American Physical Society.

[37] Sergej Flach and Andrey V. Gorbach. Discrete breathers — Advances in theory and applications. *Physics Reports*, 467(1):1–116, October 2008.

[38] S. Galtier, S. V. Nazarenko, A. C. Newell, and A. Pouquet. A weak turbulence theory for incompressible magnetohydrodynamics. *Journal of Plasma Physics*, 63(5):447–488, June 2000. Publisher: Cambridge University Press.

[39] Sébastien Galtier and Sergey V. Nazarenko. Direct Evidence of a Dual Cascade in Gravitational Wave Turbulence. *Physical Review Letters*, 127(13):131101, September 2021. Number: 13 Publisher: American Physical Society.

[40] Jiansheng Geng, Xindong Xu, and Jiangong You. An infinite dimensional KAM theorem and its application to the two dimensional cubic Schrödinger equation. *Advances in Mathematics*, 226(6):5361–5402, April 2011.

[41] Adam Griffin, Giorgio Krstulovic, Victor S. L'vov, and Sergey Nazarenko. Energy Spectrum of Two-Dimensional Acoustic Turbulence. *Physical Review Letters*, 128(22):224501, June 2022. Publisher: American Physical Society.

[42] Roumaissa Hassaini and Nicolas Mordant. Confinement effects on gravity-capillary wave turbulence. *Physical Review Fluids*, 3(9):094805, September 2018. Publisher: American Physical Society.

[43] K. Hasselmann. On the non-linear energy transfer in a gravity-wave spectrum Part 1. General theory. *Journal of Fluid Mechanics*, 12(4):481–500, April 1962. Number: 4 Publisher: Cambridge University Press.

[44] Alexander Hrabski and Yulin Pan. Effect of discrete resonant manifold structure on discrete wave turbulence. *Physical Review E*, 102(4):041101, October 2020. Number: 4 Publisher: American Physical Society.

[45] Alexander Hrabski and Yulin Pan. On the properties of energy flux in wave turbulence. *Journal of Fluid Mechanics*, 936, April 2022. Publisher: Cambridge University Press.

[46] Alexander Hrabski, Yulin Pan, Gigliola Staffilani, and Bobby Wilson. Energy transfer for solutions to the nonlinear Schr\"odinger equation on irrational tori. *arXiv:2107.01459 [math]*, July 2021. arXiv: 2107.01459.

[47] Peter A. E. M. Janssen. Nonlinear Four-Wave Interactions and Freak Waves. *Journal of Physical Oceanography*, 33(4):863–884, April 2003. Number: 4 Publisher: American Meteorological Society Section: Journal of Physical Oceanography.

[48] E. Kartashova. Discrete wave turbulence. *Europhysics Letters*, 87(4):44001, September 2009.

[49] Elena A. Kartashova. Partitioning of ensembles of weakly interacting dispersing waves in resonators into disjoint classes. *Physica D: Nonlinear Phenomena*, 46(1):43–56, October 1990.

[50] David J. Kaup and Alan C. Newell. An exact solution for a derivative nonlinear Schrödinger equation. *Journal of Mathematical Physics*, 19(4):798–801, August 2008.

[51] Robert H. Kraichnan. The structure of isotropic turbulence at very high Reynolds numbers. *Journal of Fluid Mechanics*, 5(4):497–543, May 1959. Publisher: Cambridge University Press.

[52] Robert H. Kraichnan. An almost-Markovian Galilean-invariant turbulence model. *Journal of Fluid Mechanics*, 47(3):513–524, June 1971. Publisher: Cambridge University Press.

[53] Ken Kreutz-Delgado. The Complex Gradient Operator and the CR-Calculus, June 2009. arXiv:0906.4835 [math].

[54] Ying-Cheng Lai, Da-Ren He, and Yu-Mei Jiang. Basins of attraction in piecewise smooth Hamiltonian systems. *Physical Review E*, 72(2):025201, August 2005. Publisher: American Physical Society.

[55] Claude Laroche, Jean-Claude Bacri, Martin Devaud, Timothée Jamin, and Eric Falcon. Observation of the Resonance Frequencies of a Stable Torus of Fluid. *Physical Review Letters*, 123(9):094502, August 2019. Publisher: American Physical Society.

[56] Anna Lischke, Guofei Pang, Mamikon Gulian, Fangying Song, Christian Glusa, Xiaoning Zheng, Zhiping Mao, Wei Cai, Mark M. Meerschaert, Mark Ainsworth, and George Em Karniadakis. What is the fractional Laplacian? A comparative review with new results. *Journal of Computational Physics*, 404:109009, March 2020.

[57] R. Livi, M. Spicci, and R. S. MacKay. Breathers on a diatomic FPU chain. *Nonlinearity*, 10(6):1421–1434, November 1997. Publisher: IOP Publishing.

[58] Yuri V. Lvov, Sergey Nazarenko, and Boris Pokorni. Discreteness and its effect on water-wave turbulence. *Physica D: Nonlinear Phenomena*, 218(1):24–35, June 2006.

[59] V. S. L'vov, Yu. L'vov, A. C. Newell, and V. Zakharov. Statistical description of acoustic turbulence. *Physical Review E*, 56(1):390–405, July 1997. Publisher: American Physical Society.

[60] V. S. L'vov and S. Nazarenko. Discrete and mesoscopic regimes of finite-size wave turbulence. *Physical Review E*, 82(5):056322, November 2010. Number: 5 Publisher: American Physical Society.

[61] A. J. Majda, D. W. McLaughlin, and E. G. Tabak. A one-dimensional model for dispersive wave turbulence. *Journal of Nonlinear Science*, 7(1):9–44, February 1997. Number: 1.

[62] Benoit B. Mandelbrot. Lognormal hypothesis and distribution of energy dissipation in intermittent turbulence. In *Multifractals and 1/f Noise*, pages 294–316. Springer New York, New York, NY, 1999.

[63] Guillaume Michel, Benoît Semin, Annette Cazaubiel, Florence Haudin, Thomas Humbert, Simon Lepot, Félicien Bonnefoy, Michaël Berhanu, and Éric Falcon. Self-similar gravity wave spectra resulting from the modulation of bound waves. *Physical Review Fluids*, 3(5):054801, May 2018. Publisher: American Physical Society.

[64] Benjamin Miquel, Alexandros Alexakis, Christophe Josserand, and Nicolas Mordant. Transition from Wave Turbulence to Dynamical Crumpling in Vibrated Elastic Plates. *Physical Review Letters*, 111(5):054302, August 2013. Publisher: American Physical Society.

[65] Benjamin Miquel, Alexandros Alexakis, and Nicolas Mordant. Role of dissipation in flexural wave turbulence: From experimental spectrum to Kolmogorov-Zakharov spectrum. *Physical Review E*, 89(6):062925, June 2014. Publisher: American Physical Society.

[66] A. E. Miroshnichenko, S. Flach, M. V. Fistul, Y. Zolotaryuk, and J. B. Page. Breathers in Josephson junction ladders: Resonances and electromagnetic wave spectroscopy. *Physical Review E*, 64(6):066601, November 2001. Publisher: American Physical Society.

[67] Eduardo Monsalve, Maxime Brunet, Basile Gallet, and Pierre-Philippe Cortet. Quantitative Experimental Observation of Weak Inertial-Wave Turbulence. *Physical Review Letters*, 125(25):254502, December 2020. Number: 25 Publisher: American Physical Society.

[68] N. Mordant. Fourier analysis of wave turbulence in a thin elastic plate. *The European Physical Journal B*, 76(4):537–545, August 2010. Number: 4.

[69] Sergey Nazarenko. *Wave Turbulence*, volume 825 of *Lecture Notes in Physics*. Springer, Berlin, Heidelberg, 2011.

[70] Sergey Nazarenko. Verifying Weak Turbulence Theory. *Physics*, 13:194, December 2020. Publisher: American Physical Society.

[71] Sergey Nazarenko and Miguel Onorato. Wave turbulence and vortices in Bose–Einstein condensation. *Physica D: Nonlinear Phenomena*, 219(1):1–12, July 2006. Number: 1.

[72] Alan C. Newell, Sergey Nazarenko, and Laura Biven. Wave turbulence and intermittency. *Physica D: Nonlinear Phenomena*, 152-153:520–550, May 2001.

[73] M. Onorato and G. Dematteis. A straightforward derivation of the four-wave kinetic equation in action-angle variables. *Journal of Physics Communications*, 4(9):095016, September 2020. Number: 9 Publisher: IOP Publishing.

[74] Miguel Onorato, Davide Proment, Günther Clauss, and Marco Klein. Rogue Waves: From Nonlinear Schrödinger Breather Solutions to Sea-Keeping Test. *PLOS ONE*, 8(2):e54629, February 2013. Publisher: Public Library of Science.

[75] Yulin Pan, Brian K. Arbic, Arin D. Nelson, Dimitris Menemenlis, W. R. Peltier, Wentao Xu, and Ye Li. Numerical Investigation of Mechanisms Underlying Oceanic Internal Gravity Wave Power-Law Spectra. *Journal of Physical Oceanography*, 50(9):2713–2733, September 2020. Publisher: American Meteorological Society Section: Journal of Physical Oceanography.

[76] Yulin Pan and Dick K. P. Yue. Decaying capillary wave turbulence under broad-scale dissipation. *Journal of Fluid Mechanics*, 780, October 2015. Publisher: Cambridge University Press.

[77] Yulin Pan and Dick K. P. Yue. Understanding discrete capillary-wave turbulence using a quasi-resonant kinetic equation. *Journal of Fluid Mechanics*, 816, April 2017. Publisher: Cambridge University Press.

[78] Yulin Pan and Dick K.P. Yue. Direct Numerical Investigation of Turbulence of Capillary Waves. *Physical Review Letters*, 113(9):094501, August 2014. Publisher: American Physical Society.

[79] R. Peierls. Zur kinetischen Theorie der Wärmeleitung in Kristallen. *Annalen der Physik*, 395(8):1055–1101, 1929. _eprint: https://onlinelibrary.wiley.com/doi/pdf/10.1002/andp.19293950803.

[80] L. Pistone, M. Onorato, and S. Chibbaro. Thermalization in the discrete nonlinear Klein-Gordon chain in the wave-turbulence framework. *EPL (Europhysics Letters)*, 121(4):44003, February 2018. Number: 4 Publisher: IOP Publishing.

[81] K. L. Polzin and Y. V. Lvov. Toward Regional Characterizations of the Oceanic Internal Wavefield. *Reviews of Geophysics*, 49(4), 2011. _eprint: https://onlinelibrary.wiley.com/doi/pdf/10.1029/2010RG000329.

[82] C. Procesi and M. Procesi. A KAM algorithm for the resonant non-linear Schrödinger equation. *Advances in Mathematics*, 272:399–470, February 2015.

[83] A. Pushkarev and V. E. Zakharov. Quasibreathers in the MMT model. *Physica D: Nonlinear Phenomena*, 248:55–61, April 2013.

[84] A. N. Pushkarev and V. E. Zakharov. Turbulence of capillary waves — theory and numerical simulation. *Physica D: Nonlinear Phenomena*, 135(1):98–116, January 2000. Number: 1.

[85] Benno Rumpf. Simple statistical explanation for the localization of energy in nonlinear lattices with two conserved quantities. *Physical Review E*, 69(1):016618, January 2004. Number: 1 Publisher: American Physical Society.

[86] Benno Rumpf and Alan C. Newell. Coherent Structures and Entropy in Constrained, Modulationally Unstable, Nonintegrable Systems. *Physical Review Letters*, 87(5):054102, July 2001. Number: 5 Publisher: American Physical Society.

[87] Benno Rumpf and Alan C. Newell. Wave instability under short-wave amplitude modulations. *Physics Letters A*, 377(18):1260–1263, August 2013. Number: 18.

[88] Benno Rumpf, Alan C. Newell, and Vladimir E. Zakharov. Turbulent Transfer of Energy by Radiating Pulses. *Physical Review Letters*, 103(7):074502, August 2009. Number: 7 Publisher: American Physical Society.

[89] Benno Rumpf and Thomas Y. Sheffield. Transition of weak wave turbulence to wave turbulence with intermittent collapses. *Physical Review E*, 92(2):022927, August 2015. Number: 2 Publisher: American Physical Society.

[90] R. Saint-Jalm, P.C.M. Castilho, É. Le Cerf, B. Bakkali-Hassani, J.-L. Ville, S. Nascimbene, J. Beugnon, and J. Dalibard. Dynamical Symmetry and Breathers in a Two-Dimensional Bose Gas. *Physical Review X*, 9(2):021035, May 2019. Number: 2 Publisher: American Physical Society.

[91] J. M. Sanz-Serna and M. P. Calvo. *Numerical Hamiltonian Problems*. Dover Publications, Mineola, New York, illustrated edition edition, June 2018.

[92] Thomas Y. Sheffield and Benno Rumpf. Ensemble dynamics and the emergence of correlations in one- and two-dimensional wave turbulence. *Physical Review E*, 95(6):062225, June 2017. Number: 6 Publisher: American Physical Society.

[93] Gigliola Staffilani and Bobby Wilson. Stability of the Cubic Nonlinear Schrodinger Equation on an Irrational Torus. *SIAM Journal on Mathematical Analysis*, 52(2):1318–1342, January 2020. Publisher: Society for Industrial and Applied Mathematics.

[94] Masayoshi Tajiri and Yosuke Watanabe. Breather solutions to the focusing nonlinear Schr\"odinger equation. *Physical Review E*, 57(3):3510–3519, March 1998. Publisher: American Physical Society.

[95] Hendrik L Tolman. User manual and system documentation of WAVEWATCH III TM version 3.14.

[96] E. Trías, J. J. Mazo, and T. P. Orlando. Discrete Breathers in Nonlinear Lattices: Experimental Detection in a Josephson Array. *Physical Review Letters*, 84(4):741–744, January 2000. Publisher: American Physical Society.

[97] Yue Wu and Yulin Pan. Energy cascade in the Garrett-Munk spectrum of internal gravity waves, May 2023. arXiv:2305.13110 [physics].

[98] P. K. Yeung and K. Ravikumar. Advancing understanding of turbulence through extreme-scale computation: Intermittency and simulations at large problem sizes. *Physical Review Fluids*, 5(11):110517, November 2020. Number: 11 Publisher: American Physical Society.

[99] V. E. Zakharov and N. N. Filonenko. Weak turbulence of capillary waves. *Journal of Applied Mechanics and Technical Physics*, 8(5):37–40, September 1967. Number: 5.

[100] V. E. Zakharov, P. Guyenne, A. N. Pushkarev, and F. Dias. Wave turbulence in one-dimensional models. *Physica D: Nonlinear Phenomena*, 152-153:573–619, May 2001.

[101] Vladimir E. Zakharov, Victor S. L'vov, and Gregory Falkovich. *Kolmogorov spectra of turbulence I: Wave turbulence*. Springer Sci. & Bus. Media, 1992.

[102] Zhou Zhang and Yulin Pan. Numerical investigation of turbulence of surface gravity waves. *arXiv:2108.01189 [physics]*, August 2021. arXiv: 2108.01189.

[103] Zhou Zhang and Yulin Pan. Forward and inverse cascades by exact resonances in surface gravity waves. *Physical Review E*, 106(4):044213, October 2022. Publisher: American Physical Society.